UNIVERSIDADE FEDERAL DE MINAS GERAIS
Escola de Engenharia
Programa de Pós-Graduação em Engenharia Elétrica

Igor Rodrigues de Oliveira

THERMAL ANALYSIS OF POWER CONVERTERS FOR DOUBLY-FED INDUCTION WIND GENERATORS DURING LOW VOLTAGE RIDE-THROUGH

Belo Horizonte
2023

Igor Rodrigues de Oliveira

THERMAL ANALYSIS OF POWER CONVERTERS FOR DOUBLY-FED INDUCTION WIND GENERATORS DURING LOW VOLTAGE RIDE-THROUGH

Tese apresentada ao Programa de Pós-Graduação em Engenharia Elétrica da Universidade Federal de Minas Gerais, como requisito parcial à obtenção do título de Doutor em Engenharia Elétrica.

Orientador: Prof. Dr. Victor Flores Mendes
Coorientador: Prof. Dr. Fernando Lessa Tofoli

Belo Horizonte
2023

Oliveira, Igor Rodrigues de.
O48t Thermal analysis of power converters for doubly-fed induction wind generators during low voltage ride-through [recurso eletrônico] / Igor Rodrigues de Oliveira. - 2023.
1 recurso online (175 f. : il., color.) : pdf.

Orientador: Victor Flores Mendes.
Coorientador: Fernando Lessa Tofoli.

Tese (doutorado) - Universidade Federal de Minas Gerais, Escola de Engenharia.

Bibliografia: f. 164-175.
Exigências do sistema: Adobe Acrobat Reader.

1. Engenharia elétrica - Teses. 2. Análise térmica - Teses. 3. Energia eólica - Teses. 4. Conversores - Teses. 5. Geradores elétricos - Teses. 6. Afundamento de tensão - Teses. 7. Potência reativa (Engenharia elétrica) - Teses. I. Mendes, Victor Flores. II. Tofoli, Fernando Lessa. III. Universidade Federal de Minas Gerais. Escola de Engenharia. IV. Título.

CDU: 621.3(043)

Ficha catalográfica elaborada pela Bibliotecária Ângela Cristina Silva - CRB-6/2361
Biblioteca Prof. Mário Werneck, Escola de Engenharia da UFMG.

UNIVERSIDADE FEDERAL DE MINAS GERAIS
ESCOLA DE ENGENHARIA
PROGRAMA DE PÓS-GRADUAÇÃO EM ENGENHARIA ELÉTRICA

FOLHA DE APROVAÇÃO

"THERMAL ANALYSIS OF POWER CONVERTERS FOR DOUBLY-FED INDUCTION WIND GENERATORS DURING LOW VOLTAGE RIDE-THROUGH"

IGOR RODRIGUES DE OLIVEIRA

Tese de Doutorado submetida à Banca Examinadora designada pelo Colegiado do Programa de Pós-Graduação em Engenharia Elétrica da Escola de Engenharia da Universidade Federal de Minas Gerais, como requisito para obtenção do grau de Doutor em Engenharia Elétrica. Aprovada em 19 de dezembro de 2023. Por:

Prof. Dr. Victor Flores Mendes
DEE (UFMG) - Orientador

Prof. Dr. Fernando Lessa Tofoli
(UFSJ) - Coorientador

Prof. Dr. Gabriel Azevedo Fogli
(UFMG)

Prof. Dr. Allan Fagner Cupertino
(UFJF)

Prof. Dr. Clodualdo Venicio de Sousa
(UNIFEI)

Prof. Dr. Arthur Eduardo Alves Amorim
(IFES Espírito Santo)

Documento assinado eletronicamente por **Victor Flores Mendes**, **Professor do Magistério Superior**, em 19/01/2024, às 10:36, conforme horário oficial de Brasília, com fundamento no art. 5º do Decreto nº 10.543, de 13 de novembro de 2020.

Documento assinado eletronicamente por **Fernando Lessa Tofoli**, **Usuário Externo**, em 19/01/2024, às 10:41, conforme horário oficial de Brasília, com fundamento no art. 5º do Decreto nº 10.543, de 13 de novembro de 2020.

Documento assinado eletronicamente por **Clodualdo Venicio de Sousa**, **Usuário Externo**, em 21/01/2024, às 19:22, conforme horário oficial de Brasília, com fundamento no art. 5º do Decreto nº 10.543, de 13 de novembro de 2020.

Documento assinado eletronicamente por **Allan Fagner Cupertino**, **Usuário Externo**, em 29/01/2024, às 14:47, conforme horário oficial de Brasília, com fundamento no art. 5º do Decreto nº 10.543, de 13 de novembro de 2020.

Documento assinado eletronicamente por **Arthur Eduardo Alves Amorim**, **Usuário Externo**, em 03/02/2024, às 09:28, conforme horário oficial de Brasília, com fundamento no art. 5º do Decreto nº 10.543, de 13 de novembro de 2020.

Documento assinado eletronicamente por **Gabriel Azevedo Fogli**, **Professor do Magistério Superior**, em 05/02/2024, às 10:43, conforme horário oficial de Brasília, com fundamento no art. 5º do Decreto nº 10.543, de 13 de novembro de 2020.

A autenticidade deste documento pode ser conferida no site https://sei.ufmg.br/sei/controlador_externo.php?acao=documento_conferir&id_orgao_acesso_externo=0, informando o código verificador **2974763** e o código CRC **313B8DBB**.

Referência: Processo nº 23072.277916/2023-11 SEI nº 2974763

Dedicated to God, my parents, and my sister

ACKNOWLEDGMENT

I express my heartfelt gratitude to my parents, José Custódio and Maria Aparecida, for their unwavering affection, boundless love, and dedicated prayers throughout my life. Their guidance and the values instilled in me have been fundamental in shaping my character. I am also deeply thankful to my sister, Agatha, for her enduring affection, unwavering support, and dedicated encouragement. Additionally, I extend my gratitude to my aunt, Marilda, for her assistance and for graciously providing me a place to stay in Belo Horizonte.

I want to express my deep appreciation to my girlfriend, Aurora, for her unwavering love, affection, companionship, and dedication. Your encouragement has been invaluable to me throughout my doctoral journey. Thank you for bringing happiness into my life.

I extend my sincere appreciation to professors Victor Flores Mendes and Fernando Lessa Tofoli for their invaluable guidance, unwavering support, dedication, and commitment to the development of this work.

I express my heartfelt gratitude to my colleagues at LCCE whose support was invaluable in the realization of this work. I extend my thanks to Lucas, Israel, Chrystiano, and Samuel for their friendship and partnership, both within and outside the laboratory.

I extend my gratitude to the professors of the Graduate Program in Electrical Engineering for imparting their invaluable knowledge. My sincere thanks to the Federal University of Minas Gerais, CPH, and its employees for providing the essential infrastructure and equipment necessary for the development and execution of this work.

I am grateful to the CAPES agency for their financial support during this endeavor.

My heartfelt thanks to my friends and family for their unwavering support.

Finally, my appreciation goes out to all who directly or indirectly contributed to the completion of this work.

“Nobody is gonna hit as hard as life. But it ain't about how hard ya hit. It's about how hard you can get hit and keep moving forward. How much you can take and keep moving forward. That's how winning is done!”

Sylvester Stallone, Rocky Balboa

RESUMO

Com o uso crescente dos sistemas de conversão de energia eólica é importante estudar os diversos aspectos das diferentes tecnologias empregadas nesses sistemas. Um dos elementos mais importantes das tecnologias a velocidade variável é o conversor de potência, portanto, o projeto e avaliação do seu comportamento diante de diferentes condições operativas são de suma importância. Neste trabalho, uma modelagem térmica de um sistema de conversão de energia eólica (SCEE) usando como tecnologia o gerador de indução duplamente alimentado (*doubly-fed induction generator* - DFIG) é desenvolvida, a qual avalia o comportamento da temperatura de junção dos dispositivos semicondutores que compõem os conversores de potência do sistema. A tecnologia DFIG será a estudada por ser uma das mais usadas em usinas eólicas e ser severamente impactada pelos afundamentos momentâneos de tensão (AMTs). Como o sistema deve operar continuamente, surge a necessidade de se utilizar estratégias que visem a suportabilidade dos equipamentos aos AMTs, para que assim se atenda os códigos de rede. Estes estabelecem diretrizes para a conexão de usinas eólicas às redes elétricas que vão desde o estabelecimento de limites para desconexão durantes tais distúrbios, ao fornecimento de potência reativa para auxiliar na recuperação da rede. Desse modo, esse trabalho pretende investigar o comportamento das variáveis mais relevantes em um WECS que utiliza a tecnologia DFIG quando submetido aos AMTs. Será analisada a utilização de estratégias de controle que visam à melhoria da suportabilidade aos distúrbios citados avaliando os esforços térmicos dos componentes semicondutores. A metodologia empregada neste trabalho se baseia em desenvolvimentos matemáticos e simulações de um sistema de 2MW, implementada no *software* PLECS.

Palavras-chave: estresses térmicos; sistemas de conversão de energia eólica; gerador de indução duplamente alimentado; suportabilidade a afundamentos de tensão; afundamentos momentâneos de tensão; conversores de potência.

ABSTRACT

With the increasing prevalence of wind energy conversion systems, it has become imperative to delve into the diverse technologies employed within these systems. A crucial element for variable speed technologies is the power converter. Therefore, meticulous design and comprehensive evaluation of its performance under various conditions are of paramount importance. This study focuses on the thermal modeling of a Wind Energy Conversion System (WECS) utilizing the Doubly-Fed Induction Generator (DFIG) technology. The investigation centers on assessing the junction temperature behavior of the semiconductor devices within the power converters of the system. DFIG technology is chosen due to its widespread use in wind power plants, facing significant impact from momentary voltage sags (MVS). Given the continuous operation requirement of the system, supportability strategies are essential to enhance the system's response during MVS, ensuring compliance with grid codes. These codes set forth requirements for connecting wind farms to electricity grids, including disconnection limits during disturbances and the provision of reactive power to aid grid recovery. This study aims to explore the behavior of key variables in a WECS utilizing DFIG technology when subjected to MVS and the application of control strategies to enhance the system's Low-Voltage Ride-Through (LVRT) supportability. Furthermore, the research focuses on the power semiconductor components within the system, as these components may experience high thermal stresses during MVS. The electrical and thermal behavior of these devices are evaluated through simulations of a 2MW system implemented in PLECS software.

Keywords: thermal stresses; wind energy conversion systems; doubly-fed induction generator; low voltage ride-through capability; voltage sags; power converters.

FIGURE LIST

TABLE LIST

ABBREVIATION LIST

A-TVC	Advanced Transient Voltage Control
DOb	Disturbance Observer
CB	Circuit Breaking
CRTC	Current Reference Tracking Control
CSC	Current Source Converter
CT	Coupling Transformer
CVDPC	Combine Vector Direct Power Control
DCCC	DC-link Capacitor Crowbar
DDPMG	Direct Drive Permanent Magnetic Generator
DFR	Dual Frequency Resonant
DNC	Decentralized Nonlinear Control
DPC	Direct Power Control
DFIG	Doubly-fed Induction Generator
DSOGI	Dual Second-Order Generalized Integrator
DTC	Direct Torque Control
ESS	Energy Storage System
FCL	Fault Current Limiter
FFTCC	Feedforward Transient Current Control
FSCR	Feedback of the Stator Current Reference
GSC	Grid-Side Converter
GWEC	Global Wind Energy Council

HMC	Hybrid Multilevel Converter
IGBT	Insulated Gate Bipolar Transistor
ISS	Input-to-State Stability
LCCE	Laboratório de Controle e Conversão da Energia
LVRT	Low Voltage Ride-Through
MCC	Magnetizing Current Control
MCCR	Magnetizing Current Control + Resonant Control
MSDBR	Modulated Series Dynamic Braking Resistor
MST	Modified Super Twisting
MVS	Momentary Voltage Sag
NNDTIOC	Neural Discrete-Time Inverse Optimal Controller
NPC	Neutral-Point-Clamped
ONS	Operador Nacional do Sistema
PCC	Point of Common Coupling
PGRS	Parallel Grid-Side Rectifier
PI	Proportional-Integral
PIR	Proportional-Integral Resonant Control
PLL	Phase-Locked Loop
PMG	Permanent Magnetic Generator
PMSG	Permanent Magnetic Synchronous Generator
PWM	Pulse Width Modulation
RMS	Rotor Mean Square
RSC	Rotor-Side Converter

RTFC	Ride-Through Fault Capability
SCIG	Squirrel Cage Induction Generator
SDR	Series Dynamic Resistor
SDBR	Series Dynamic Braking Resistor
SFCL	Superconducting Fault Current Limiter
SMC	Sliding Mode Control
SMES	Superconducting Magnetic Energy Storage
SOSM	Second-order Sliding Mode
SPWM	Sinusoidal Pulse Width Modulation
SRSC	Series Rotor-Side Crowbar
SVC	Static VAR Compensator
SVPWM	Space Vector Pulse Width Modulation
STATCOM	Static Synchronous Compensator
UFMG	Universidade Federal de Minas Gerais
WECS	Wind Energy Conversion System
WT	Wind Turbine

Summary

Chapter 1. **INTRODUCTION**

1.1. Wind market

Wind energy has emerged as a compelling alternative in addressing the global energy crisis. In 2022, an impressive 77.6 GW of new capacity was integrated into power grids (see Figure 1.1), elevating the total installed wind capacity to 906 GW, marking a 9% growth compared to 2021, as illustrated in Figure 1.2.

Examining Figure 1.3, it becomes evident that the leading markets for new installations in 2022 were China, the USA, Brazil, Germany, and Sweden. Together, these countries accounted for a substantial 71% of global installations last year.

It is noteworthy to emphasize the significant role of Brazilian wind power, solidifying its position as one of Brazil's most robust energy generation sectors, boasting an impressive 25.6 GW of installed capacity in 2022 (GWEC, 2023). In light of this, it becomes particularly crucial to delve into the study and comprehension of these systems harnessing wind energy for power generation. The existing literature covers a broad spectrum of topics pertaining to wind energy conversion systems, including design, dynamic behavior, efficiency, grid integration, new technologies, and more.

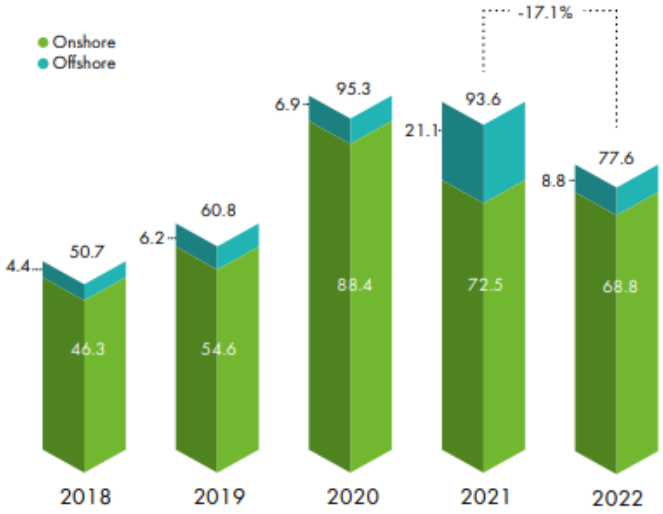

Figure 1.1 – Total world new installed capacity of WECSs (GWEC, 2023).

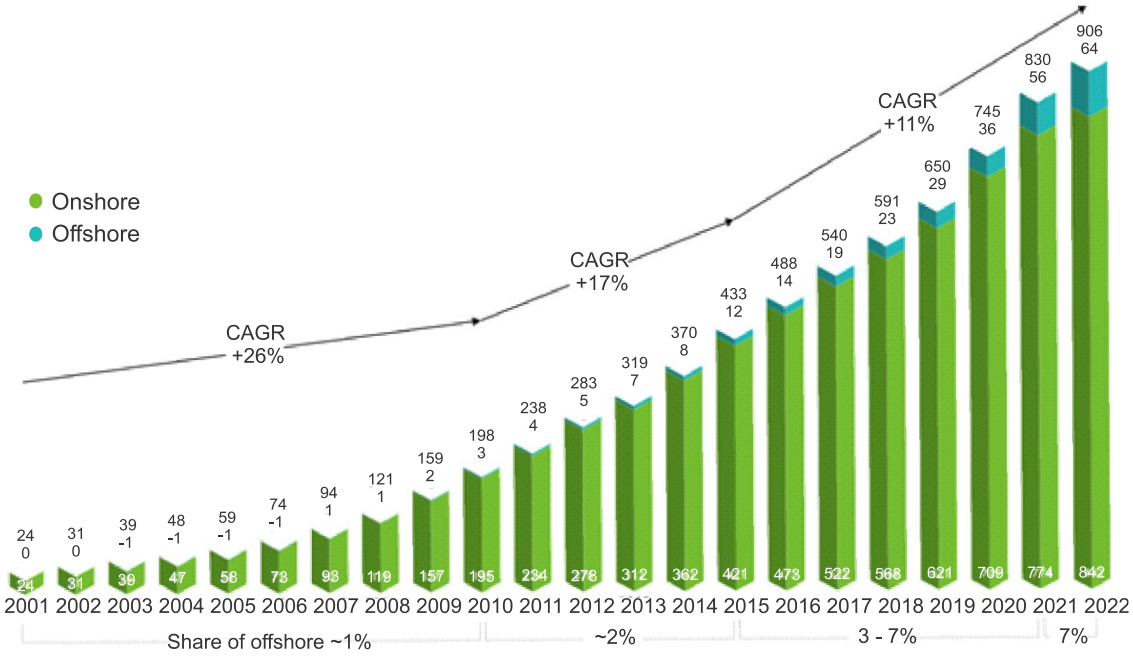

Figure 1.2 - Total world installed capacity of WECSs (GWEC, 2023).

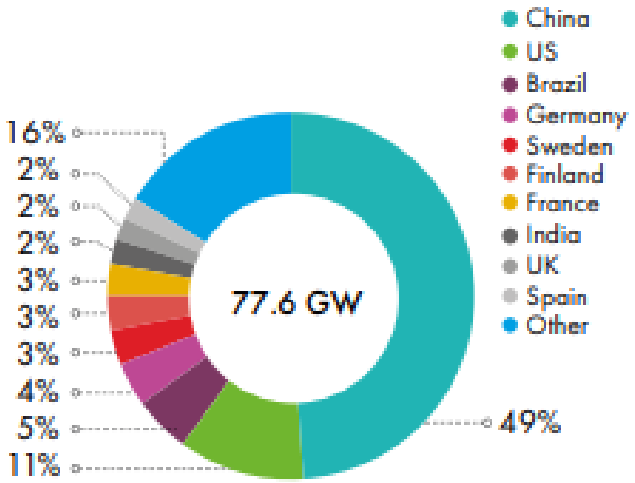

Figure 1.3 - Top markets of new wind power capacity in 2022 (GWEC, 2023).

1.2. Doubly-Fed Induction Generator (DFIG)

Wind energy conversion systems (WECS) typically consist of a wind turbine, an electric generator, a power electronic converter, and the corresponding control system, as depicted in Figure 1.4. However, it is worth noting that, depending on the technology, it may involve the use of a gearbox coupled to the wind turbine.

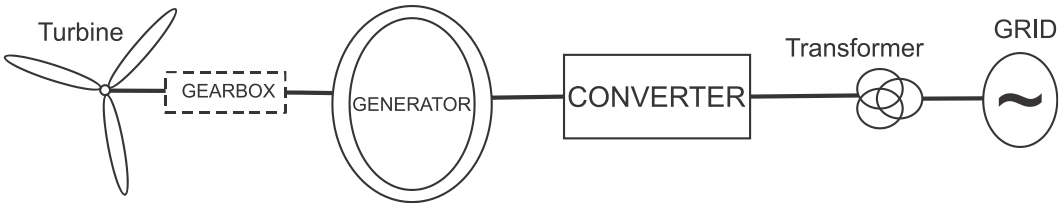

Figure 1.4 – Wind energy conversion system structure (Own authorship).

Among the machines employed in WECS, the doubly-fed induction generator (DFIG) stands out as one of the most prevalent, primarily due to its capability to operate at variable speeds. It offers the benefits of enabling active and reactive power control, all while requiring the converter to handle only a fraction of the rated generator power (typically between 20 – 30%).

According to GWEC (2021), the DFIG maintained its position as the predominant solution in 2021, capturing 50% of the market share. It was followed by the direct drive permanent magnetic generator (DD PMG), squirrel cage induction generator (SCIG), and medium-speed PMG.

In the Brazilian context, the situation is quite similar. As reported by ePowerBay (2022), the two leading wind turbine manufacturers in the country, responsible for approximately 52% of the total installed power, employ DFIG technology in their products. This underscores the significant presence of this technology in the country and underscores the importance of studying it.

The DFIG facilitates the conversion of mechanical energy produced by the turbine, which is then fed into the grid through the stator and rotor windings. The rotor windings are linked to an AC/DC/AC converter, while the stator windings are directly connected to the mains. The AC/DC/AC converter consists of two voltage-source converters linked via a DC link. This configuration, commonly referred to as a back-to-back converter, often employs insulated gate bipolar transistors (IGBTs) driven by pulse width modulation (PWM) schemes. Figure 1.5 provides a schematic representation of a DFIG-based WECS.

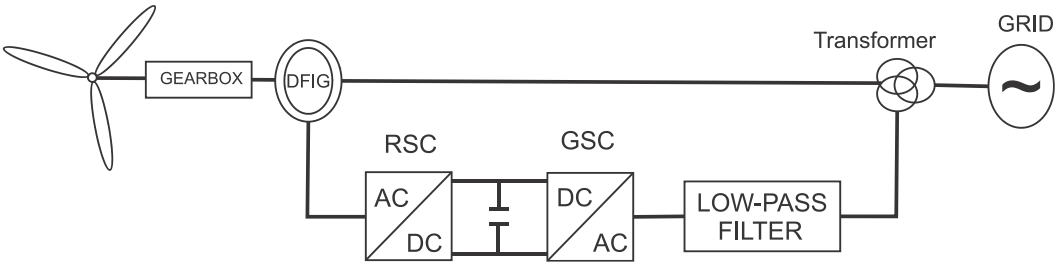

Figure 1.5 – Doubly-fed induction generator-based Wind energy conversion system (Own authorship).

As depicted in Figure 1.5, the rotor-side converter (RSC) is linked to the rotor windings and is tasked with regulating the rotor currents. Additionally, it influences the stator currents through magnetic coupling with the stator circuit, thus governing the power flow in the stator. Essentially, the RSC manages the active and reactive powers in the stator.

The grid-side converter (GSC) is connected to the grid via a low-pass filter, which serves to reduce the harmonic content introduced by the converter. This component is in charge of regulating the DC-link voltage and overseeing the flow of reactive power.

However, it is important to note that due to its architecture, which involves a decoupling between the electrical grid and the DFIG rotor through back-to-back converters, WECS systems utilizing DFIG technology may exhibit certain instabilities in grid frequency and electromagnetic torque (Ngamroo, 2017).

Liu et al. (2020b) elucidate strategies to alleviate instabilities in grid frequency by introducing an optimization model for controlling the parameters of DFIG wind farms through virtual inertia control. Wiam and Ali (2019) advocate for a modified Direct Torque Control (DTC) strategy designed to regulate the electromagnetic torque and rotor flux in WECS employing DFIG technology.

Moreover, it is worth noting that DFIGs exhibit a high sensitivity to grid disturbances, particularly voltage dips. A sudden decrease in grid voltage can lead to overvoltage and overcurrent in the rotor windings, potentially resulting in converter damage if proper protective measures are not in place (Eltamaly et al., 2020).

A momentary voltage sag (MVS) is defined by the Brazilian National Electric System Operator (ONS) as an event where the Root Mean Square (RMS) voltage falls

within the range of 0.1 per unit (pu) or higher, but less than 0.9 pu, and lasts for a duration between 1 cycle (16.67 ms) and 3 seconds(ONS, 2011).

The primary triggers of MVS include line overloads, the activation of large loads, and grid short-circuits. These events result in elevated currents and significant voltage reductions within the power system (Oliveira, 2016). MVS incidents can be categorized as phase-to-ground, phase-to-phase, phase-to-phase-to-ground, or three-phase. The characteristic profile of an MVS may vary depending on its source, typically marked by an abrupt initial drop followed by a more gradual recovery. Additionally, during a voltage sag, phase shifts can occur, leading to alterations in the voltage phase angle (Ren et al., 2021).

Mensou et al. (2020) introduce a novel Direct Power Control (DPC) method designed to regulate the DFIG stator powers and facilitate the operation of the aero-generator during balanced voltage dips. In contrast, Chang et al. (2022) provide analytical expressions for stator and rotor currents, taking into account variations in magnitude and phase angle for both positive and negative sequence voltages during unbalanced sags. Kashkooli et al. (2020) present an enhanced direct torque control approach for a DFIG under balanced voltage sags, incorporating transient flux damping.

Numerous studies have investigated the response of DFIGs to voltage sags. Chapter 2 of this work provides detailed explanations about voltage dips and also offers a compilation of studies that employ strategies to mitigate the detrimental effects stemming from such events. Therefore, the following listed works serve to offer an overview and further support the points mentioned earlier.

1.3. Grid codes

The WECS is obligated to adhere to grid codes that outline specific criteria for integrating wind power plants with the grid. One crucial requirement is the ride-through fault capability (RTFC). RTFC signifies the capacity of the power plant to sustain its connection to the grid even in the presence of voltage sags.

Since 2003, the (ONS) has mandated that WECSs must be equipped to continue operating without any disruption to power supply, even in the presence of abnormal grid voltage conditions (ONS, 2009). In a more recent update in 2019, the grid code also underscores the requirement for injecting reactive power to help the grid during faults.

Germany, the Netherlands, Spain, Denmark, and various other countries have established their own Ride-Through Fault Capability (RTFC) standards for their respective wind farms (Wu et al., 2019). These grid codes delineate unique RTFC criteria tailored to the specific characteristics of each country's grid. Figure 1.6 provides an illustration of the RTFC requirements specified in different grid codes (Energinet, 2016, Tennet, de España, 2006). The y-axis pertains to the voltage experiencing the most significant fluctuation, while the x-axis denotes the duration of the voltage sag.

The ability to supply reactive power to the grid during a voltage sag is also mandated by recent grid codes. This provision is crucial for supplying voltage support through the injection of additional positive sequence reactive current. Frequently, in tandem with this, there is also a decrease in the active power of the system. Figure 1.7 illustrates the reactive support curve in various grid codes. During low voltage ride-through (LVRT) operation, adhering to the grid code's stipulations for grid support is of paramount importance.

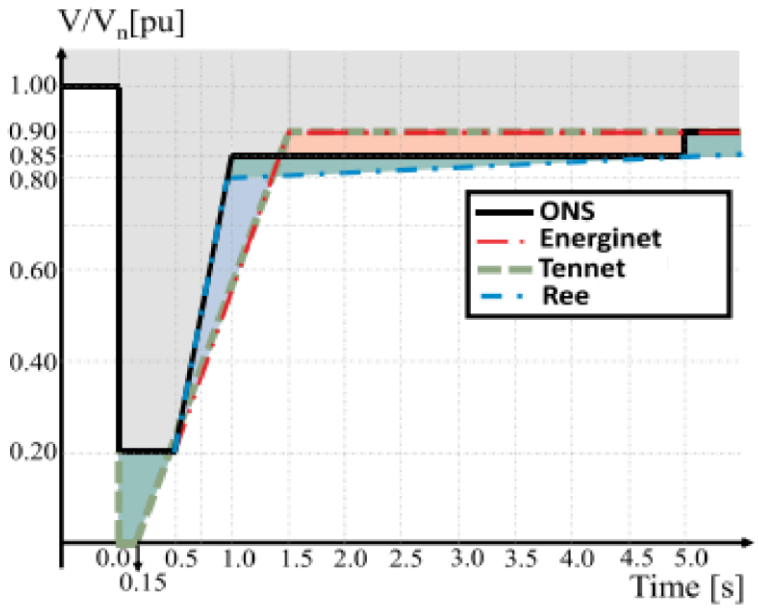

Figure 1.6 – Ride through fault capability curve established for different grid codes (Silva et al., 2020).

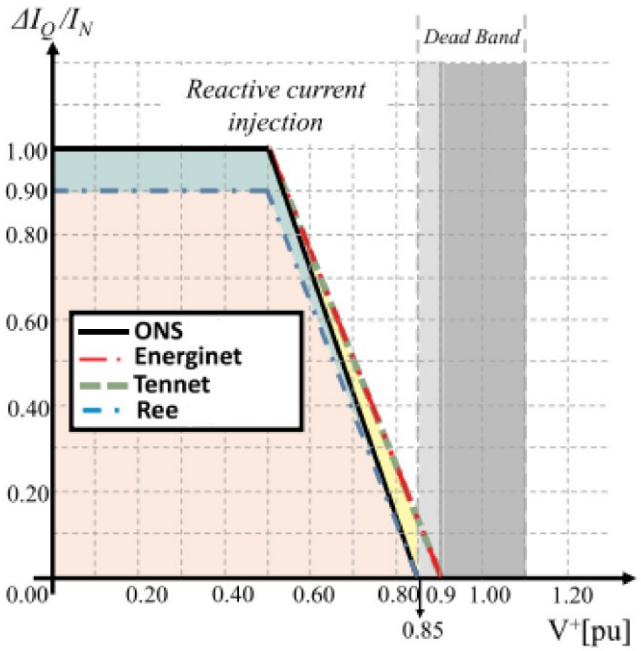

Figure 1.7 – Requirements for voltage support established for different grid codes (Silva et al., 2020).

The Brazilian grid code defines the RTFC curve, depicted in Figure 1.8, with specified thresholds for dynamic undervoltage and overvoltage (ONS, 2009). On the vertical axis, we have the remaining voltage in per unit (pu) at the shared connection point of the wind farm, while the horizontal axis represents the duration of the voltage sag. The shaded region in the graph indicates the sag amplitude and duration range during which the system should not disconnect from the grid. Furthermore, in addition to maintaining connection, the WECS is required to inject reactive power if the voltage falls below 0.85 pu, and absorb reactive power if the voltages exceed 1.1 pu, as depicted in Figure 1.9.

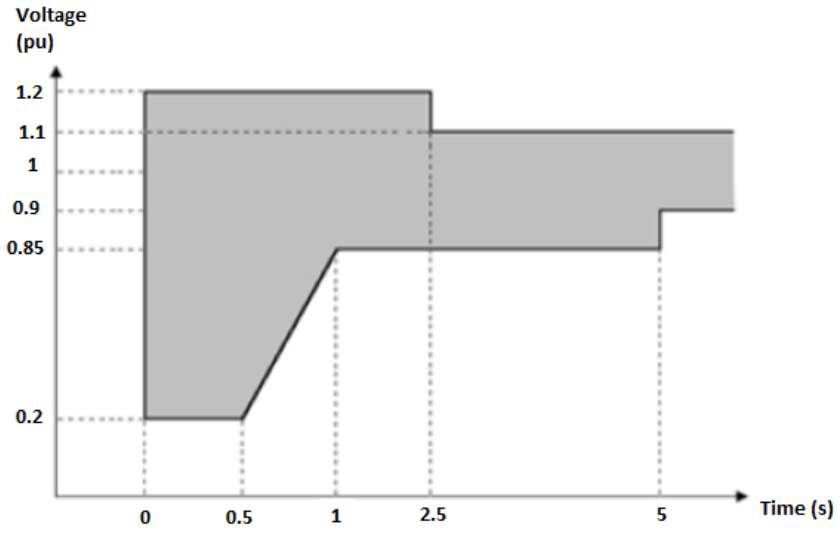

Figure 1.8 – RTFC curve required by the Brazilian grid code (Own authorship).

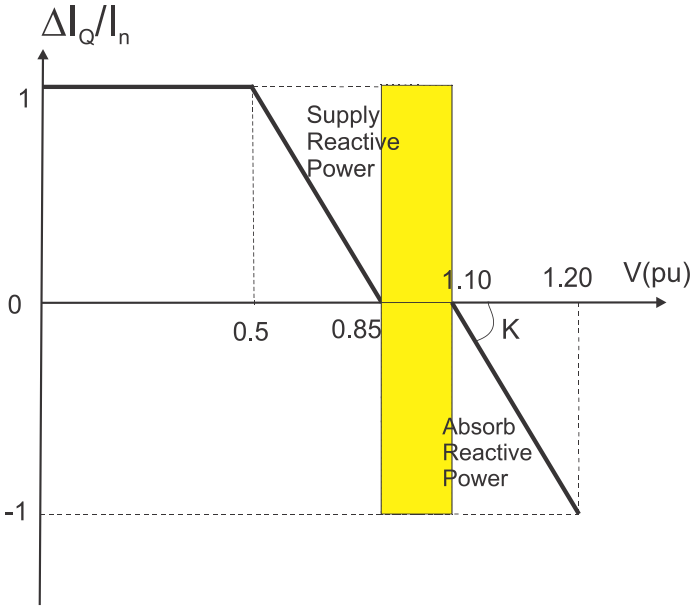

Figure 1.9 – Requirements for the injection of reactive power (Adapted from (ONS, 2009)).

The advent of dedicated grid codes for integrating WECS into the grid, which encompass ride-through fault capability requirements, has spurred a surge in recent publications centered on enhancing DFIG technology. These efforts primarily focus on devising novel strategies to improve the system's RTFC. These strategies may entail hardware solutions, involving alterations to the conventional structure or the incorporation of new components, as well as software-based solutions that primarily revolve around proposing advanced control strategies to augment the DFIG's RTFC. The subsequent chapter provides a thorough overview of these strategies, offering a comprehensive state-of-the-art assessment.

1.4. Objectives and methodology

Among the most vulnerable components in WECS, power electronic converters deserve special attention. The increasing significance of reliability and cost requirements for these power electronics compounds the challenge. In the case of reliability-critical components, such as power semiconductors and power capacitors, their thermal loading assumes paramount importance.

Studies have revealed that the dynamic changes in thermal stress represent one of the most critical factors leading to wear-out failures. Consequently, establishing an accurate model for thermal behavior becomes a crucial step in evaluating the reliability performance of power converters (Zhou and Blaabjerg, 2020).

In this context, the current study endeavors to conduct a thermal analysis of power semiconductor devices employed in DFIG-based WECSs. The objective is to explore the overall behavior and thermal stresses experienced by these devices during regular operational conditions, as well as in scenarios involving both balanced and unbalanced voltage sags.

Moreover, the research aims to assess, simulate, and compare ride-through fault control strategies. This evaluation will prioritize approaches that are both minimally complex and exhibit the most promising control implementations. The effectiveness, advantages, and limitations of each method will be considered concerning RTFC and the thermal stresses imposed on the semiconductors.

The development of this work comprises the fulfillment of several stages, which are briefly described below.

The first stage involves a comprehensive mathematical modeling of the DFIG and power converter to derive an equivalent model that will be used in designing the main components and formulating control strategies. Subsequently, computational simulations of a 2 MW system will be conducted using PLECS software to assess voltage and current profiles across the semiconductors. These results will allow for assessing the power converter, ensuring the system's safe operation under normal conditions. Additionally, this analysis will extend to investigating the thermal behavior of the system through simulations, including the study of overheating effects on these devices during voltage sags.

In the second stage, a comparative assessment of ride-through control strategies from existing literature will be conducted, with particular emphasis on the current and voltage stresses experienced by semiconductor devices during grid faults. Various strategies will be implemented in simulations, and their outcomes will be evaluated in the presence of grid disturbances. This process will yield a deeper comprehension of converter behavior and facilitate the formulation of strategies to mitigate the aforementioned stresses.

1.5. Contributions

As emphasized in Section 1.4, special attention is warranted for the thermal stresses experienced by power semiconductors, as the development of the thermal model directly impacts the investigation of system reliability. Therefore, the essence of this work lies in analyzing the thermal behavior of power semiconductors when implementing RTFC control strategies for wind energy conversion systems utilizing DFIG technology.

This work also highlights the following contributions, outlined below:

- A comprehensive bibliographic review about methods for LVRT improvement in DFIG-based WECSs and their comparison;
- Investigation of the thermal behavior of DFIG semiconductors considering the occurrence of grid voltage sags, especially during unbalanced dips;
- Evaluation and comparison of LVRT strategies from the point of view of the stresses on semiconductors.

The results of the research until now were reported in the following papers:

[P1] DE OLIVEIRA, I. R., TOFOLI, F. L. & MENDES, V. F. 2019. Thermal Modeling of Converters for Wind Conversion Systems Employing DFIG Technology. *IEEE 15th Brazillian Power Electronics Conference and IEEE 5th Southern Power Electronics Conference (COBEP/SPEC).* Santos - Brazil.

[P2] DE OLIVEIRA, Igor Rodrigues; TOFOLI, Fernando Lessa; MENDES, Victor Flores. Thermal Analysis of Power Converters for DFIG-Based Wind Energy Conversion Systems during Voltage Sags. Energies, v. 15, n. 9, p. 3152, 2022.

1.6. Text Organization

The first chapter offers a concise overview of the global landscape surrounding the utilization of wind energy. It outlines the components comprising a WECS based on DFIG technology and provides a comprehensive assessment of the state-of-the-art of DFIGs, including their inherent strengths and weaknesses. Additionally, a succinct explanation of voltage sags is provided, with a particular focus on RTFC. The chapter also outlines the motivation, objectives, methodology, and anticipated contributions of the study.

The second chapter delves into the mathematical modeling of DFIG, providing a detailed description of all induction machine equations. Additionally, it addresses the behavior of DFIG under both balanced and unbalanced sags. The chapter also conducts a review of prevalent RTFC strategies found in existing literature, emphasizing their fundamental operating principles, structures, and classifications.

The third chapter encompasses the electrical modeling and outlines the control methodology employed. It also includes a concise state-of-the-art presentation, highlighting crucial aspects of thermal analysis for power semiconductor devices. The chapter further provides detailed insights into thermal modeling and expounds upon the parameters utilized for system simulation. Additionally, various ride-through control strategies sourced from existing literature, tailored for both balanced and unbalanced dips, are subjected to a comprehensive analysis. This includes an in-depth examination of the magnetizing current control (MCC) strategy, developed by the Energy Control and Conversion Laboratory (LCCE) at the Federal University of Minas Gerais.

Chapter 4 presents the outcomes of the system simulation, focusing on the performance of the MCC strategy in comparison to other LVRT strategies. The analysis and discussion delve into the thermal stresses experienced by the semiconductors. The chapter also includes a comparative assessment of these strategies from a thermal perspective, highlighting their respective strengths and weaknesses. Moving forward, Chapter 5 encapsulates the primary conclusions drawn from the study and outlines potential avenues for future research.

Chapter 2. DOUBLY-FED INDUCTION GENERATOR AND RIDE-THROUGH FAULT CAPABILITY

2.1. DFIG mathematical modeling

The equations that represent the mathematical model of the classical induction machine are described as follows. The stator and rotor differential equations are in the synchronous reference frame as defined in (Kovács, 1983):

$$\vec{v}_s = R_s \vec{i}_s + \frac{d\vec{\psi}_s}{dt} + j\omega_s \vec{\psi}_s \tag{2.1}$$

$$\vec{v}_r = R_r \vec{i}_r + \frac{d\vec{\psi}_r}{dt} + j\omega_r \vec{\psi}_r \tag{2.2}$$

where the variables and the parameters are referred to the stator. The subscripts s and r refer to the variables and parameters of the stator and rotor, respectively; v_s and v_r are voltages, i_s and i_r are currents; ω_s and ω_r are angular frequencies; ψ_s and ψ_r are flux linkages, R_s and R_r are resistances.

The stator and rotor flux linkages ψ_s and ψ_r are given by:

$$\vec{\psi}_s = L_s \vec{i}_s + L_m \vec{i}_r = (L_{\sigma s} + L_m)\vec{i}_s + L_m \vec{i}_r \tag{2.3}$$

$$\vec{\psi}_r = L_r \vec{i}_r + L_m \vec{i}_r = (L_{\sigma r} + L_m)\vec{i}_r + L_m \vec{i}_s \tag{2.4}$$

where L_s, L_r are self-inductances; $L_{\sigma s}$, $L_{\sigma r}$ are leakage inductances; and L_m is the magnetizing inductance.

The differential equation that describes the mechanical system is:

$$J\frac{d\omega_m}{dt} + k_f \omega_m = T_e - T_{mec} \tag{2.5}$$

where J is the inertia moment of the mechanical system (turbine + generator); k_f is the friction coefficient; T_{mec} is the mechanical torque in the generator axis provided by the

wind turbine through the gearbox; and T_e is the machine electromagnetic torque calculated by:

$$T_e = \frac{3}{2} p \frac{L_m}{L_s} \Im m\left\{\vec{\psi}_s \hat{}\right\} \quad (2.6)$$

where p is the number of poles of the machine and the superscript "^" denotes the complex conjugate.

These mathematical expressions provide the basis for understanding and modeling the behavior of the DFIG during voltage sags, which are discussed in the next section. Furthermore, in 0 it will also contribute to the development of control strategies.

2.2. DFIG behavior during voltage sags

This section models the DFIG behavior during the occurrence of balanced and unbalanced voltage sags.

2.2.1. Balanced voltage sags

To carry out the theoretical analysis involving the influence of MVSs in DFIGs, the dynamic models of the induction machine are used, which are represented by equations (2.1) to (2.4). This development is based on (Lopez et al., 2007).

In this section, balanced three-phase sags are discussed, as they are the simplest phenomena that represent a particular case of the unbalanced sags, as discussed in the next section. It is assumed that the stator voltage drops instantly from its initial rated value (Vs) to a value V_2 at instant $t = t_0$:

$$\vec{v}_s \quad \begin{cases} {}^{j\omega_s t} = V_1 e^{j\omega_s t}, & t < t_0 \\ \left\lfloor V_2 e^{j\omega_s t}, \right. & t \geq t_0 \end{cases} \quad (2.7)$$

In DFIGs, the currents are controlled by manipulating the voltages imposed on the rotor through the RSC. Thus, the variable of interest for the control system is the rotor voltage, which can be obtained from equations (2.2), (2.3), and (2.4) as:

$$\vec{v}_r \quad L_s \left(\frac{d}{dt} - j\omega \right) \vec{\psi}_s \cdot \left[\cdot \cdot_r \cdot \sigma L_r \left(\frac{d}{dt} - j\omega \right) \right] \vec{\imath}_r \quad (2.8)$$

Equation (2.8), which is in the rotor reference frame, represents the voltage synthetized by the RSC during the normal operation. The first term of this equation is the rotor voltage portion coming from the stator flux, i.e., the induced voltage in the rotor, and the second one is the portion due to the voltage drop caused by the rotor impedances.

The dynamic behavior of the stator flux, expressed by the equation (2.1), depends on the stator voltage, i.e., the grid voltage and the current that flows through the stator. Neglecting the voltage drop in the stator resistance, that is generally small, the stator flux in steady state can be expressed as:

$$\vec{\psi}_s \qquad \frac{t}{j\omega_s} \tag{2.9}$$

where V_s is the stator peak phase voltage and ω_s is the stator angular frequency. Substituting (2.9) in (2.8) results in the rotor voltage in normal operation, expressed by:

$$\vec{\quad}_r \quad \vec{\quad}_s \; L_s \; \left[R_r + \sigma L_r \left(\frac{d}{dt} - j\omega \right) \right] \vec{\quad}_r \tag{2.10}$$

where s is the machine slip. From equation (2.10), it is possible to verify that generally, for a large generator, the second term is relatively smaller than the first one because the rotor resistance and the transient inductance (σL_r) are often small. Thus, the voltage induced in the rotor depends almost exclusively on the stator flux, which depends on the stator voltage (Equation 2.9).

As the term of the voltage drop in the rotor impedance is relatively small, a first approximation analyzes the behavior of the machine during an MVS considering an open-circuit rotor, i.e., $\left(\vec{\quad}_r - \upsilon\right)$. Therefore, the focus is to analyze the behavior of the voltage induced in the rotor.

Considering $\vec{\quad}_r - \upsilon$, equations (2.1) and (2.2) result in:

$$\frac{d\vec{\psi}_s}{dt} = \vec{\quad}_s \qquad L_s \; \vec{\quad}_s \tag{2.11}$$

Before the dip at $t<t_0$, the stator flux is in steady state and totally produced by the voltage on the stator, i.e., there is only the presence of the forced system response. Thus, equation (2.9) becomes:

$$\vec{\psi}_{s_{f1}} \qquad \frac{\omega_s t}{j\omega_s} \tag{2.12}$$

This flux is used as an initial condition for solving Equation (2.11) to calculate the flux at the moment that the voltage dip occurs. Assuming that the sag occurs at $t_0 = 0$, i.e., at the beginning of the sag the voltage is at the value maximum (worst case condition), the stator flux response is given by:

$$\vec{\psi}_s \qquad j\omega_s \qquad j\omega_s \qquad \vec{r}_{s_{f2}} \qquad \vec{r}_{s_n} \tag{2.13}$$

where $\tau_s = \frac{L_s}{R_s}$ is the stator time constant, $\vec{\psi}_{s_{f2}}$ is the forced response due the remaining voltage during the sag; and $\vec{\psi}_{s_n}$ is the natural flux that is induced during the stator voltage transient. Note that the first term is constant and rotates with synchronous frequency in the complex plane, while the second one is a fixed vector, whose amplitude decays with the stator time constant.

Looking at equation (2.8) and (2.13), one can see that the two flux components induce voltage components in the rotor. Through equation (2.10) and considering $i_r = 0$, the induced voltage in the rotor caused by the forced flux yields:

$$\vec{\quad}_f \qquad 2 \frac{m}{L_s} s e^{j\omega_s t} e^{-j\omega t} = V_2 \frac{L_m}{L_s} s e^{j\omega_r t} \tag{2.14}$$

This equation is in the rotor reference frame denoted by the superscript "*r*".

The voltage produced by natural flux, obtained by replacing $\vec{\psi}_{s_n}$ in the equation (2.8) yields:

$$\vec{\quad}_{r_n} \qquad L_s \left(\frac{1}{\tau_s} + j\omega \right) \frac{V_1 - V_2}{j\omega_s} e^{-t/\tau_s} e^{-j\omega_s t} \tag{2.15}$$

Thus, the total voltage is expressed by:

$$\vec{r}_a \quad \vec{r}_f \quad \vec{r}_n = \frac{L_m}{L_s}\left(V_2 s e^{j\omega_r t} - \left(\frac{1}{\tau_s} + j\omega \right) \frac{V_1 - V_2}{j\omega_s} e^{-t/\tau_s} e^{-j\omega t} \right) \tag{2.16}$$

Analyzing equation (2.16), it is observed that the first term has amplitude and frequency considerably lower than the second parcel. This is because within the DFIG operation range the slip is low. The second term has a frequency equal to rotor electric frequency. From Equation (2.16), it is noticed that voltage amplitude will be greater as the sag and machine rotational speed increase.

It is possible to deduce the maximum rotor voltage amplitude through the manipulation of equation (2.16), resulting in a maximum voltage approximately equal to:

$$\left| \vec{r}_{a\,\max} \right| \quad \frac{m}{L_s}\left(V_2 |s| + (1-s)(V_1 - V_2) \right) \tag{2.17}$$

The worst case, i.e., when the voltage reaches the maximum value occurs when the remaining voltage (V_2) is zero and the speed is as high as possible.

The rotor voltage reaches its highest value when the sag occurs when the stator voltage passes through a maximum point. In this case, the maximum voltage appears right at the beginning of the dip. If the voltage in the stator is passing through zero when the sag occurs, the maximum induced voltage will appear one-fourth cycle after the initial instant. If the stator constant time is high, the maximum voltage reached will be close in both cases, but if it is small, the second case will present a lower maximum voltage.

A more in-depth analysis of the DFIG behavior during balanced voltage sags can be found in Mendes (2009) and Mendes (2013), where the main conclusions can be stated for the balanced voltage sags:

- In balanced sags, the main problem is the natural flux component which induces large voltages in the rotor, causing high oscillatory currents that can damage the inverter;

- The oscillations produced by the natural component are reflected in torque pulsations that are unacceptable form the point of view of mechanical coupling between generator and turbine, and in power swings that are undesirable for the electric system.

2.2.2. Unbalanced voltage sags

For the theoretical analysis of unbalanced MVSs, the classical equations of the induction machine will also be used, corresponding to equations (2.1) to (2.4). Equations (2.8) to (2.11) as derived in the previous section will also be useful in the mathematical analysis of the effects of unbalanced sags in DFIGs. This development is based on (López et al., 2008).

While in a balanced three-phase system there is only positive-sequence voltage component, negative-sequence component also appears during a voltage unbalance (Bollen, 2000). Therefore, to analyze the behavior of the DFIG, the theory of symmetric components is used (Wagner and Evans, 1933), in addition to the superposition theorem as it will be shown.

Decomposing the stator voltage into symmetric components gives:

$$\vec{v}_s = \vec{v}_+ + \vec{v}_- + \vec{v}_0 \tag{2.18}$$

where $\vec{v}_+$, $\vec{v}_-$, and $\vec{v}_0$ are the positive-, negative-, and zero-sequence components, respectively. Using the Fortescue transformation (Fortescue, 1918), these components can be given by:

$$\begin{bmatrix} \vec{v}_+ \\ \vec{v}_- \\ \vec{v}_0 \end{bmatrix} = \frac{1}{3}\begin{bmatrix} 1 & \vec{a} & \vec{a}^2 \\ 1 & \vec{a}^2 & \vec{a} \\ 1 & 1 & 1 \end{bmatrix}\begin{bmatrix} v_{s_a} \\ v_{s_b} \\ v_{s_c} \end{bmatrix} \tag{2.19}$$

where $\vec{a} = e^{j\frac{2\pi}{3}}$.

Considering a machine with symmetrical impedances, the positive- and negative-sequence components generate fluxes that rotate with the synchronous speed, but in the opposite direction with each other, while the zero-sequence component does not produce

any flux (López et al., 2008). Using the superposition theorem, the steady state stator flux is given by the sum of the forced fluxes due to the positive-sequence component ($\vec{\psi}_{s_+}$) and the negative-sequence component ($\vec{\psi}_{s_-}$). When a transition occurs, a natural flux produced by each one of these components appears ($\vec{\psi}_{s_+}$,$\vec{\psi}_{s_-}$). Therefore, there are four terms, two forced and two natural fluxes, whereas the natural components can be grouped as they depend only on the initial flux condition:

$$\vec{\psi}_s \quad \vec{\psi}_{s_+} \cdot \vec{\psi}_{s_-} \cdot \vec{\psi}_{s_{n_+}} \cdot \vec{\psi}_{s_{n_-}} \quad \vec{\psi}_{s_+} \cdot \vec{\psi}_{s_-} \cdot \vec{\psi}_{s_n} \tag{2.20}$$

Similarly to the case where there is only positive-sequence component, the stator flux terms induce rotor voltages that summed together become:

$$\vec{\cdot}_r \quad \vec{\cdot}_{r_+} \cdot \vec{\cdot}_{r_-} \cdot \vec{\cdot}_{r_n} \tag{2.21}$$

Considering an open-circuit rotor (I_r=0), solving equation (2.11) and ignoring the voltage drop in the stator resistance during the sag, the forced fluxes for each symmetric component are:

$$\vec{\psi}_{s_+} \quad j\omega_s \, e^{j\omega_s t} \tag{2.22}$$

$$\vec{\psi}_{s_-} \quad j\omega_s \, -e^{-j\omega_s t} \tag{2.23}$$

Thus, the forced voltages induced in the rotor by these fluxes, obtained through equation (2.10), are in the rotor reference frame (superscript "*r*") equal to:

$$\vec{\cdot}_{r_+} \quad \cdot + \frac{m}{L_s} s e^{j\omega_s t} \tag{2.24}$$

$$\vec{\cdot}_{r_-} \quad \cdot - \frac{n}{L_s}\left(s-2\right)e^{-j(2-s)\omega_s t} \tag{2.25}$$

The voltage induced by the positive sequence has an amplitude proportional to the slip, therefore small, as its rotation frequency is small as well. The amplitude of the voltage induced by the negative sequence includes a factor of 2, which can be large if the

asymmetry also is. The frequency is close to twice the grid frequency, thus, large when compared with the positive-sequence component.

Observing equations (2.22) and (2.23), it is verified that the fluxes due to each of the components rotate in the opposition to each other .Thus, the instant at which the sag occurs influences the behavior of these variables during the transient. When the dip occurs, if the positive- and negative-sequence fluxes are in opposition, they are subtracted resulting in a flux equal to the one before the fault, with no natural flux induced in the rotor. If at the instant that the dip occurs the flux are aligned, they will add up and the largest possible natural flux for that sag will appear. In this condition, the natural flux will be given by the sum of the natural fluxes for each of the components, that is:

$$\vec{\psi}_{s_n} \quad \vec{\psi}_{s_{n+}} \cdot \vec{\psi}_{s_{n-}} \qquad \frac{V_+ - V_-}{j\omega_s} e^{-t/\tau_s} \tag{2.26}$$

where it was considered that the voltages are balanced before the sag, as there is only the positive-sequence component ($V_+(t<0) = V_1$ and $V_-(t < 0) = 0$. For this condition, the induced voltage is given by:

$$\vec{\cdot}_{r_n} \qquad L_s \left(\frac{1}{\tau_s} + j\omega \right) \frac{(V_1 - V_+ - V_-)}{j\omega_s} e^{-t/\tau_s} e^{-j\omega_s t} \tag{2.27}$$

A more in-depth analysis of the DFIG behavior submitted to unbalanced sags is found in (Mendes, 2009) and Mendes (2013), where the main conclusions can be stated for the unbalanced voltage sags as follows:

- In unbalanced sags, the negative sequence component of the rotor voltage is the main cause of excessive rotor overcurrents.
- Unlike the balanced three-phase case, where the impact is caused only by the natural transient component, these overcurrents are present throughout the dip.
- In the unbalanced case, the problem is even worse when there is the presence of the natural component, since the overcurrents may be caused by the sum of natural and negative sequence components.
- Torque and power will have oscillations with higher amplitude as a consequence of current oscillations.

2.3. RTFC strategies

As shown in the last sections, the voltage sags affect the DFIG-based systems significantly. Therefore, in the last decade several works proposed different strategies to improve the system behavior, guarantying the RTFC.

RTFC techniques can encompass the integration of supplementary hardware into the system, or they can adopt control strategies to enhance overall dynamic performance (Qin et al., 2020). Consequently, the cited works will be categorized into two groups: techniques involving additional hardware and those employing control strategies.

2.3.1. Additional hardware techniques

Figure 2.1 illustrates some examples of the main strategies found in the literature that use additional equipment.

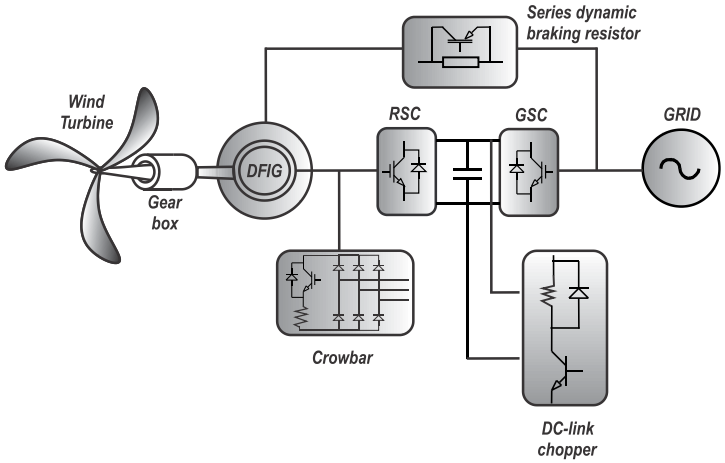

Figure 2.1 – Protection equipment present in WECS (Adapted from (Baiju and Rajeev, 2015)).

The crowbar is a conventional method using a resistive network connected to the rotor circuit as a protection of rotor overcurrents and DC-link overvoltages.

The activation of the crowbar is temporary, meaning that during normal operation, the device remains inactive. It is only triggered in the event of a fault. Once the fault is resolved, the device is deactivated again. When the crowbar is engaged, the RSC semiconductors are disabled, compromising the control of the DFIG during the crowbar operation. This constitutes the primary drawback of this device. Haidar et al. (2017), Döşoğlu (2020), and Xiao et al. (2023) have introduced control strategies focused on the activation and deactivation of the crowbar, accompanied by simulation results.

Another drawback is the substantial amount of reactive power drawn from the grid when the crowbar is active, leading to additional voltage degradation. This phenomenon arises because, with the crowbar circuit linked to the rotor, the machine emulates the behavior of a squirrel-cage induction generator characterized by the high rotor resistance and slip. Swain and Ray (2017) propose an innovative scheme for a crowbar circuit that enhances both active and reactive power profiles. It is noteworthy that the crowbar consists of resistors, leading to a substantial energy consumption during its activation.

Onishi et al. (2023) conduct an analysis on the operation of crowbars in DFIGs, exploring the effects of crowbar deactivation timing. They propose an improvement algorithm based on simulation results. Consequently, careful calculation of crowbar resistances is essential to ensure sufficient damping and minimal energy consumption. Figure 2.2 illustrates the electrical diagram of the crowbar method.

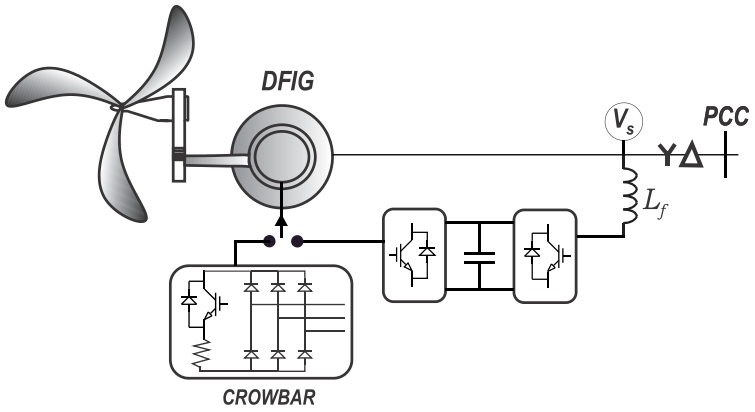

Figure 2.2 – Electric design of the crowbar method (Adapted from (Lima et al., 2010)).

The Energy Storage System (ESS) has found extensive applications in power systems, including wind systems and modern grids. To store the generated power effectively, it is imperative to convert it into alternative forms of energy, such as chemical or mechanical energy (Palizban and Kauhaniemi, 2016). Nadeem et al. (2018) and He et al. (2021) present a review of ESS, listing the challenges and impacts of power systems.

Kim et al. (2019) present an implementation of an ESS in a DFIG-WT system. In this setup, the ESS serves as a buffer in DFIG wind systems, maintaining DC-link power flow through charging/discharging processes. Figure 2.3 illustrates a DFIG-based WECS equipped with an ESS, configured indirectly. Here, the battery is connected in parallel with the DC link through a DC/DC converter, enabling the ESS and GSC to share the DC

link. Additionally, the ESS can offer reactive power support by injecting an additional demagnetizing current (Qin et al., 2020).

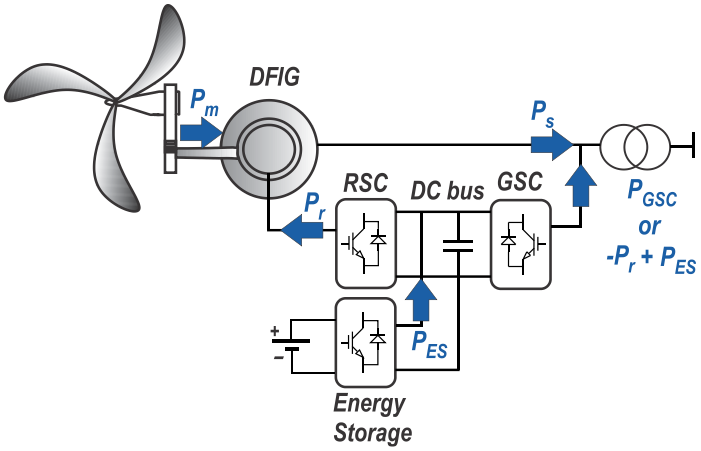

Figure 2.3 – WECS associated with an ESS (Adapted from (Kim et al., 2019)).

Tourou et al. (2017) propose a similar deployment of an ESS with a DFIG, utilizing a direct configuration. In this arrangement, the ESS is connected in parallel to the DC link without the presence of a DC/DC converter. This configuration offers a lower cost and higher efficiency compared to the indirect configuration. Furthermore, the direct DC-link ESS is capable of smoothing active power variations delivered to the grid during voltage dips. However, it is important to note that the demagnetizing current injected from converters into the rotor circuit may lead to rotor overcurrent (Qin et al., 2020).

Alternative methods, such as the use of a braking resistor (DC chopper), can be employed and combined. This involves connecting the DC chopper in parallel with the DC-link capacitor to restrict overcharging during fault conditions (Okedu et al., 2012, Pannell et al., 2013). Figure 2.4 illustrates an electrical schematic of the DC chopper.

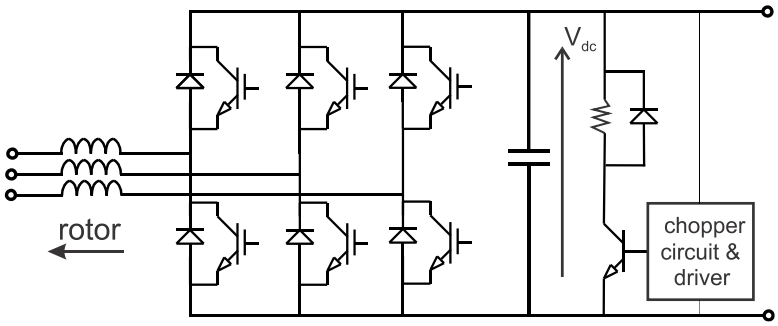

Figure 2.4 – Electrical schematic of DC chopper (Adapted from (Pannell et al., 2013)).

The DC chopper functions as a straightforward protective device that creates a short circuit in the DC-link through a power resistor when the DC-link voltage surpasses a predetermined threshold. The brake serves to control the DC-link voltage while accommodating transient rotor overcurrents. An insulated gate biolar transistor- (IGBT) based chopper circuit is generally employed to swiftly connect and disconnect the resistor. The chopper operates based on a hysteresis band, meaning that the turn-off voltage is set below the turn-on threshold. The inclusion of an antiparallel diode across the braking resistor is necessary to account for stray inductance effects when the chopper is switched off.

Naderi et al. (2019) propose a modified DC chopper capable of not only controlling DC-link voltage but also limiting rotor overcurrents. In contrast to the traditional configuration, this modified setup incorporates three additional semiconductor switches for inserting the chopper resistor in parallel with the DC-link capacitor.

The Series Dynamic Resistor (SDR) is a resistor connected in series between the rotor windings and the RSC in the event of a voltage sag. The primary role of the SDR is to restrict the acceleration of the rotor during fault conditions (Gray et al., 2016).

The Series Dynamic Braking Resistor (SDBR) consists of a resistor in parallel with a switch, commonly an IGBT, as depicted in Figure 2.1 . The SDBR is designed to elevate terminal voltage during grid voltage dips by introducing resistance into the stator circuit (Alam et al., 2018). This strategy has a significant drawback as it necessitates deactivating the back-to-back converter upon activation. The difficulty arises in synchronizing stator voltage, coupled with the challenges posed by the variable frequency switching scheme. These issues can potentially result in a deterioration of voltage quality (Huang et al., 2014).

To address these challenges, Keshavarzi and Ali (2019) proposed a modulated series dynamic braking resistor (MSDBR). The MSDBR incorporates a high-power braking resistor in parallel with two IGBTs arranged in an antiseries configuration for each phase, as described in Figure 2.5. Furthermore, Okedu (2019) suggests integrating a parallel capacitor with the MSDBR to enhance the performance of DFIG-WT during voltage sags. Simulation results from this study indicate that the proposed hybrid control scheme effectively limits rotor overvoltage and restricts DC bus overvoltage.

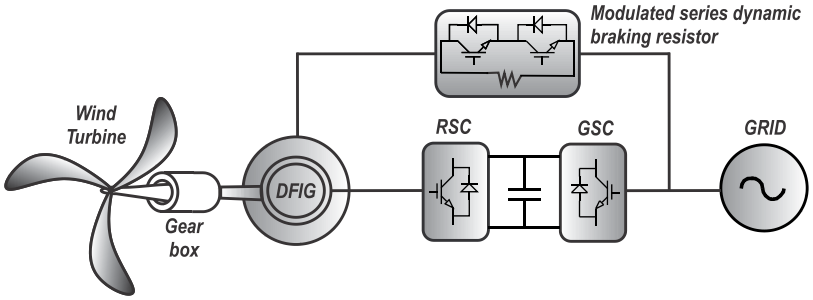

Figure 2.5 - Electric scheme of MSDBR (Own authorship).

In Abdelsalam et al. (2014), a novel current-source-converter- (CSC-) based back-to-back topology is introduced as shown in Figure 2.6. This topology addresses the limitations of conventional converters, such as overvoltage experienced by switches during commutation. The system boasts a simple and easily controllable structure, reduced switching frequency, and the capability for maximum power point tracking with controllable grid active and reactive powers. While this RTFC method is passive and straightforward, Dai et al. (2010) also discuss a method to control the DC-link current by managing the GSC.

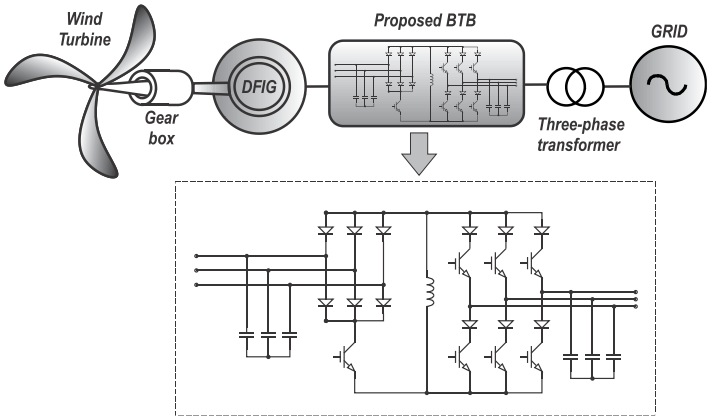

Figure 2.6 - Electrical schematic of CSC-based BTB topology (Own authorship).

Flannery and Venkataramanan (2008) propose an alternative strategy employing a parallel grid-side rectifier (PGRS) with a series GSC. This combination facilitates straightforward power processing and robust ride-through capability during voltage disturbances. A series-connected GSC is employed to inject DC-link power into the grid. While this approach allows for power flow control within the typical operating range—above and below synchronous speed—it faces limitations at subsynchronous speeds. To overcome this, a parallel-connected passive rectifier, rated at a fraction of the total power, is incorporated to optimize overall system utilization. Figure 2.7 illustrates this strategy.

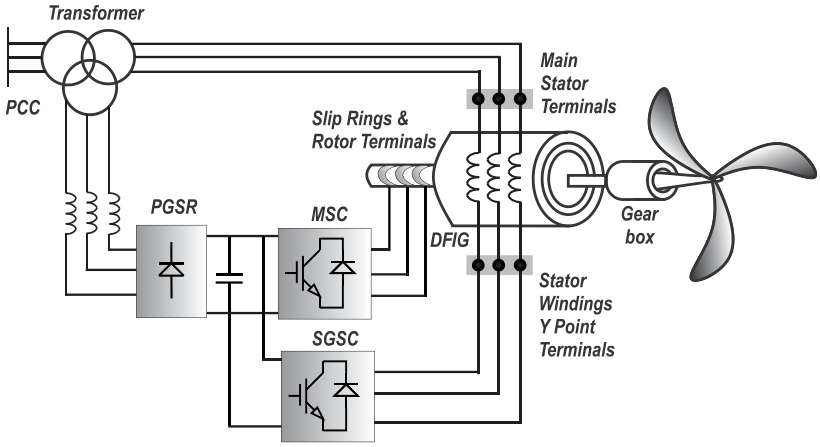

Figure 2.7 – WECS using PGRS (Adapted from (Flannery and Venkataramanan, 2008)).

Fault current limiters (FCLs) are devices designed to restrict the magnitude of current flowing through a circuit during a fault condition. They play a crucial role in safeguarding electrical equipment from damage caused by excessively high fault currents. Additionally, FCLs contribute to enhancing the overall reliability of electrical systems by preventing the spread of faults and minimizing the risk of outages (Baimel et al., 2021, Chen et al., 2022, Demin et al., 2023, Elshiekh et al., 2021).

Baimel et al. (2021) propose an active bridge FCL to enhance the transient stability of DFIG wind farms. Experimental results from the benchmark system demonstrate improved transient stabilities, achieved by limiting peak currents, minimizing terminal voltage drops, and mitigating transients in active and reactive powers and torque. Likewise, Demin et al. (2023) showcase an enhancement in wind turbine transient stability using a similar strategy. This approach effectively curtails fault currents throughout the fault period, leading to a reduction in torque oscillations.

A Superconducting Fault Current Limiter (SFCL) is a type of FCL that leverages superconductivity to restrict the current flow through a circuit during a fault. In the event of a fault, the current through the SFCL coil experiences a sharp increase. This leads to the quenching of the superconducting material, causing it to lose its superconducting properties. Consequently, the coil resistance rises rapidly, effectively limiting the current flowing through the circuit (Chen et al., 2014, Gonçalves Sotelo et al., 2022, Oliveira et al., 2015).

While SFCLs are still in the developmental stage, several pilot projects have been successfully implemented, as evidenced by Lim et al. (2013), Islam et al. (2020), Islam

et al. (2022) in the literature. As this technology continues to mature, SFCLs are anticipated to see broader deployment in electrical systems.

Elshiekh et al. (2021) proposed a circuit configuration that integrates a FCL with a SMES to improve the transient stability of DFIG-WTs under various operating and fault conditions. The effectiveness of the energy storage function and current limitation is demonstrated through experimentation on a small-scale test bench.

Amorim et al. (2021) introduce a novel topology for the back-to-back converter that utilizes full-bridge modules connected in series with a traditional converter, incorporating a Hybrid Multilevel Converter (HMC) structure on the rotor side. The new topology is illustrated in Figure 2.8. This research proposes a method to protect the DFIG from undesirable effects induced by the natural component, such as the generation of higher voltages in the rotor circuit. In normal operating conditions, the system performs the standard switching of the RSC. However, during fault conditions, it switches not only the RSC but also the full-bridge modules.

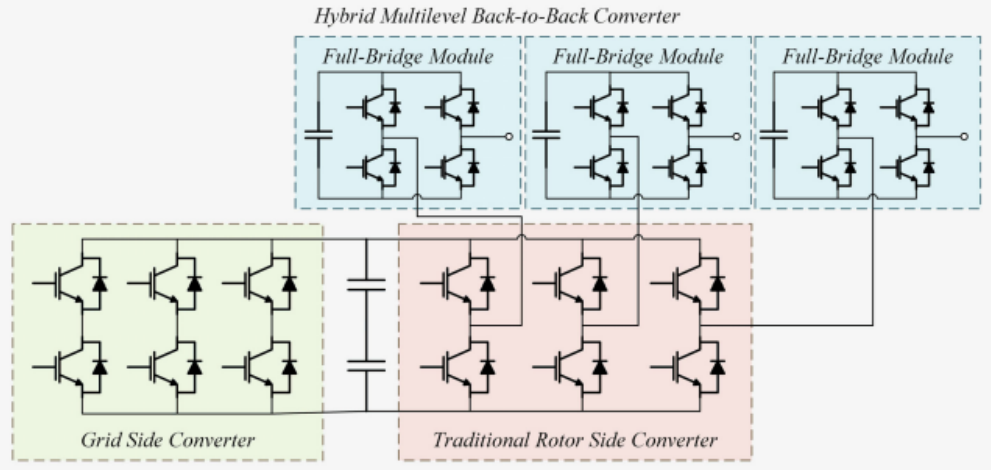

Figure 2.8 – Modified back-to-back converter topology (Amorim et al., 2021).

Since wind generating units are expected to support the grid during low voltages, and in situations where the DFIG may not consistently supply the required reactive power according to grid codes, the installation of Static VAR Compensators (SVCs) (Liu et al., 2020a, Liu et al., 2018) or Static Synchronous Compensators (STATCOMs) (Hossain et al., 2012, Tanaka et al., 2019, Yao et al., 2022, Zhang et al., 2021, Zhou et al., 2023) at the DFIG terminals becomes necessary. These compensators are employed to provide the required reactive power.

The comparison of the primary hardware RTFC strategies found in the literature is summarized in Table 2.1. In the table, "○" indicates that the RTFC technique leads to an improvement in the variable, "x" indicates that the RTFC solution may worsen the variable, and "-" indicates that the RTFC technique has no impact on the variable.

Table 2.1 – Comparison between the strategies with additional hardware from the point of view of the relevant variables of the DFIG-WT system.

RTFC technique	Active and Reactive Power Support	High DC-Link Voltage	High Rotor Voltage	High Rotor Current	High Stator Current
Crowbar	x	○	x	○	○
ESS	○	○	-	x	○
DC chopper	-	○	-	-	-
Modified DC chopper	-	○	-	○	-
SDR	○	○	○	○	-
SDBR	-	○	○	-	-
MSDBR	-	○	-	○	○
CSC	○	○	-	○	○
PGRS	○	○	-	-	-
FCL	-	-	○	-	○
SFCL	-	-	-	○	○
FCLSMES	○	○	-	○	○
HMC	○	○	○	○	-
STATCOM	○	○	-	-	x

2.3.2. Control techniques

In addition to implementing additional devices to enhance the LVRT capability of DFIG-WTs, the performance during transient periods can be improved through effective control strategies. This approach proves to be more economical as it eliminates the need for additional hardware.

Vector control, also known as field-oriented control (FOC), is a robust and versatile machine control method that can be employed to achieve high performance and efficiency across various applications, including DFIG-WT systems. The fundamental principle of vector control involves representing the stator currents of a three-phase AC machine as two orthogonal components, reflecting the torque-producing and flux-producing aspects of the stator current.

In the context of DFIG-based systems, vector control proves highly effective. It relies on proportional–integral (PI) controllers within the RSC, which are capable of regulating rotor speed, reactive power, and rotor current (Yang et al., 2011, Mohammadi et al., 2014).

Particle Swarm Optimization (PSO) was introduced in Ruiz-Cruz et al. (2012) to optimize the tuning of PI controller parameters, enhancing the overall control performance. However, the closed-loop structure of conventional vector control can lead to complex calculations and a sluggish dynamic response in DFIGs. In response to these challenges, a combined Vector and Direct Power Control (CVDPC) was proposed in Mohammadi et al. (2014). This innovative approach aims to achieve a faster dynamic response, reduce computation complexity, and simplify implementation in DFIGs.

Utilizing the mechanism where DC flux can be transformed into compensation current, Chen et al. (2011) introduced the Current Compensation (CC) control to enhance the LVRT capability of DFIG-based WECSs. As an effective RSC control method, this technique employs compensation current to counteract the DC flux induced by faults. Consequently, transient current and rotor voltage can be effectively limited. To complement the CC control, a crowbar circuit is incorporated into the DC-link. This crowbar circuit serves as a release channel for additional power, ensuring coordinated and effective control during fault conditions.

The optimal active current compensation controller plays a crucial role in enhancing the LVRT capability of DFIG-WTs. Leveraging the mechanism that judicious active current injection can substantially enhance the small-signal stability of DFIG-based systems. Thus, a novel optimal method for active and reactive current proportion was introduced in Liu et al. (2019).

In Hu et al. (2008), a coordinated control method, comprising a PI controller and resonant compensation, was implemented in DFIG-WTs to constrain torque and active power oscillations. This approach contributed to improving the dynamic performance of DFIG-WTs under unbalanced conditions. Subsequently, in Hu et al. (2012), a PI-Dual Frequency Resonant (DFR) controller, consisting of a PI regulator and dual-frequency resonant (DFR), was employed in DFIG-WTs. Through this coordinated control strategy, oscillations in the DC-link voltage could be limited, ensuring a constant active power output. Both the RSC and the GSC were controlled to facilitate smooth and optimized operation.

In Liang et al. (2010), a Feedforward Transient Control (FFTCC) scheme for the RSC is proposed. This control scheme incorporates additional feedforward transient compensation into a conventional current regulator. During a three-phase fault, these compensation terms align the output voltage of the RSC with the transient-induced voltage, minimizing transient rotor currents and reducing the occurrence of crowbar interruptions. Although the computational burden is higher compared to conventional controllers, the proposed scheme enhances the LVRT capability of DFIG wind turbines (WTs).

Lima et al. (2010) present an alternative control strategy designed to mitigate currents in the stator/rotor windings when the system experiences a voltage sag. This control strategy involves utilizing the measured stator currents as the set point for the current controller of the RSC during a voltage dip. The details and analysis of this strategy will be further explored and discussed in Chapter 3 of the present work.

Mendes et al. (2011) propose a Magnetizing Current Control (MCC) for DFIG during symmetrical voltage sags. This control strategy will be discussed in further detail in section 3.3.1 of the present work. Additionally, Zhou et al. (2014b) also employ a magnetizing current control approach, alternating it with vector control of the DFIG converters. However, under severe voltage sags, high currents in the rotor are still observed, suggesting the need for its application in conjunction with other strategies.

Zhu et al. (2016) demonstrate the utilization of a control system capable of emulating the insertion of inductance into the RSC during a voltage sag. This strategy seeks a compromise between the high currents needed in some methods and the high voltages required in others. However, the presented results indicate that, for severe sags,

the rotor current still reaches high values, and there is an inability to inject reactive power during the fault. In a subsequent study, Zhu et al. (2017) introduced improvements to the PI control for the negative- and natural-sequence components through feedforward control of the oscillating components control loops. This method is not meant for optimizing current limiting or converter protection but rather dampening the oscillations caused by traditional control strategies.

Conventional Proportional-Integral-Derivative (PID) controllers, designed based on linearized system models, tend to exhibit poor performance during severe grid faults. Consequently, several nonlinear control methods have been proposed to enhance the control effectiveness of DFIG WTs under large disturbances.

In Ozsoy et al. (2017), a proportional current control with a first-order low-pass filter disturbance observer (DOb) was proposed. This approach establishes an independent control of both positive- and negative-sequence current components under asymmetrical grid voltage conditions.

Another technique described in Kong et al. (2022) is the Model Predictive Control (MPC), which relies on an effective linearized technique, specifically the input–output feedback linearization method. The control law is derived from optimizing two targets, aiming to eliminate oscillations in either active or reactive power.

Rafiee et al. (2022) propose an Advanced Transient Voltage Control (A-TVC) solution to enhance the LVRT capability of the DFIG. This study evaluates the system under different sag levels, employing the mentioned strategy to improve transient voltage stability and reduce stator and rotor overcurrents.

In a similar vein, Hiremath and Moger (2022) introduce the Modified Super Twisting (MST) algorithm to enhance the LVRT capability of the system. This technique utilizes the second-order sliding mode (SOSM) approach to control the DFIG. While the results demonstrate efficiency, the study lacks a more in-depth analysis, particularly under more severe voltage sag conditions.

In Qin et al. (2017), Input-to-State Stability (ISS)-based control was implemented for Doubly Fed Induction Generator Wind Turbines (DFIG-WTs). ISS is a potent tool for analyzing the stability of nonlinear control systems. It is employed to demonstrate the stability of systems under various disturbances and inputs. ISS is particularly valuable for

designing controllers capable of maintaining system stability in the presence of disturbances (Nešić and Teel, 2004). Leveraging the mechanism where the existence of Input-to-State Stability (ISS) control Lyapunov functions can demonstrate the input-to-state stability of nonlinear systems, a decentralized ISS control law was proposed for the RSC to enhance the transient stability of WTs.

However, ISS-based controllers can only ensure inverse optimality, requiring a combination with other control techniques to further optimize the ISS control parameters. In Qin and Sun (2018), an effective RSC control scheme was proposed based on the State-Dependent Riccati Equation (SDRE) technique. This scheme involves reasonably designing state-dependent coefficient (SDC) matrices and weighting matrices to enhance control performance.

The implementation of the SDRE control method offers the advantages of simplified control and mitigation of the impact of grid voltage dips. Furthermore, the choice of SDC matrices influences control performance, and the additional flexibility in selecting non-unique SDC matrices enhances the flexibility of robust controller design (Qin et al., 2018).

Fuzzy control is a form of intelligent control that utilizes fuzzy logic for decision-making. It is particularly well-suited for controlling nonlinear and uncertain systems, such as DFIG-WTs. This robust and reliable control method has the potential to enhance the performance and reliability of DFIG-based wind turbines (Lu, 2018).

In the study conducted by Djeridane et al. (2018), two fuzzy logic controllers were incorporated into RSCs. One of these controllers was designed to regulate the direct current proportional to the generated reactive power, while the other was responsible for controlling the quadrature current proportional to the generated active power. The results from simulations and experiments indicated that the fuzzy logic controller exhibited a faster and more accurate response compared to PI controllers.

Shihabudheen et al. (2018) propose a neuro-fuzzy algorithm named the learning adaptive neuro-fuzzy inference system (ELANFIS) for controlling the RSC in DFIG-WT system. The controllers in this strategy are trained based on the performance of different PI controllers tuned for various operational conditions. Real-time simulations demonstrate a favorable response compared to conventional PI control. In both balanced

and unbalanced dips, the strategy successfully dampens oscillations in stator and rotor current, DC bus voltage, and active and reactive powers. However, it shows less efficiency in reducing the peak values that stator and rotor currents reach at the beginning of the sag.

In Ruiz-Cruz et al. (2018), a neural discrete-time inverse optimal controller (NNDTIOC) is introduced. This proposed scheme represents the first instance of utilizing optimal inverse control for trajectory tracking in a DFIG. Moreover, it offers robustness to unmodeled dynamics and parameter variations through an online-trained neural network.

A comparison among the main RTFC control strategies found in the literature is presented in Table 2.2. In the table, ○ indicates that the RTFC technique leads to an improvement in the variable, x indicates that the RTFC solution may worsen the variable, and - indicates that the RTFC technique has no impact on the variable. In the same table, the column representing implementation complexity necessitates a distinct classification method compared to the other columns. For this purpose, indicators such as low, medium, and high were employed to denote the implementation complexity.

Table 2.2 – Comparison among the control strategies from the point of view of the relevant variables of the DFIG-WT system.

RTFC technique	DC-link Voltage	Rotor Voltage	Rotor Current	Stator Current	Implementation Complexity
Vector control	-	-	-	-	Low
Feedforward control	-	x	○	○	Low
MCC	-	-	○	○	Low
CRTC		x	○	○	Low
FSCR		x	○	○	Low
PIR	-	x	○	○	Low
DOb	-	-	-	-	High
ATV-C	-	-	○	○	Medium
MST	○	-	-	-	High
ISS	○	○	○	○	High
SDRE	○	○	○	○	High
Fuzzy	○	-	○	○	Medium
ELANFIS	○	○	x	x	High
NNDTIOC	-	-	○	○	High

This section has highlighted various RTFC strategies from the literature, each with its own set of advantages and disadvantages. The simpler strategies based on control methods may not always achieve full supportability. On the other hand, more expensive and complex systems can compromise the main advantage of the DFIG, which is the cost-effectiveness of the converter. However, none of these strategies have delved into the investigation of the thermal stresses experienced by semiconductor devices. Therefore, this work aims to take a further step in understanding the supportability of DFIG, particularly by exploring the thermal stresses on semiconductor devices.

2.4. Chapter closure

The chapter delves deeper into both balanced and unbalanced voltage dips, providing a theoretical foundation for understanding this phenomenon. This is achieved through the presentation of equations that describe the behavior of DFIG voltage and currents during a sag. By assimilating this information, it becomes evident how crucial it is to implement protection devices and RTFC strategies, which are specifically designed to mitigate the disturbances caused by voltage sags.

In conclusion, the chapter provides a comprehensive compilation of the most extensively researched control strategies in the literature. These strategies are categorized into two classes: those that incorporate additional hardware and those that rely solely on control techniques. This comprehensive review reveals both gaps and limitations in the study of techniques aimed at bolstering the DFIG-WT system against voltage sags. Additionally, the chapter includes a comparative analysis of the mentioned RTFC strategies, shedding light on their respective impacts on the most critical variables within the DFIG-WT system.

Chapter 3. **MODELING OF A DFIG-BASED WECS**

3.1. Simulation model

A computational model representing the main electrical dynamics of the DFIG drive was implemented using simulation software PLECS, as can be seen in Figure 3.1.

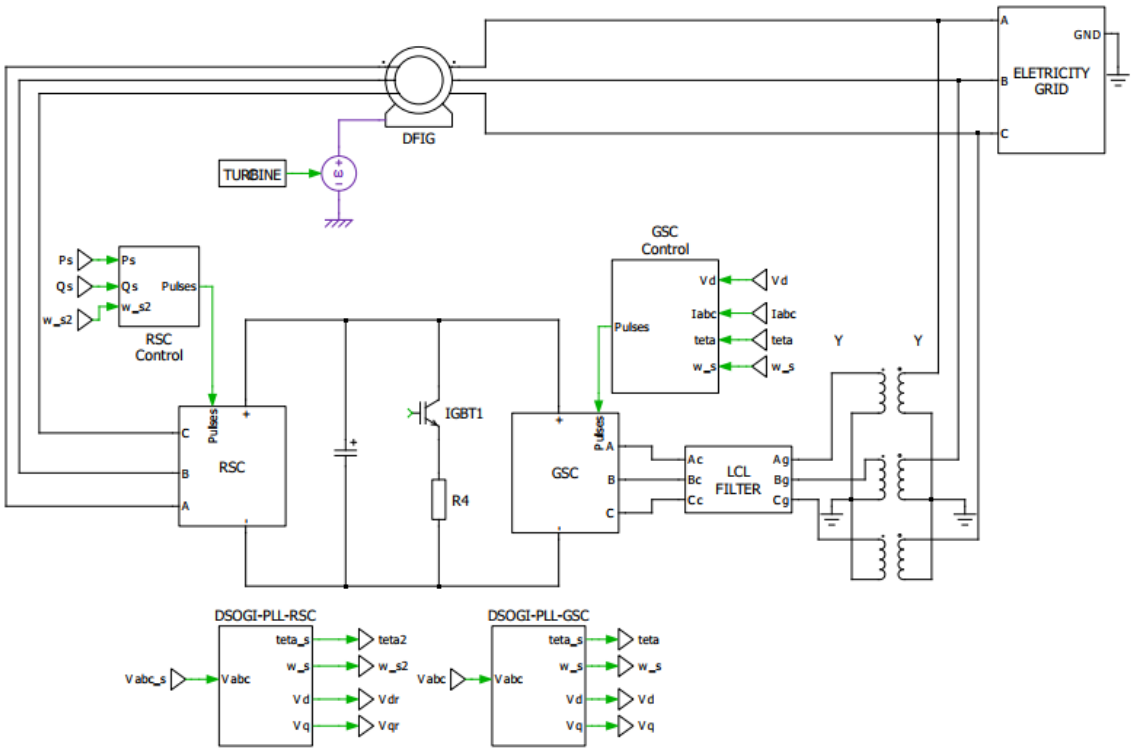

Figure 3.1 – Simulation model implemented in PLECS (Own authorship).

The parameters of the DFIG WECS used in this work are presented in Table 3.1 and Table 3.2. The modeling of the main components of the system is described in the next sections.

Table 3.1 – Parameters of the WECS.

Parameters	Value
GSC voltage	380 V
Grid frequency	60 Hz
Output rated power	2 MW
DC-link voltage	698 V
Switching frequency	3 kHz
DC-link capacitor	10 mF
Filter inductance converter side	240.67 µH
Filter inductance grid side	240.67 µH
Resistance of the converter side filter inductor	6,05 mΩ
Resistance of the grid side filter inductor	6,05 mΩ
Filter capacitance	9.2 mF

Table 3.2 – DFIG generator parameters.

Parameters	Value
Rated Power	1.6 MW
Stator voltage	690 V
Peak stator phase current amplitude	2000 A
Stator resistance	0.002381 Ω
Stator leakage inductance	0.07579 mH
Blocked rotor voltage	1380 V

Peak rotor phase current amplitude	1000 A
Rotor resistance	0.002381 Ω
Rotor leakage inductance	0.060481 mH
Magnetizing inductance	0.0023 H
Rotor/Stator Turns ratio	0.5
Inertia	59.4 kg/m²
Friction coefficient	0.007 Nms
Number of pole pairs	2

3.1.1. Grid

The grid is conceptualized as an ideal three-phase voltage source with infinite short-circuit capability, allowing simulation of both balanced and unbalanced voltage sags. As the focus is not on grid dynamics, the voltage sags are represented by instantaneous voltage drops, as illustrated in the examples shown in Figure 3.2.

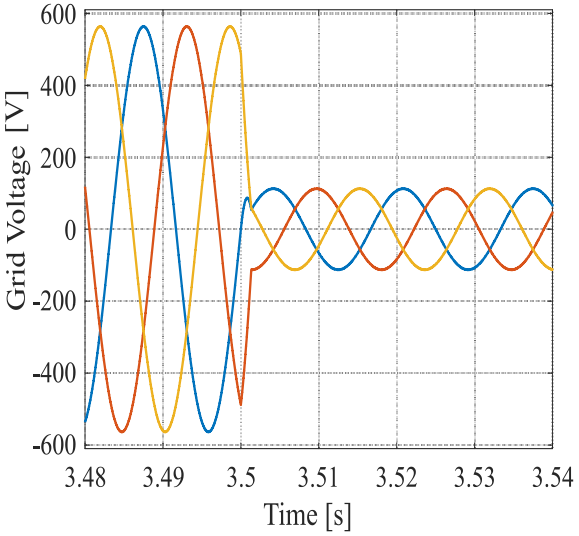

(a)

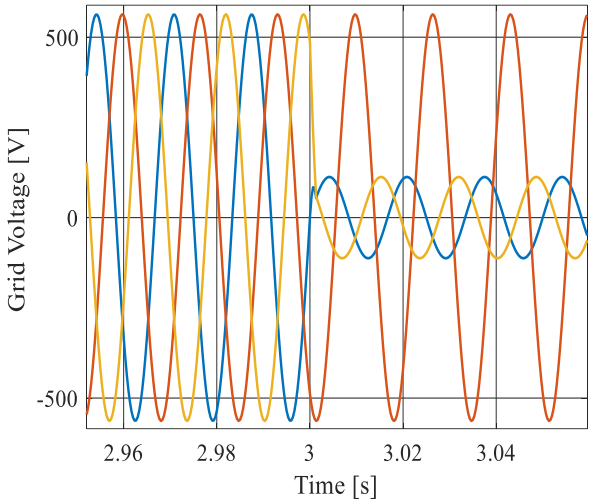

(b)

Figure 3.2 - Grid voltage after a 20% voltage sag: (a) balanced and (b) unbalanced.

3.1.2. LCL filter

To mitigate the grid harmonics introduced by the GSC, it is common to employ an inductor-capacitor-inductor (LCL) filter to connect the converter to the grid. The schematic diagram of the LCL filter is depicted in Figure 3.3, where:

- L_f and R_f represent the filter inductance and resistance on the converter side, respectively.
- L_N and R_N are the filter inductance and resistance on the grid side, which may also encompass the grid impedance.
- C_f is the filter capacitance.

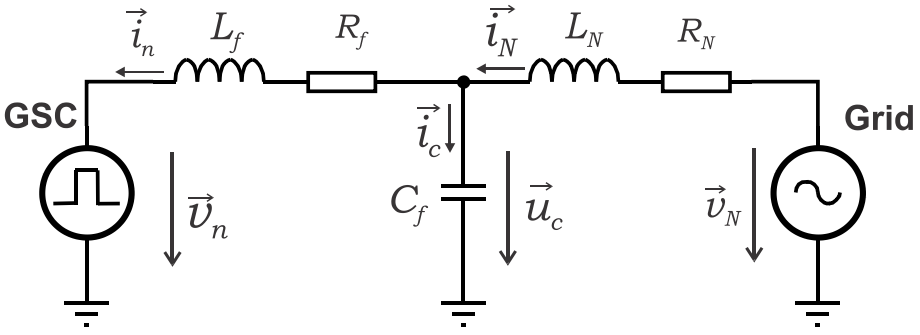

Figure 3.3 – LCL filter (Own authorship).

It is also common to use a resistor in series with the capacitor, although not explicitly shown in the circuit, to enhance filter damping. In addition, the capacitor voltage is approximately equal to the grid voltage. Employing vector notation and assuming a three-phase balanced system, the filter response at the grid frequency can be modeled as a simple RL circuit according to Equation (3.1):

$$\vec{v}_N = R_f \vec{i}_n + L_f \frac{d\vec{i}_n}{dt} + \vec{v}_n \tag{3.1}$$

where i_s is the filter current, v_N is the grid voltage, v_n is the voltage imposed by the GSC converter.

Rewriting the equation (3.1) in the synchronous reference frame, rotating with the grid voltage angular frequency (ω_N), yields:

$$\vec{v}_N = R_f \vec{i}_n + L_f \frac{d\vec{i}_n}{dt} + j\omega_N L_f \vec{i}_n + \vec{v}_n \tag{3.2}$$

Equation (3.2) can be divided in real (d) and imaginary (q) parts, then it is rewritten as:

$$v_{n_d} = -R_f i_{n_d} - L_f \frac{di_{n_d}}{dt} + v_{N_d} + \omega_N L_f i_{n_q} \tag{3.3}$$

$$v_{n_q} = -R_f i_{n_q} - L_f \frac{di_{n_q}}{dt} + v_{N_q} - \omega_N L_f i_{n_d} \tag{3.4}$$

For details on the filter design, refer to Liserre et al. (2005). The values of the filter components are determined based on the following limitations:

- The capacitance is restricted by the reactive power of the system, which must be kept below 5%;
- The inductance must be constrained to a value less than 0.1 pu to minimize voltage drop during operation;
- The resonance frequency of the filter must exceed 10 times the grid fundamental frequency and be below half of the inverter switching frequency to avoid resonance issues at low and high frequencies;

- The resistance value in series with the capacitor should be selected to smooth the filter's resonance peak without excessively increasing low-frequency losses and significantly reducing attenuation at high frequencies. A typical approach is to set the resistance value to half the value of the capacitor's impedance at the resonant frequency.

3.2. Classical control

3.2.1. GSC control

The classical GSC control strategy employs internal loops to control the grid currents, which are oriented in the angle of the grid voltage. This orientation allows for a decoupled control of active and reactive power (Pena et al., 1996). The direct-axis component (d) is responsible for active power, and an external controller for the quadrature-axis (q) current control loop regulates reactive power. External to the direct-axis current loop, the DC-link voltage control is implemented. Figure 3.4 provides a block diagram representation of the GSC control. The PI compensators are tuned using the pole allocation method.

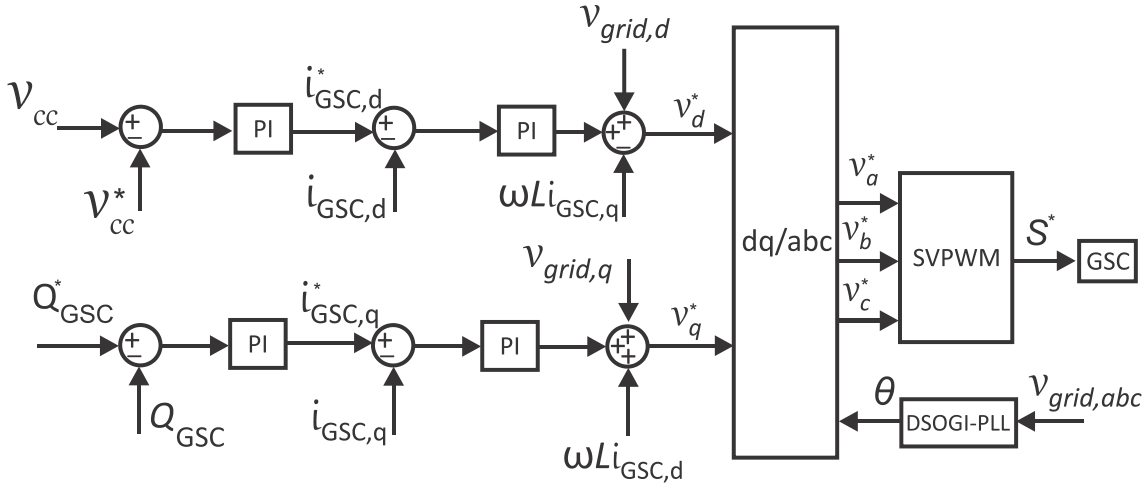

Figure 3.4 – Block diagram representation of the GSC control structure (Own authorship).

The main parts of the control structure shown in Figure 3.4 are detailed below.

3.2.1.1. SVPWM

Pulse width modulation (PWM) is a technique employed in switching static converters, where the conduction and blocking times for each semiconductor can be adjusted, while maintaining a constant switching period. A straightforward variant of this technique is sinusoidal pulse width modulation (SPWM), wherein the three-phase voltage to be synthesized by the converter is compared with a high-frequency triangular wave.

However, another variant employed in this work is vector modulation or space vector pulse width modulation (SVPWM). SVPWM optimizes semiconductor switching, enhancing its utilization factor and providing AC voltages with higher amplitudes for the same DC voltage (Buso and Mattavelli, 2015). In this work, SVPWM was implemented following the approach outlined in Hava et al. (1999). Although other types of modulation exist, such as discontinuous pulse width modulation (DPWM) or selected harmonic elimination pulse width modulation (SHEPWM), SVPWM was chosen because it is the most commonly used in existing works in the literature and also in the strategies analyzed and discussed in this text.

3.2.1.2. Phase-Locked Loop (PLL)

The Phase-Locked Loop (PLL) is utilized to estimate the angle of the grid voltage vector, enabling the referencing of currents used in the control to the synchronous reference frame. The block diagram of the PLL employed in this work is illustrated in Figure 3.5 (Rodriguez et al., 2006), representing a PLL based on the dual second-order generalized integrator (DSOGI). This PLL is similar to the classical one, but it incorporates a decoupling structure for the separation of positive and negative sequence components of the voltages. The reason for using this PLL is its capability to provide a fast and accurate response even during unbalanced conditions.

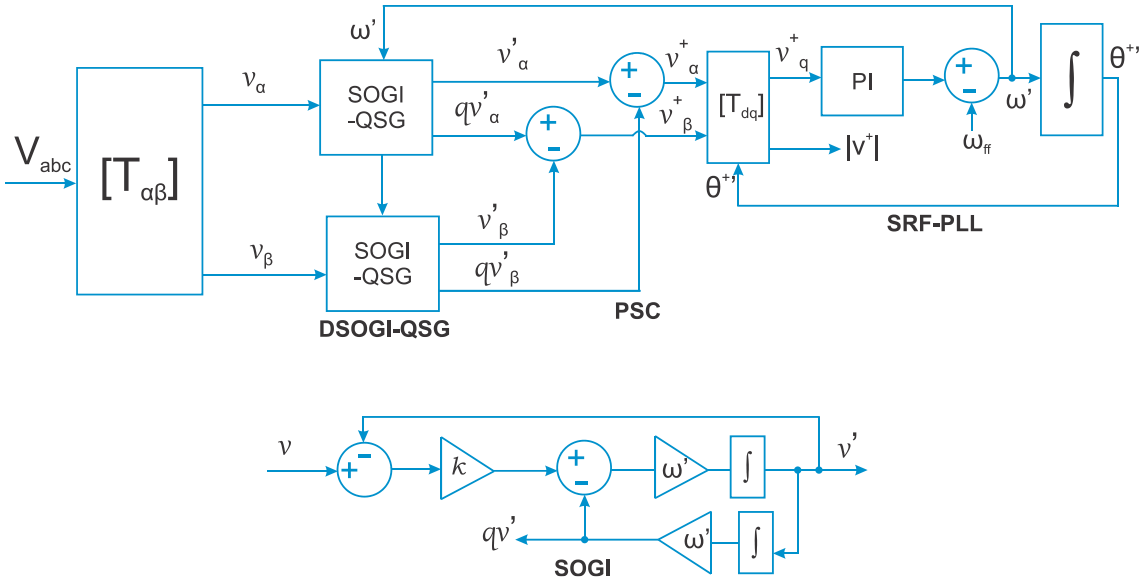

Figure 3.5 – Block diagram of DSOGI-PLL (Adapted from (Rodriguez et al., 2006)).

3.2.1.3. GSC current control

The GSC is connected to the grid through the LCL filter. For the sake of simplifying the design of the control loops, this filter is considered only as the sum of the inductances. Equations (3.5) and (3.6) describe this system in a synchronous reference frame.

$$v_d = -R_f i_{GSC,d} - L_f \frac{di_{GSC,d}}{dt} + v_{grid,d} + \omega L_f i_{GSC,q} \tag{3.5}$$

$$v_q = -R_f i_{GSC,q} - L_f \frac{di_{GSC,q}}{dt} - \omega L_f i_{GSC,d} \tag{3.6}$$

In these equations, the voltages *vd* and *vq* represent the direct axis and quadrature components synthesized by the converter, *Rf* is the filter resistance, L_f is the filter inductance, i_{GSC} is the GSC current, and v_{grid} is the grid voltage, which has only the direct axis component owing to the adopted orientation.

It is noted that there are coupling terms between the axes in Equation (3.5) and (3.6). These terms are considered disturbances in the control loop and are compensated by feedforward controllers, as described in Equations (3.7) and (3.8).

$$v_{comp,d} = v_{grid,d} + \omega L_f i_{GSC,q} \tag{3.7}$$

$$v_{comp,q} = -\omega L_f i_{GSC,d} \tag{3.8}$$

Applying the Laplace transform in equations (3.5) and (3.6), and considering that the cross-coupling terms are totally compensated, it is possible to obtain the transfer function that describes the currents dynamics:

$$\frac{i_{GSC,d}(s)}{v_d(s)} = \frac{i_{GSC,q}(s)}{v_q(s)} = \frac{1}{sL_f + R_f} \tag{3.9}$$

In this transfer function, the subscripts *d* and *q* are omitted, since both components have the same dynamics. The control loops $i_{GSC,d}(s)$ and $i_{GSC,q}(s)$ can be seen in Figure 3.6. The converter dynamics is represented by $G(s)$. This dynamic behavior is neglected when designing the controllers because the unity-gain crossover frequency of the current loops is much lower than the converter switching frequency.

The open-loop transfer function of Figure 3.6 can be easily obtained, resulting in:

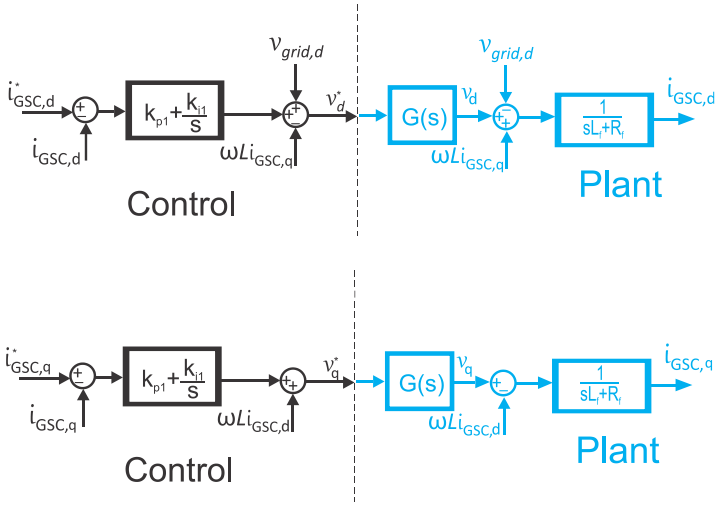

Figure 3.6 – GSC current control loop (Own authorship).

$$\frac{i_{GSC,d}(s)}{i^*_{GSC,d}(s)} = \frac{i_{GSC,q}(s)}{i^*_{GSC,q}(s)} = \frac{s + k_{i1}/k_{p1}}{s + R_f/L_f}\frac{k_{p1}}{sL_f} \tag{3.10}$$

Equation (3.10) has a pole near the origin given by $-R_f/L_f$. Thus, canceling the pole with the zero of the function yields:

$$\frac{k_{i1}}{k_{p1}} = \frac{R_f}{L_f} \tag{3.11}$$

In addition, the closed-loop transfer function $H(s)$ is:

$$H(s) = \frac{i_{GSC,d}(s)}{i^*_{GSC,d}(s)} = \frac{i_{GSC,q}(s)}{i^*_{GSC,q}(s)} = \frac{1}{sL_f / k_{p1} + 1} = \frac{1}{s\tau_1 + 1} \tag{3.12}$$

The cut-off frequency is chosen as $f_1 = (1/2\pi\tau_1) = f_{sw}/10$, i.e., one decade below than the switching frequency of the GSC such that the dynamics power electronic system can be neglected in the loop. So, from Equations (3.11) and (3.12), the controller gains are defined as:

$$\begin{cases} k_{p1} = 2\pi f_1 L_f \\ k_{i1} = 2\pi f_1 R_f \end{cases} \tag{3.13}$$

3.2.1.4. DC-link voltage control

The DC-link voltage control is achieved by balancing the active power flowing through the GSC and the RSC. The schematic diagram of the DC-link is shown in Figure 3.7. Analyzing this circuit, equation (3.14) can be written.

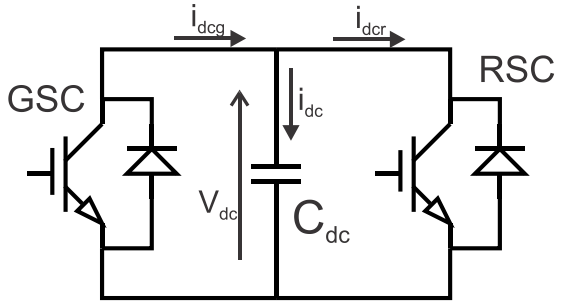

Figure 3.7 – Schematic diagram of the DC-link (Own authorship).

$$C_{dc}\frac{dv_{dc}}{dt} = i_{dcr} - i_{dcg} \tag{3.14}$$

where C_{dc} is the DC-link capacitance, i_{dcr} is the DC-link current coming from the RSC, and i_{dcg} is the DC-link current of the GSC.

A second relation can be written. It concerns the equality of active power in the *dq* reference frame on the AC side of the GSC with the same active power of the DC side. Neglecting the losses in the converter yields:

$$P_{GSC} = \frac{3}{2}\left(v_{grid,d} i_{GSC,d} + v_{grid,q} i_{GSC,q}\right) = i_{dcg} v_{dc} \tag{3.15}$$

Owing to the alignment of the axis the grid voltage, $v_{grid,q} = 0$. Thus, equation (3.15) can be rewritten as:

$$H_{vdc}(s) = \frac{i_{dcg}(s)}{i_{GSC,d}(s)} = \frac{3v_{grid,d}}{2v_{dc}} \tag{3.16}$$

Figure 3.8 shows the DC-link control loop, in which current i_{dcr} can be compensated or considered a disturbance. The internal GSC current loop is represented by $H(s)$. The outer loop controllers are designed to have a much lower unit-gain crossover frequency than inner loops. Thus, $H(s)$ is assumed as a unitary gain for the control design.

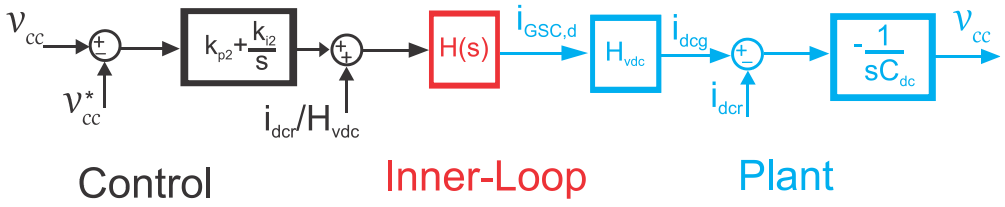

Figure 3.8 – DC-link control loop (Own authorship).

The closed-loop transfer function of the system shown in Figure 3.8 disregarding the internal loop can be written as:

$$\frac{v_{dc}(s)}{v_{dc}^{*}(s)} = \frac{sk_{p2} + k_{i2}}{-s^2 C_{dc} / H_{vdc}(s) + sk_{p2} + k_{i2}} \tag{3.17}$$

By allocating the two poles at $f_2 = f_1/10$ and $f_3 = f_2/10$, the following gains for the controller are obtained:

$$\begin{cases} k_{p2} = -\dfrac{2\pi(f_2 + f_3)C_{dc}}{H_{vdc}} \\ k_{i2} = -\dfrac{4\pi^2 f_2 f_3 C_{dc}}{H_{vdc}} \end{cases} \tag{3.18}$$

3.2.1.5. GSC reactive power control

The reactive power has several purposes such as minimizing losses, control the grid power factor and ensuring voltage support.

With the grid voltage angle orientation, the reactive power control loop is external to the loop controlling the quadrature current. The reactive power is not directly measured, but calculated through Equation (3.19):

$$Q_{GSC} = -\frac{3}{2} v_{grid,d} i_{GSC,q} \tag{3.19}$$

Generally, the calculated power is noisy, because it uses the multiplication between the measured currents and voltages that are subjected to electromagnetic interference. It is common the use of a filter in the power which is considered a first order one in the present work. Therefore, the reactive power control loop is depicted in Figure 3.9.

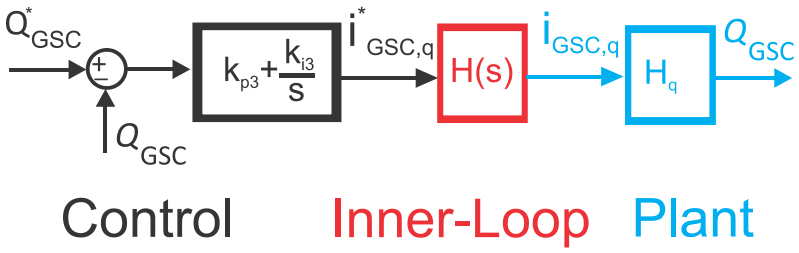

Figure 3.9 – GSC reactive power control loop (Own authorship).

Thus, the closed-loop transfer function can be seen in Equation (3.20).

$$\begin{cases} \dfrac{Q_{GSC}}{Q_{GSC}^{*}} = \dfrac{sk_{p3}/k_{i3}+1}{s\left(k_{p3}H_q+1\right)/\left(k_{i3}H_q\right)+1} = \dfrac{s\tau_2+1}{s\tau_3+1} \\ H_q = -\dfrac{3}{2}v_{grid,d} \end{cases} \tag{3.20}$$

Neglecting $i_{gsc,q}$ in the inner loop dynamics and adopting a zero of the frequency at $f_2 = 1/2\pi\tau_2 \approx f_1/10$ and $f_3 = 1/2\pi\tau_3 \approx f_2/10$, it is assumed that the controller gains will be:

$$\begin{cases} k_{p3} = \dfrac{2\pi f_3}{2\pi(f_2 - f_3)H_q} \\ k_{i3} = 2\pi f_2 k_{p3} \end{cases} \tag{3.21}$$

3.2.2. RSC control

The GSC controls maintain a constant DC-link voltage, allowing the generator control through the RSC, which regulates the rotor currents.

Using an orientation in the angle of stator voltage (grid voltage), the stator active and reactive powers are calculated by equations (3.22) and (3.23), respectively (Mendes, 2013):

$$P_s = \frac{3}{2}v_{s_d}i_{s_d} = -\frac{3}{2}\frac{L_m}{L_s}v_{s_d}i_{r_d} \tag{3.22}$$

$$Q_s = -\frac{3}{2}v_{s_d}i_{s_q} = \frac{3}{2}\frac{v_{s_d}^2}{\omega_s L_s} + \frac{3}{2}\frac{L_m}{L_s}v_{s_d}i_{r_q} \tag{3.23}$$

The stator active power depends on the direct axis rotor current, and the reactive power depends on the quadrature axis rotor current. Therefore, decoupled rotor currents internal control loops with external active and reactive power control loops are used in the RSC, as depicted in Figure 3.10.

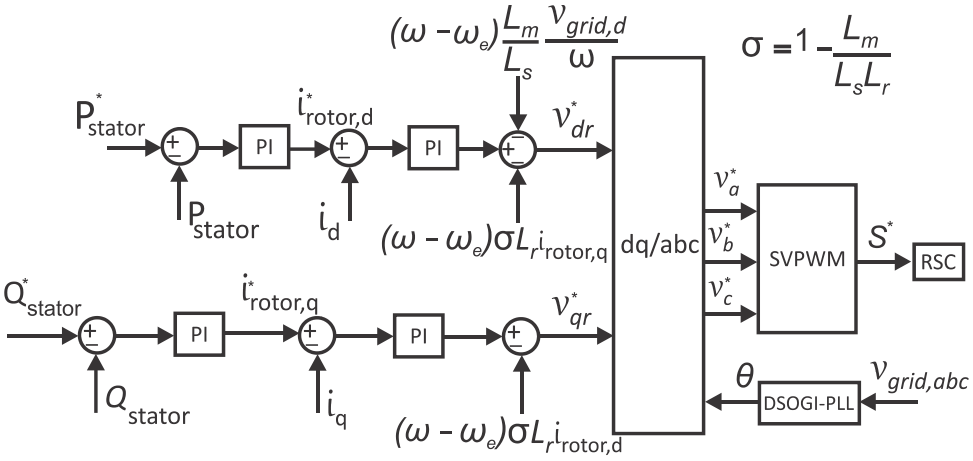

Figure 3.10 – Block diagram of the RSC control structure (Own authorship).

Before starting the presentation of each RSC control loop, in the following subsection the orientation of the generator variables is analyzed.

3.2.2.1. Orientation of DFIG variables

Similar to the GSC control, it is desirable to use the rotor currents' orientation that permits the decoupling control of active and reactive power. In electrical machines, it is common to use the stator, the rotor, or the mutual fluxes for the control orientation (Hopfensperger et al., 2000). For the DFIG, normally the so-called virtual grid flux is used for the rotor currents' orientation (Petersson et al., 2004), (Hopfensperger et al., 2000).

In steady state, the grid virtual flux $\left(\vec{\psi}_{s_v}\right)$, or similarly the stator virtual flux, is calculated from Equation (2.1) neglecting the voltage drop in the stator resistance, since this resistance is generally small:

$$\vec{\psi}_{s_v} \qquad j\omega_s \tag{3.24}$$

Equation (3.24) shows that the virtual flux has the same frequency of the grid $(\omega_s = \omega)$ and it is 90º lagging the grid voltage. Figure 3.11 depicts the vector diagrams for the orientation of the direct axis in the direction of the virtual flux and stator flux. One can notice that using the virtual flux orientation, the angle difference compared with the use of the stator flux is small if the voltage drop in the stator resistance is relatively small.

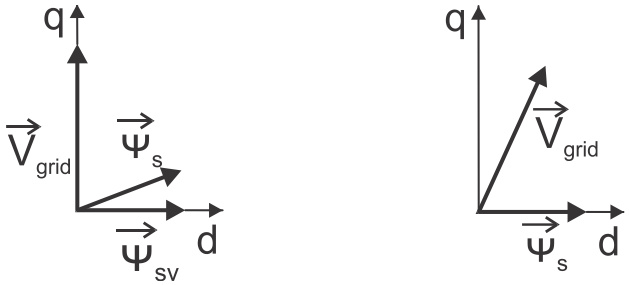

Figure 3.11 – Vector diagram of the grid voltage and stator flux: (a) virtual flux orientation and (b) stator flux orientation (Own authorship).

Instead of using the virtual flux, in this work the stator currents and voltages are orientated using angle of the stator (grid) voltage (transformation angle θ), as depicted in the vector diagram of Figure 3.12. With this orientation, the direct stator current controls the active stator power whereas the quadrature stator current is responsible for the reactive power, similar to the GSC.

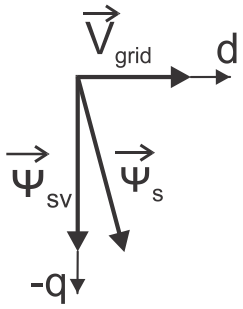

Figure 3.12 – Stator flux orientation (Own authorship).

3.2.2.2. RSC current control

Using the stator voltage orientation, equation (2.2) is divided in direct (real) and quadrature (imaginary) components and is rewritten as:

$$v_{rd} = R_r i_{rd} + \sigma L_r \frac{di_{rd}}{dt} - \omega_r \frac{L_m}{L_s} \psi_{sq} - \omega_r \sigma L_r i_{rq} \tag{3.25}$$

$$v_{rq} = R_r i_{rq} + \sigma L_r \frac{di_{rq}}{dt} + \omega_r \sigma L_r i_{rd} \tag{3.26}$$

where $\sigma = 1 - \frac{L_m^2}{L_s L_r}$ is the machine leakage coefficient. The last terms in these equations are the cross-coupling between direct and quadrature axes and are described in Equations (3.27) and (3.28).

$$v_{rcomp,d} = -\omega_r \frac{L_m}{L_s} \psi_{sq} - \omega_r \sigma L_r i_{rq} \tag{3.27}$$

$$v_{rcomp,q} = \omega_r \sigma L_r i_{rd} \tag{3.28}$$

These terms act like perturbations for the current control and, once it is possible to estimate them, feedforward compensators are used to improve the disturbance rejection.

Applying the Laplace transform and neglecting the perturbation terms, the following transfer function can be written:

$$\frac{i_{rd}(s)}{v_{rd}(s)} = \frac{i_{rq}(s)}{v_{rq}(s)} = \frac{1}{s\sigma L + R_r} \tag{3.29}$$

Figure 3.13 provides the visualization of the $i_{rd}(s)$ and $i_{rq}(s)$ control loops, where $G(s)$ represents the converter dynamics. This dynamic behavior is neglected when designing the controllers because the unity-gain crossover frequency of the current loops is much lower than the converter switching frequency.

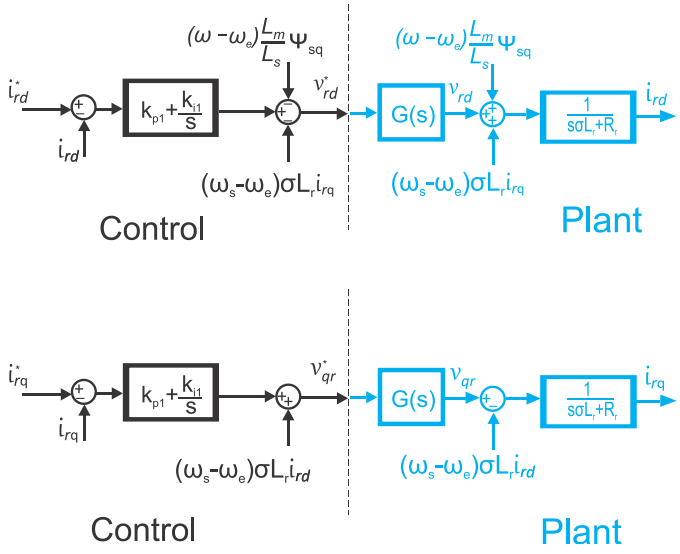

Figure 3.13 – RSC current control loops (Own authorship).

From Figure 3.13, the open-loop transfer function can be expressed as:

$$\frac{i_{rd}(s)}{i_{rd}^{*}(s)} = \frac{i_{rq}(s)}{i_{rq}^{*}(s)} = \frac{s + k_{i1}/k_{p1}}{s + R_r/\sigma L_r} \frac{k_{p1}}{s\sigma L_r} \tag{3.30}$$

As observed, there is a pole close to zero, due to the low value that R_r generally has in relation to (σL_r), mainly in machines of higher power. Therefore, this pole can be canceled by the zero, resulting in:

$$\frac{k_{i1}}{k_{p1}} = \frac{R_r}{\sigma L_r} \tag{3.31}$$

In addition, the closed-loop transfer function is:

$$H_{rsc}(s) = \frac{i_{rd}(s)}{i_{rd}^{*}(s)} = \frac{1}{1 + s\sigma L_r/k_{p1}} = \frac{1}{1 + s\tau_i} \tag{3.32},$$

and as notice that, it resembles a first-order function with the time constant τ_i. Allocating the loop cutoff frequency to $f_1 = f_{sw}/10$, where f_{sw} is the converter switching frequency. Thus, through Equation (3.33), the controllers' gains will be:

$$\begin{cases} k_{p1} = 2\pi f_1 \sigma L_r \\ k_{i1} = 2\pi f_1 \sigma R_r \end{cases} \tag{3.33}$$

3.2.2.3. Stator active and reactive power control

Equations (3.22) and (3.23) show the calculation of the active and reactive stator power using the stator voltage orientation. Rewriting Equations (3.22) and (3.23) results in Equations (3.34) and (3.35), respectively.

$$\frac{P_s}{i_{rd}} = -\frac{3}{2}\frac{L_m}{L_s} v_{sd} \tag{3.34}$$

$$\frac{Q_s}{i_{rq}} = \frac{3}{2}\frac{L_m}{L_s} v_{sd} \tag{3.35}$$

Figure 3.14 and Figure 3.15 depict the control loop block diagram, where $H_{rsc}(s)$ is the internal RSC current loop. The outer loop controllers are designed to have a much

lower unity-gain crossover frequency than inner loops. Thus, $H_{rsc}(s)$ will correspond to a unitary gain.

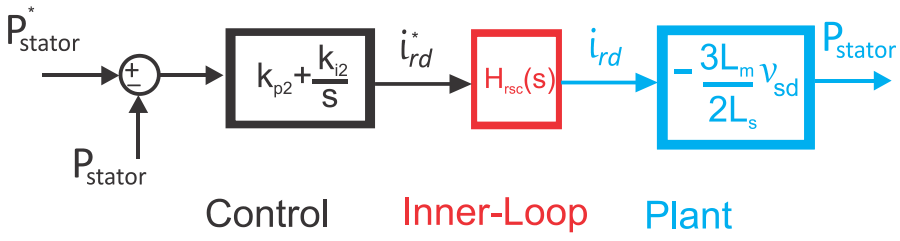

Figure 3.14 – Stator active power control loop (Own authorship).

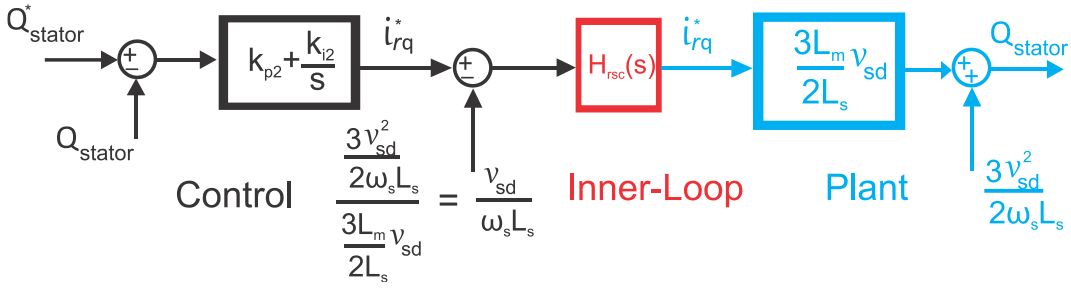

Figure 3.15 – Stator reactive power control loop (Own authorship).

The closed-loop transfer functions are represented according to Equation (3.36):

$$\begin{cases} \dfrac{P_s(s)}{i_{rd}(s)} = \dfrac{Q_s(s)}{i_{rq}(s)} = \dfrac{sk_{p2}/k_{i2}+1}{s\left(k_{p2}H_1+1\right)/k_{i2}H_1(s)+1} = \dfrac{s\tau_2+1}{s\tau_3+1} \\ H_1(s) = \pm\dfrac{3}{2}\dfrac{L_m}{L_s}v_{sd} \ ; \text{negative signal for } \dfrac{P_s}{i_{rd}} \end{cases} \tag{3.36}$$

Allocating the frequencies $2\pi f_2 = 1/\tau_2$ and $2\pi f_3 = 1/\tau_3$ approximately at $f_1/10$ and $f_1/100$, respectively, the following values are obtained for the controllers' gains:

$$\begin{cases} k_{p2} = \dfrac{f_3}{(f_2 - f_3)H_1} \\ k_{i2} = 2\pi f_2 k_{p2} \end{cases} \tag{3.37}$$

It is observed that allocating the pole frequency ten times smaller than the frequency of the zero, the transfer function in Equation (3.36) becomes a low-pass filter, with a cut-off frequency about a hundred times lower than that of the inner loops. Also, to determine $H_1(s)$, v_{sd} was used as the peak of the nominal phase voltage of the stator.

3.2.3. Controller discretization

Previously, it was shown how to adjusting the controllers using the continuous time transfer functions. However, the implementation of the controllers is generally discrete. Therefore, all signals measured to carry out the control of the converters were sampled at a frequency equal to twice the switching frequency. The advantage of this sampling is that it works as a filter for ripples of converter AC currents.

The samples are taken using a zero-order holder in which the discrete signals are stepped approximations of the continuous time signals. Further details on signal sampling, zero-order holder, and higher order holders can be found in Oppenheim and Willsky (2010).

The discretization of the controllers was done using the bilinear transform, also called Tustin or trapezoidal transform, as detailed in Equation (3.38).

$$s = \frac{2}{T_{sample}} \frac{z-1}{z+1} \tag{3.38}$$

where T_{sample} is the sampling time.

The main advantage of this discretization method, in relation to the Euler (forward Euler) and differential (backward Euler) methods, is that a stable continuous transfer function remains stable when discretized. This is because the left half-plane in the *s* domain (Laplace transform) corresponds to a circle of unity radius in the z domain (Z transform).

It is worth mentioning that the gains calculated for the continuous domain and shown in Table 3.3 were used for discretized controllers since due to the high frequency used in the sampling, the continuous response approximates the discrete signals.

Table 3.3 – Control gains of the grid-side converter and rotor-side converter.

Control Loop	Proportional Gain	Integral Gain
GSC currents	0.907 Ω	22.80 Ω/s
DC-link voltage	3.11 S	53.33 S/s
RSC currents	1.10 Ω	30.28 Ω/s
Stator power	0.00192 1/V	0.03620 1/(V.s)

3.3. RTFC control strategies

In Section 2.3, several strategies aimed at improving the withstand capability of voltage sags were highlighted. However, control-focused strategies were chosen for analysis and implementation. The strategy mentioned below was chosen because it was developed by researchers from LCCE at UFMG. The other studied strategies were selected for their similarity in operating principles, allowing for a more reliable comparison.

3.3.1. Magnetizing current control (MCC)

The objective of this strategy is to control the magnetizing current to enhance the damping of stator flux linkage oscillations, thereby reducing torque and power pulsations during voltage sags.

Utilizing the synchronous reference frame with orientation based on the grid voltage angle, the magnetizing current can be computed as follows:

$$i_m = -\left(i_{rq} + i_{sq}\right) \tag{3.39}$$

Equation (3.39) indicates that the magnetizing current is determined by the quadrature axis of the stator and rotor currents (Mendes, 2013). As the RSC governs the rotor currents, it is evident that the magnetizing current can be altered through the manipulation of the quadrature rotor current. Its magnitude can be approximated by:

$$i_m^* \approx \frac{\psi_{sq}}{L_m} \approx -\frac{v_{sd}}{L_m \omega_s} \tag{3.40}$$

The aim of this strategy is to manage the oscillations of the magnetizing current induced by the stator flux's natural component. The primary objective is to control the oscillatory (natural) part of the current, which, in the synchronous reference frame, manifests as an oscillation at the grid frequency. Thus, this oscillating component can be isolated from the total magnetizing current by utilizing a bandpass filter tuned to the stator electrical frequency, as described by the transfer function in Equation (3.41):

$$G(s) = \frac{\omega_s s}{s^2 + \omega_s s + \omega_s^2} \tag{3.41}$$

where ω_s is the stator angular frequency.

This filter is crucial because it removes high-frequency harmonics and noise, and eliminates the DC component. Additionally, the reference for the magnetizing current control can be set to zero, as only the oscillatory part is controlled. The block diagram corresponding to this strategy is shown in Figure 3.16.

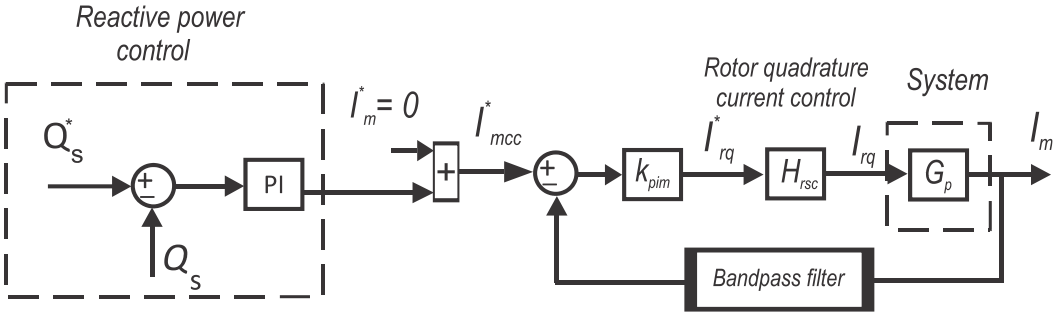

Figure 3.16 – Magnetizing current control block diagram (Own authorship).

In this figure I_m^* is the reference of the MCC, kept in 0, I_{mcc} is MCC current, I_m is the magnetizing current, k_{pim} is the proportional gain of the MCC, $H_{rsc}(s)$ is the rotor quadrature current control inner loop and $G_p(s)$ is the system plant represented as in Figure 3.13.

The control operates in cascade with the reactive power control, allowing independent control of reactive power during a sag. With this feedback structure, there is no need to detect the voltage sag and adopt a different control strategy during the dip, as the magnetizing control is always active.

The effects induced on the rotor currents and voltages by the strategy, along with a comprehensive mathematical model of the MCC, are analyzed and described in accordance with Mendes (2013).

Decomposing the machine equations corresponding to (2.1) and (2.2) into real (d-axis) and imaginary (q-axis) components and applying the Laplace transform while omitting the dependency of *s* in the variables yields:

$$V_{sd} = R_s I_{sd} + s\psi_{sd} - \omega_s \psi_{sq} \tag{3.42}$$

$$V_{sq} = R_s I_{sq} + s\psi_{sq} + \omega_s \psi_{sd} \tag{3.43}$$

$$V_{rd} = R_r I_{rd} + s\psi_{rd} - \omega_r \psi_{rq} \tag{3.44}$$

$$V_{rq} = R_r I_{rq} + s\psi_{rq} + \omega_r \psi_{rd} \tag{3.45}$$

$$\psi_{sd} = L_s I_{sd} + L_m I_{rd} \tag{3.46}$$

$$\psi_{sq} = L_s I_{sq} + L_m I_{rq} \tag{3.47}$$

$$\psi_{rd} = L_r I_{rd} + L_m I_{sd} \tag{3.48}$$

$$\psi_{rq} = L_r I_{rq} + L_m I_{sq} \tag{3.49}$$

From Equations (3.46) and (3.47), the stator currents can be expressed as:

$$I_{sd} = \frac{\psi_{sd} - L_m I_{rd}}{L_s} \tag{3.50}$$

$$I_{sq} = \frac{\psi_{sq} - L_m I_{rq}}{L_s} \tag{3.51}$$

Substituting (3.39) in (3.47) yields:

$$I_{sq} = \frac{\psi_{sq} - L_m I_m}{L_s - L_m} \tag{3.52}$$

Substituting (3.52) in (3.43) gives:

$$\psi_{sq} = \frac{\dfrac{R_s L_m}{L_s - L_m}}{s + \dfrac{R_s}{L_s - L_m}} I_m - \frac{\omega_s}{s + \dfrac{R_s}{L_s - L_m}} \psi_{sd}, \tag{3.53}$$

Substituting (3.53) and (3.50) in (3.42), one can write:

$$\psi_{sd} = \frac{\left(s + \dfrac{R_s}{L_s - L_m}\right)}{\left[s^2 + \left(\dfrac{R_s}{L_s - L_m} + \dfrac{R_s}{L_s}\right)s + \dfrac{R_s^2}{L_s\left(L_s - L_m\right)} + \omega_s^2\right]} V_{sd} + \frac{\omega_s L_m \dfrac{R_s}{L_s - L_m}}{\left[s^2 + \left(\dfrac{R_s}{L_s - L_m} + \dfrac{R_s}{L_s}\right)s + \dfrac{R_s^2}{L_s\left(L_s - L_m\right)} + \omega_s^2\right]} I_m +$$

$$+ \frac{L_m \dfrac{R_s}{L_s}\left(s + \dfrac{R_s}{L_s - L_m}\right)}{\left[s^2 + \left(\dfrac{R_s}{L_s - L_m} + \dfrac{R_s}{L_s}\right)s + \dfrac{R_s^2}{L_s\left(L_s - L_m\right)} + \omega_s^2\right]} I_{rd} \tag{3.54}$$

It is possible to neglect the term $\dfrac{R_s^2}{L_s\left(L_s - L_m\right)}$, much smaller than ω^2_s, and considering $\tau_{\sigma s} = \dfrac{L_s - L_m}{R_s} = \dfrac{L_{\sigma s}}{R_s}$, since $L_s = L_{\sigma s} + L_m$ and $L_{\sigma s}$ is the stator linkage inductance. The last term, which is dependent on I_{rd}, can also be neglected because the transfer function gain is smaller when compared with the other two terms. From these assumptions, one can write the following equation:

$$\psi_{sd}(s) = \frac{\left(s + \dfrac{1}{\tau_{\sigma s}}\right)}{\left[s^2 + \left(\dfrac{1}{\tau_s} + \dfrac{1}{\tau_{\sigma s}}\right)s + \omega_s^2\right]} V_{sd}(s) + \frac{\dfrac{\omega_s L_m}{\tau_{\sigma s}}}{\left[s^2 + \left(\dfrac{1}{\tau_s} + \dfrac{1}{\tau_{\sigma s}}\right)s + \omega_s^2\right]} I_m(s) \tag{3.55}$$

Similarly, it is possible to derive the *q*-axis component of the stator flux linkage as follows:

$$\psi_{sd}(s) = \frac{-\omega_s}{\left[s^2 + \left(\dfrac{1}{\tau_s} + \dfrac{1}{\tau_{\sigma s}}\right)s + \omega_s^2\right]} V_{sd}(s) + \frac{\dfrac{L_m}{\tau_{\sigma s}}\left(s + \dfrac{1}{\tau_{\sigma s}}\right)}{\left[s^2 + \left(\dfrac{1}{\tau_s} + \dfrac{1}{\tau_{\sigma s}}\right)s + \omega_s^2\right]} I_m(s) \tag{3.56}$$

Equations (3.55) and (3.56) show how the magnetizing current influences the stator flux linkage, however the objective of the development is to evaluated the flux behavior when this current is controlled.

As the control acts only on the current oscillations, only a proportional controller (k_{pim}) is necessary, as zero steady-state error is not of interest. For the sake of simplicity in the analysis, the following simplifications are considered:

- The reactive power control is neglected because, generally, it has a narrow bandwidth, and during the transient, the controller output varies slowly;
- Only the natural (oscillatory) flux response is analyzed, since the control reference is zero. This assumption is represented by the superscript "*n*" in the flux variables;
- The rotor current control (internal loop) is much faster than the magnetizing current control and has no limitations. Therefore, the rotor current reference generated by the external loop can be reached immediately.

Assuming these simplifications, the rotor current can be written as:

$$I_{rq} = -\frac{k_{pim} I_{sq}}{1 + k_{pim}} \tag{3.57}$$

Substituting (3.57) in (3.47) yields:

$$I_{sq} = \frac{\psi_{sq}^{n} \left(1 + k_{pim}\right)}{k_{pim} L_s + L_s - k_{pim} L_m}, \tag{3.58}$$

Substituting (3.58) in (3.43) gives:

$$\psi_{sq}^{n} = \frac{-\omega_s \psi_{sd}^{n}}{s + \dfrac{R_s \left(1 + k_{pim}\right)}{k_{pim} L_s + L_s - k_{pim} L_m}} \tag{3.59}$$

Using (3.59) and (3.50) in (3.42) results in:

$$\psi_{sd}^{n}=\frac{\left[s+\frac{R_s\left(1+k_{pim}\right)}{k_{pim}L_s+L_s-k_{pim}L_m}\right]V_{sd}+\left[L_m\frac{R_s}{L_s}\left(s+\frac{R_s\left(1+k_{pim}\right)}{k_{pim}L_s+L_s-k_{pim}L_m}\right)\right]I_{rd}}{\left[s^2+\left(\frac{R_s}{L_s}+\frac{R_s\left(1+k_{pim}\right)}{k_{pim}L_s+L_s-k_{pim}L_m}\right)s+\frac{R^2{}_s\left(1+k_{pim}\right)}{L_s\left(k_{pim}L_s+L_s-k_{pim}L_m\right)}+\omega_s^2\right]} \quad (3.60)$$

The term $\left[R_s^2\left(1+k_{pim}\right)\right]/\left[L_s\left(k_{pim}L_s+L_s-k_{pim}L_m\right)\right]$ is much smaller than $\omega^2{}_s$ and can be neglected. The second term, which is dependent on I_{rd}, is small when compared with the first one, can also be neglected as a consequence. Assuming $\tau_m=\frac{k_{pim}L_s+L_s-k_{pim}L_m}{R_s\left(1+k_{pim}\right)}$ and the simplifications, the direct stator flux linkage is:

$$\psi_{sd}^{n}(s)=\frac{\left(s+\frac{1}{\tau_m}\right)}{s^2+\left(\frac{1}{\tau_s}+\frac{1}{\tau_m}\right)s+\omega_s^2}V_{sd}(s) \quad (3.61)$$

$$\psi_{sq}^{n}(s)=\frac{-\omega_s}{s^2+\left(\frac{1}{\tau_s}+\frac{1}{\tau_m}\right)s+\omega_s^2}V_{sd}(s) \quad (3.62)$$

The flux damping is increased, because $1/\tau_m$ can be high depending on the controller adjustment as follows:

- In the case that $k_{pim}=0$:

  $1/\tau_m=1/\tau_s$, and, therefore, the damping is not modified;

- In the case that $k_{pim}\to\infty$:

  $\lim_{k_{pim}\to\infty}\left(\frac{1}{\tau_m}\right)=\frac{R_s}{L_s-L_m}=\frac{R_s}{L_{\sigma s}}$.

Generally, $L_{\sigma s}$ is too small, therefore $1/\tau_m$ is higher than $1/\tau_s$, so the flux damping is increased.

Theoretically, the maximum damping obtained using the magnetizing current control is $\frac{R_s}{2\omega_s}\left(\frac{1}{L_s}+\frac{1}{L_{\sigma s}}\right)$. Of course, choosing k_{pim} requires considering the rotor current control loop dynamics in such a way that the magnetizing current control is not faster than the inner control loop to avoid instability.

If during the sag, the converter is not capable of imposing the demanded voltage, high currents can arise. Therefore, it is important to analyze the behavior of the rotor voltages.

Using Equations (3.61) and (3.62), it is possible to demonstrate that the rotor voltages can be approximated by:

$$V_{rd}(s)=\left[\frac{\frac{L_m}{L_s}s^2+\frac{L_m}{L_s\tau_m}s-\frac{\omega_r\omega_s\left[L_m(1+k_{pim})-L_rk_{pim}\right]}{k_{pim}L_m-L_s\left(1+k_{pim}\right)}}{s^2+\left(\frac{1}{\tau_s}+\frac{1}{\tau_m}\right)s+\omega_s^2}\right]V_{sd}(s)- \\ -\left(\frac{\omega_r\left(k_{pim}L_m^2-k_{pim}L_sL_r\right)}{k_{pim}L_m-L_s(1+k_{pim})}\right)I^*_{mcc}(s) \tag{3.63}$$

$$V_{rq}(s)=\left[\frac{\frac{L_m\omega_s(1+k_{pim})-\omega_sL_rk_{pim}+\omega_r\left(L_m/L_s\right)}{k_{pim}L_m-L_s(1+k_{pim})}s-\frac{\omega_sR_rk_{pim}}{k_{pim}L_m-L_s(1+k_{pim})}+\frac{\omega_rL_m}{L_s\tau_m}}{s^2+\left(\frac{1}{\tau_s}+\frac{1}{\tau_m}\right)s+\omega_s^2}\right]V_{sd}(s)+ \\ +\left[\frac{k_{pim}L_m^2-k_{pim}L_sL_r}{k_{pim}L_m-L_s(1+k_{pim})}s-\frac{R_rk_{pim}L_s}{k_{pim}L_m-L_s(1+k_{pim})}\right]I^*_{mcc}(s) \tag{3.64}$$

Equations (3.63) and (3.64) show that the rotor voltages depends on the stator voltages and it is influenced by control adjustment (k_{pim}). The reference of the magnetizing current control (I^*_{mcc}) appears in these equations, because it is not zero when the reactive stator power is controlled. One can notice that this reference cannot be changed abruptly, because there is a derivative term in the quadrature voltage transfer function as can be seen in Equation (3.64).

This analysis does not address the thermal issue of power semiconductor devices. Then, in the next chapter, the thermal behavior of these devices due to use of the MCC strategy is analyzed and discussed.

3.3.2. Feedback of the stator currents as the reference for the RSC (FSCR)

This strategy proposed by Lima et al. (2010) aims to design a control strategy for reducing the currents in the stator/rotor when a voltage sag occurs. The objective of this strategy is to decrease the stator overcurrents and, as a consequence, the rotor overcurrents that appear in the DFIG windings during the dip. The control feedbacks the measured stator currents as the set point for the current controller of the RSC when the system is subjected to a voltage sag. Thus, the current control system synthesizes rotor currents that generate current waveforms in the stator windings, with the same shape as the currents generated during the dip but in counter phase.

The layout of this strategy is shown in Figure 3.17. As demonstrated, the control system under steady-state conditions would track the PQ-references, while the dashed line of the control diagram of the rotor converter is responsible for controlling the DFIG during the voltage sag when the switch will be placed in position 2. When the switch is turned on, the external PQ control loop gets disconnected, and the rotor currents set point matches the measured values of the stator currents in the *dq* reference frame as indicated below:

$$i_{rd}^{*} = i_{sd} \tag{3.65}$$

$$i_{rq}^{*} = i_{sq} \tag{3.66}$$

It is worth mentioning that the d-axis and q-axis are aligned with the grid voltage in this work, in opposition to the original work in which the axis was aligned with the stator flux. Therefore, there will be some differences in the system modeling.

Considering that the system described by Equations (2.1) to (2.4) is linear, assuming the magnetic circuit of the DFIG is linear, and applying the Laplace transform, the stator currents are as follows:

$$I_{sd}(s)=\frac{(sL_s+R_s)V_{sd}(s)+\omega_s L_s V_{sq}(s)}{(s^2L_s^2+2sL_sR_s+R_s^2+\omega_s^2L_s^2)}-\frac{(s^2L_s+sR_s+\omega_s^2L_s)L_mI_{rd}(s)-R_s\omega_sL_mI_{rq}(s)}{(s^2L_s^2+2sL_sR_s+R_s^2+\omega_s^2L_s^2)} \quad (3.67)$$

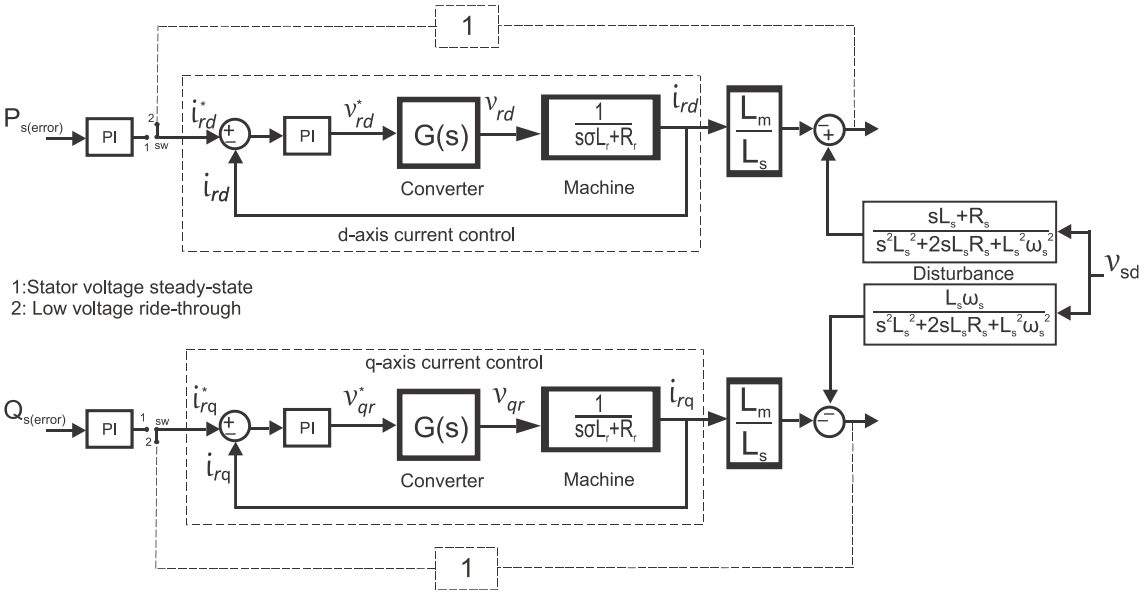

Figure 3.17 - Layout of the proposed control system for the RSC (Adapted from (Lima et al., 2010).

$$I_{sq}(s)=\frac{-\omega_s L_s V_{sd}(s)+(sL_s+R_s)V_{sq}(s)}{(s^2L_s^2+2sL_sR_s+R_s^2+\omega_s^2L_s^2)}-\frac{R_s\omega_sL_mI_{rd}(s)+(s^2L_s+sR_s+\omega_s^2L_s)L_mI_{rq}(s)}{(s^2L_s^2+2sL_sR_s+R_s^2+\omega_s^2L_s^2)}$$

(3.68)

Equations (3.67) and (3.68) can be simplified considering that the stator resistance is very low; thus, $R_s^2 \to 0$. In addition, and considering the reference frame system assumed the stator voltage vector be aligned with the in-direct axis, and hence the v_{sq} can be neglected as well. In this manner, the previous equations can be rewritten as:

$$I_{sd}(s)=\frac{(sL_s+R_s)V_{sd}(s)}{(s^2L_s^2+2sL_sR_s+\omega_s^2L_s^2)}-\frac{(s^2L_s+sR_s+\omega_s^2L_s)L_mI_{rd}(s)-R_s\omega_sL_mI_{rq}(s)}{(s^2L_s^2+2sL_sR_s+\omega_s^2L_s^2)} \quad (3.69)$$

$$I_{sq}(s)=\frac{-\omega_s L_s V_{sd}(s)}{(s^2L_s^2+2sL_sR_s+\omega_s^2L_s^2)}-\frac{R_s\omega_sL_mI_{rd}(s)+(s^2L_s+sR_s+\omega_s^2L_s)L_mI_{rq}(s)}{(s^2L_s^2+2sL_sR_s+\omega_s^2L_s^2)} \quad (3.70)$$

Owing to the low value of the $R_s\omega_s L_m$ coefficient, the crossed terms of the rotor current i_{rd} and i_{rq} can be negligible, as well as $\frac{(s^2L_s + sR_s + \omega_s^2 L_s)}{(s^2L_s^2 + 2sL_sR_s + \omega_s^2 L_s^2)} \cong 1$. Thus, Equations (3.69) and (3.70) become:

$$I_{sd}(s) = \frac{(sL_s + R_s)V_{sd}(s)}{L_s\left(s^2L_s + 2sR_s + \omega_s^2 L_s\right)} - \frac{L_m}{L_s} I_{rd}(s) \tag{3.71}$$

$$I_{sq}(s) = \frac{-\omega_s L_s V_{sd}(s)}{L_s\left(s^2L_s + 2sR_s + \omega_s^2 L_s\right)} - \frac{L_m}{L_s} I_{rq}(s) \tag{3.72}$$

The steady-state equation of the simplified model can be described according with Equations (3.73) and (3.74):

$$i_{sd} = \frac{R_s v_{sd}}{L_s^2\omega_s^2} - \frac{L_m}{L_s} i_{rd} \tag{3.73}$$

$$i_{sq} = -\frac{v_{sd}}{\omega_s L_s} - \frac{L_m}{L_s} i_{rq} \tag{3.74}$$

Considering $R_s \ll$ yields:

$$i_{sd} = -\frac{L_m}{L_s} i_{rd} \tag{3.75}$$

$$i_{sq} = -\frac{v_{sd}}{L_s\omega_s} - \frac{L_m}{L_s} i_{rq} \tag{3.76}$$

Equation (3.75) elucidates the linear relationship between the stator and rotor current components on the in-direct axis. Conversely, the ultimate value of i_{sq} in Equation (3.76) relies on two terms. The first, accounting for steady-state conditions, delineates its correlation with the magnetizing current, while the second term hinges on the rotor's quadrature current component.

In the original, work there is no discuss or analysis that takes into account the thermal issue of power semiconductors when they are affected during voltage sags using this strategy. In this manner, the present work analyzes and discusses such problems in the next chapter.

The original proposal of the strategy did not encompass addressing unbalanced sags. Therefore, this study proposes a modification by integrating it with a resonant control. Additionally, a suggested alteration involves filtering the stator currents using a notch filter set at a frequency of 120 Hz, intending to use these filtered currents as a control reference. Consequently, the strategy exclusively addresses magnetization, delegating management of the negative sequence to the resonant controllers.

3.3.3. Current reference tracking control (CRTC)

This section presents an LVRT strategy for RSC control proposed by Huang et al. (2016). This strategy has the same structure as compared to the strategy seen in the previous subsection but with different characteristics that will be explained with its basic principles as follows.

The stator magnetizing current i_m can be expressed as:

$$\vec{\imath}_m = \frac{L_m}{L_m} \quad \frac{L_m}{L_m} \vec{\imath}_s + \vec{\imath}_r \tag{3.77}$$

Looking the Equation (3.77), it is possible to observe that the stator flux and magnetizing current are related to the stator and rotor currents. Generally, either the stator current or rotor current is directly controlled, and then, the other is indirectly regulated. For example, when the rotor current reference is set to track stator current in a certain proportion:

$$\vec{\imath}_r = k_r \vec{\imath}_s \tag{3.78}$$

where i_r^* presents the rotor current reference, and k_r the tracking coefficient, and here it is assumed to be a real number. Substituting Equation (3.78) in Equation (3.77) yields:

$$\begin{cases} \vec{\imath}_s = \left(L_s / L_m\right) - k_r \vec{\imath}_{sm} \\ \vec{\imath}_r = \left(L_s / L_m\right) - k_r \vec{\imath}_{sm} \end{cases} \tag{3.79}$$

Figure 3.18 depicts the schematic of the control strategy proposed. As shown, if we consider, k_r = -1 this strategy becomes identical to the strategy proposed by Lima et

al. (2010). Another similarity is that during a sag it is not possible to control the active and reactive power of the system.

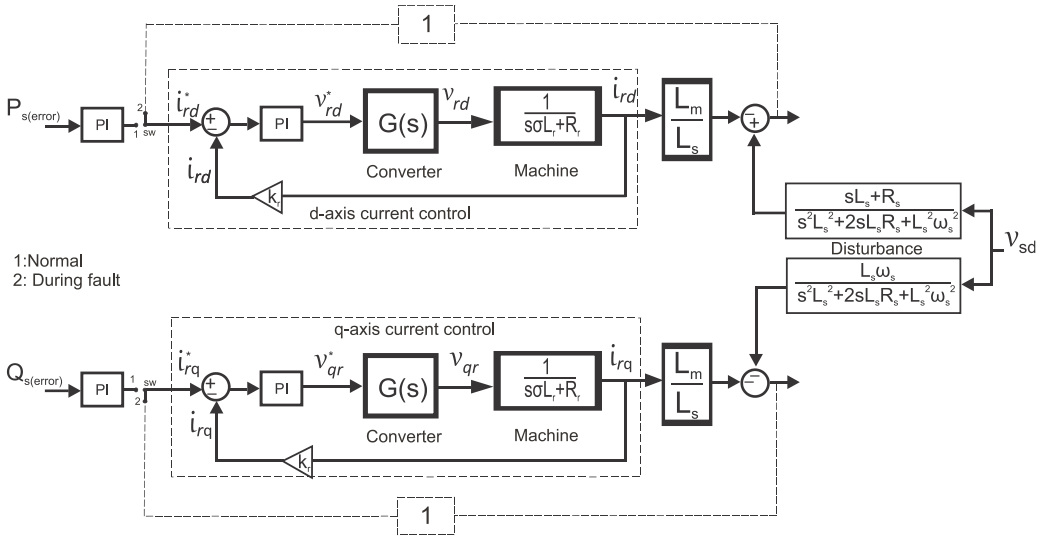

Figure 3.18 - Schematic of the RTFC control strategy propose (Own authorship).

The authors introduced specific constraints on the values of k_r, taking into account the maximum allowable current through the RSC (I_{rmax}) and its maximum voltage output (U_{rmax}), primarily determined by the DC link voltage. These restrictions are outlined in Equations (3.80) and (3.81), respectively.

$$k_r \leq \frac{1}{k_{ms} + \frac{\psi_{s\max}}{L_s I_{r\max}}} \tag{3.80}$$

$$\frac{1 - \frac{U_{r\max}}{E_{r\max}}}{\frac{L_r}{L_m} - \frac{L_m}{L_s}\frac{U_{r\max}}{E_{r\max}}} \leq k_r \geq \frac{L_m}{L_r} \tag{3.81}$$

where ψ_{smax} and E_{rmax} are the maximum amplitudes of stator flux and rotor induced voltage during fault transient, which can be calculated using the Equation (2.13) and (2.17), respectively.

It is important to highlight that the objective of this section is only to present an introduction to the strategy. A more in-depth description can be found in Huang et al. (2016). The authors present studies of the influence of constant k_r only on the behavior of the stator voltage and currents, rotor voltage and currents, and electromagnetic torque. In the view of the above, there is no concern about the thermal stresses that the strategy may

cause in power semiconductors. Thus, this work intends to show how k_r affects the temperature of these components. The results are presented in the next chapter.

3.3.4. PI resonant control (PIRC)

This strategy aims to mitigating the effects caused by unbalanced voltage sags. Based on the principle of controlling the negative-sequence components, the authors in Hu et al. (2008), Hu and He (2009) and Hu and He (2011) proposed the use of resonant controllers for the positive synchronous reference frame instead of decentralizing the control system into two loops associated with the positive-sequence and negative-sequence components. This method relies on the strategy used to mitigate harmonics in VSCs as described in Liserre et al. (2006).

The structure of the PI resonant control (PIRC) is similar to the classical control presented in Figure 3.4 and Figure 3.10, as can be seen in Figure 3.19 which represents the GSC control and Figure 3.20 depicts the RSC control. The classical PI controller used in the currents loops are replaced with a PI plus resonant (PI + R) controller tuned at the twice the grid frequency, that is, the frequency of the negative-sequence component in the positive synchronous reference frame, resulting in the following transfer function:

$$G(s) = K_p + \frac{K_i}{s} + \frac{sK_r}{s^2 + (2\omega_s)^2}, \tag{3.82}$$

where K_p is the proportional gain; K_i is the integral gain; and K_r is the resonant gain, whose adjustment is discussed in the following subsection.

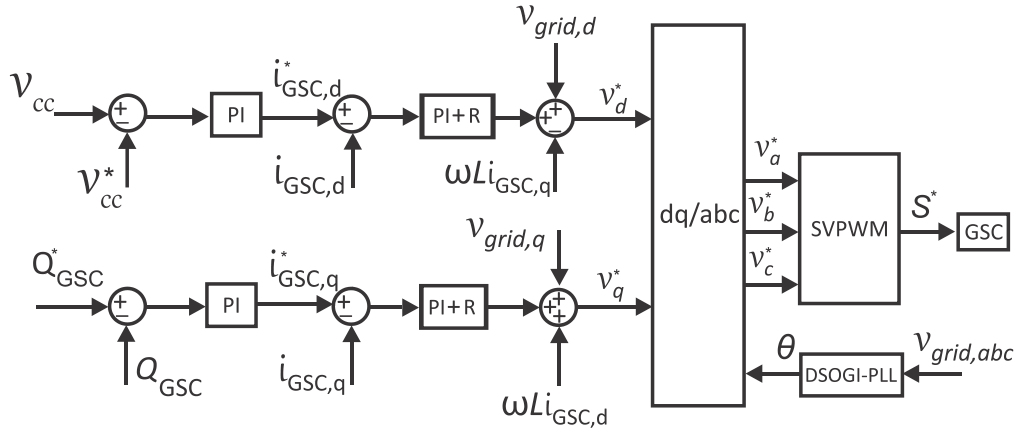

Figure 3.19 - Block diagram representation of the GSC PIR control structure (Own authorship).

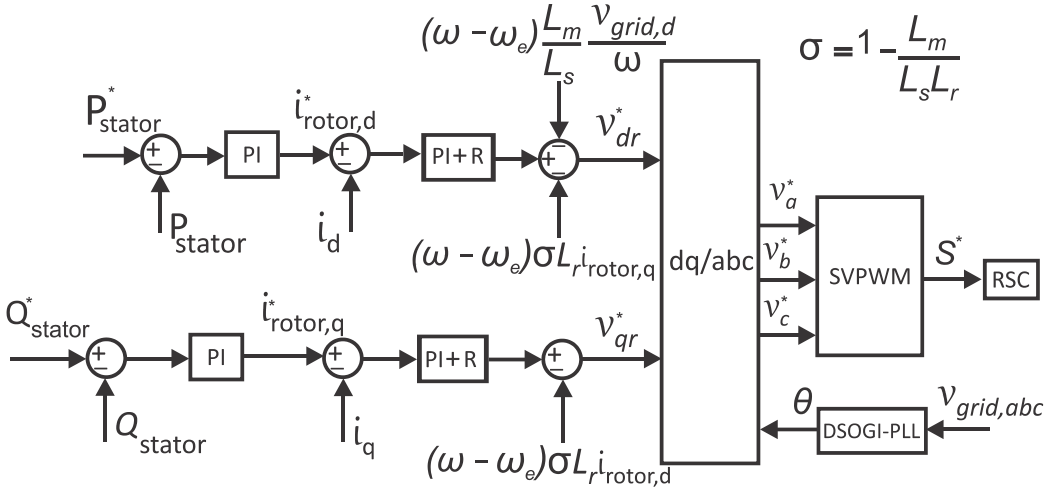

Figure 3.20 - Block diagram representation of the RSC PIR control structure (Own authorship).

3.3.4.1. Mathematical modeling during voltage sags

As in Section 2.2, this subsection follows a similar approach, but with the incorporation of resonant control. Further details on this development can be found in Mendes et al. (2011).

To determine the resonant gain (K_r), an analysis of the controller frequency response is crucial. Figure 3.21 displays the bode diagram of the controller transfer function, as described in Equation (3.82), with various resonant gains. It is evident that increasing the gain enhances the controller's response at the $2\omega_s$, but it also affects frequencies in the surrounding vicinity. When choosing an appropriate gain, it is essential to ensure that the gain at $2\omega_s$ is high, while also ensuring that the resonant peak is not excessively wide.

When it comes to digital implementation, the discretization method is a critical consideration in designing the resonant controller. Depending on the chosen method, the resonant peak may be attenuated, and the frequency may be shifted. In this work, Tustin's method was employed owing to its simplicity and effectiveness.

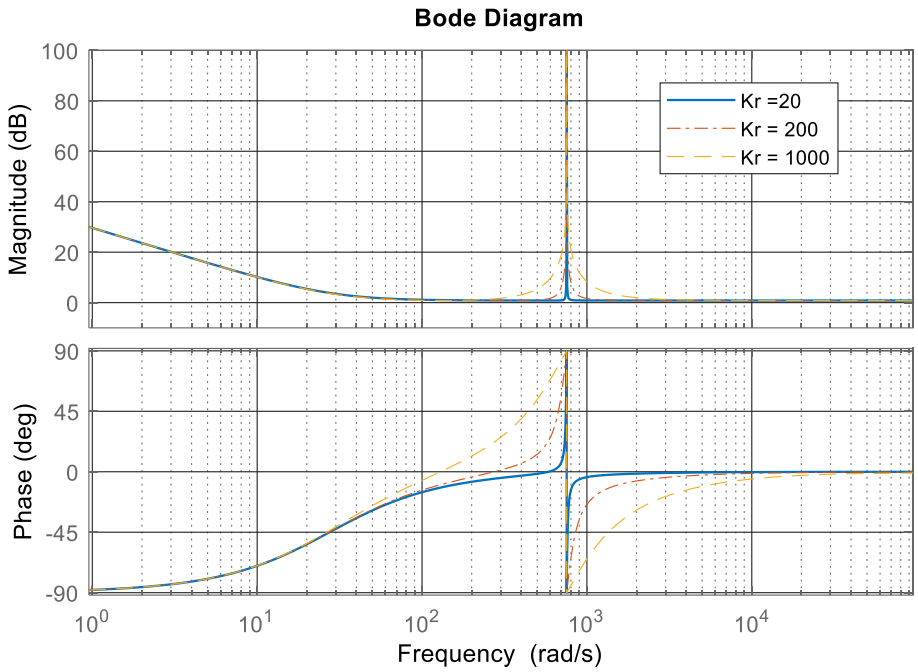

Figure 3.21 - Bode diagram of the PIRC controller for different gains.

However, even after determining the best gain for the resonant control, success in damping the negative-sequence component is not guaranteed. This is due to the fact that, depending on the severity of the sag imposed on the system, it can lead to a high induced voltage in the machine rotor. This phenomenon is illustrated in the calculations presented in Equation (2.27) and allow us to ascertain the voltage induced in the rotor in relation to the dip level.

3.3.5. Magnetizing current control + resonant control (MCCR)

The preceding control strategy demonstrates its ability to control the negative sequence of the rotor current effectively during unbalanced voltage sags, as long as the RSC voltage limits are not exceeded. However, in unbalanced sags, the presence of the natural component may or may not be observed. When the natural component is present, the previous strategy is incapable of mitigating the oscillations caused by it. To address this challenge and eliminate both the negative sequence and the natural component, Mendes (2013) introduced the concept of Magnetizing Current Control in conjunction with Resonant Control (MCCR).

Figure 3.22 shows the block diagram of the MCCR strategy, which is very similar to the one shown and explained in section 3.3.1 of this chapter. It is worth mentioning that the negative sequence component of the magnetizing current is removed through a notch filter tuned at 120 Hz. Thus, only the positive-sequence component of the magnetizing current is used in the control and it is given by Equation (3.83).

$$i_{m+}^{+} = -(i_{rq+}^{+} + i_{sq+}^{+}) \tag{3.83}$$

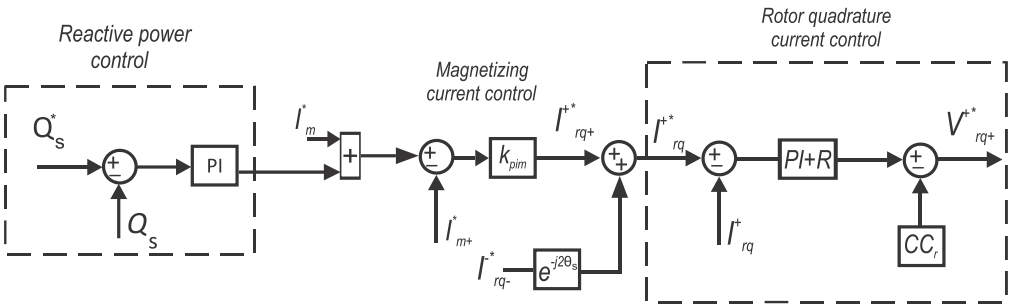

Figure 3.22 - MMCR block diagram (Adapted from (Mendes, 2013)).

3.4. Thermal analysis of converters in WECSs

As seen in Chapter 2, there are several works that study the DFIG under voltage sags and propose RTFC strategies. However, the losses and thermal behavior of the semiconductors when the DFIG is under voltage sags are an important and interesting topic that deserves further investigation.

Zhou and Blaabjerg (2013) analyzed and simulated the power losses and thermal cycling of the most popular WECSs, specifically the Permanent Magnetic Synchronous Generator (PMSG) and Doubly Fed Induction Generator (DFIG), during balanced voltage sags. In the case of the PMSG system, the analysis and results were conducted on the converter connected to the grid. Conversely, for the DFIG system, the focus was on the converter connected to the rotor. The study involved simulating various sag values and comparing the thermal behavior of the two systems by analyzing junction temperatures and thermal fluctuations of semiconductor devices. The comparison revealed the DFIG system's vulnerability to these disturbances. However, the study did not include an analysis using LVRT strategies to mitigate these adverse effects.

Zhou et al. (2014a) presented simulation results regarding the thermal behavior of the DFIG during balanced grid faults. The focus of the investigation was on the impact of rotor current on the stator flux damping time. The study underscores the significance of a well-designed converter power module, as severe voltage sags can lead to increased power losses, elevated junction temperature fluctuations, and may even pose a risk of damage to the rotor converter.

Few papers in the literature delve into the thermal behavior of the Doubly Fed Induction Generator (DFIG) during grid disruptions, and the number of recent studies is limited. Zhou et al. (2018) introduced an optimized demagnetizing control strategy to maintain a constant maximum rotor current in the DFIG system between the occurrence of faults and the injection of reactive current. The study provides insights into the thermal behavior of power devices under various values of voltage sags and rotor speeds. Additionally, the research includes the validation of these findings through experimental results conducted on a high-power test bench.

However, it is important to note that these works exclusively focuses on thermal analyses when the system faces balanced voltage sags. The studies lack an examination of the thermal behavior of power semiconductors in the presence of unbalanced sags. To the best of the author's knowledge, there is a noticeable absence of literature addressing this specific aspect of the study.

The reliability of the converter is a critical aspect that warrants careful examination. Fault-tolerant power electronic converters have the ability to adapt and compensate for random failures that may arise during their anticipated lifespan. However, concerning the mitigation of thermal stress, the adoption of such converters may pose challenges. This is attributed to the fact that they increase the number of components within the system, consequently resulting in higher power losses.

Peyghami et al. (2020) provide a comprehensive overview of reliability in contemporary power systems. The study delineates the challenges stemming from grid modernization and introduces a novel framework for assessing the reliability of modern power systems. The research explores the impact of grid modernization on the adequacy and security of power systems, elucidating how modifications can be made to incorporate the influence of modern technologies into enhancing power system reliability.

Hahn et al. (2017) conducted a reliability analysis of modular power converters to optimize the electrical and thermal design of power semiconductors. In a related study, Zhou et al. (2018) explored the design lifetime of power converters in a 2.0 MW DFIG wind turbine, establishing new design criteria for power modules with a focus on reliability. Notably, the thermal analysis of power semiconductors in this work does not provide insights into the system's resilience in the presence of voltage sags.

While numerous works in the literature delve into the reliability subject, it is essential to clarify that the focus of this particular work does not encompass a comprehensive exploration. Consequently, only a select few papers will be cited, providing the reader with an awareness of existing studies and a concise summary of the current state of the art. These referenced works approach the thermal profiles of semiconductor components from a distinct perspective, conducting analyses over extended periods to identify potential failures that these components might encounter.

3.4.1. Thermal modelling

This subsection delves into the thermal considerations of power electronics converters. Within the power stage of such converters, alongside capacitors and inductors, semiconductor switches play a crucial role. These switches dissipate a portion of energy in the form of heat, contributing to an increase in device temperature. Efficient management of this thermal energy is essential to prevent semiconductor switch failure. This is typically achieved through the use of a heat sink. Therefore, an important aspect of the power electronic converter design involves the implementation of an appropriate thermal design, specifically the design of a suitable heat sink.

In this subsection, a thermal design leveraging the thermal analysis capabilities of PLECS is outlined. The energy losses in the semiconductor switches are modeled using datasheet information. The total energy losses are then calculated using PLECS, and a heat sink is designed accordingly for the converters.

The steps outlined by Asadi and Eguchi (2020) for conducting the thermal modeling of the converter in the DFIG system are detailed in the following subsections.

3.4.1.1. Power module choice

This selection is based on the electrical parameters of the simulated system, as outlined in Table 3.1. Many manufacturers recommend a module capable of withstanding a voltage approximately 60% of the DC-link voltage. In view of this, IGBT power modules with a blocking voltage of 1200 V were chosen. It is crucial that this module can handle the maximum current generated in the machine rotor, which, under rated conditions, reaches an approximate value of 1000 A. Consequently, the selected module is FF1500R12IE5 by Infineon and its characteristics are provided in Table 3.4. Additionally, its circuit diagram is illustrated in Figure 3.23.

Table 3.4 – Module information.

Parameter	Value
Collector-emitter voltage	1200 V
Continuous DC collector current	1500 A
Repetitive peak collector current	3000 A
Maximum junction temperature	175°C

Figure 3.23 – FF1500R12IE5 circuit diagram.

With a current capacity exceeding the rated current of the machine rotor, theoretically, employing only one module per phase would be sufficient for the safe operation of the system under normal conditions. Despite the GSC having a lower maximum current (800 A) compared to the RSC, the same module designed for the RSC is utilized in the GSC. This practice is common to streamline maintenance procedures.

3.4.1.2. Thermal description of semiconductor devices

To calculate the losses of the converters and simulate the thermal performance of the converter, it is essential to first establish thermal loss descriptions for the semiconductors. This involves creating thermal descriptions for the IGBTs and diodes using the datasheet for the power module selected in the previous subsection. The required information for each component includes conduction losses, switching losses, and thermal impedance between the junction and case.

3.4.1.2.1. Switching losses

The current and voltage of a semiconductor switch do not change instantaneously, as illustrated in Figure 3.24.

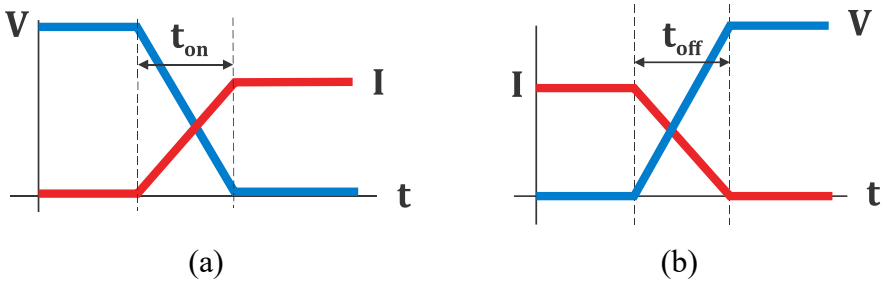

Figure 3.24 - The semiconductor switch: (a) turns on and (b) turns off (Own authorship).

As depicted in Figure 3.24, during the off-state (t_{off}) or on-state (t_{on}), the current and voltage are not zero. Consequently, their product, i.e., the power loss, is also not zero. The power lost during the turn-on phase is referred to as turn-on switching loss, while the power lost during the turn-off phase is termed turn-off switching loss. Switching loss occurs exclusively during transitions, specifically when an on-state device turns off or when a device turns on. The switching losses in the IGBT can be incorporated into the PLECS platform through its thermal library.

The plot that allows for calculating the switching losses in the IGBT is presented in Figure 3.25. The datasheet provides switching losses data for two temperatures, 125 ºC and 175 ºC. Parameter E_{on} is used to model the turn-on losses, while E_{off} represents the turn-off losses. Figure 3.26 presents a screenshot of PLECS thermal library, which allows for incorporating the losses into the model.

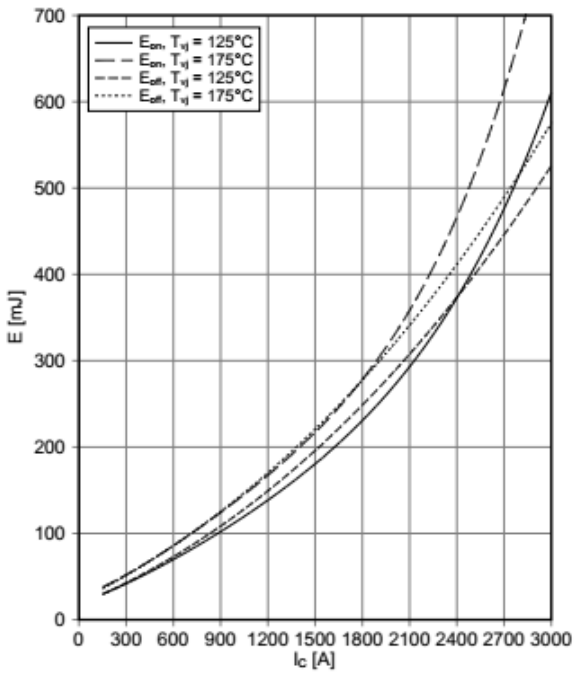

Figure 3.25 - IGBT switching loss characteristic curves of module FF1500R12IE5, considering a gate resistance of 0.82 Ω (Infineon, 2017).

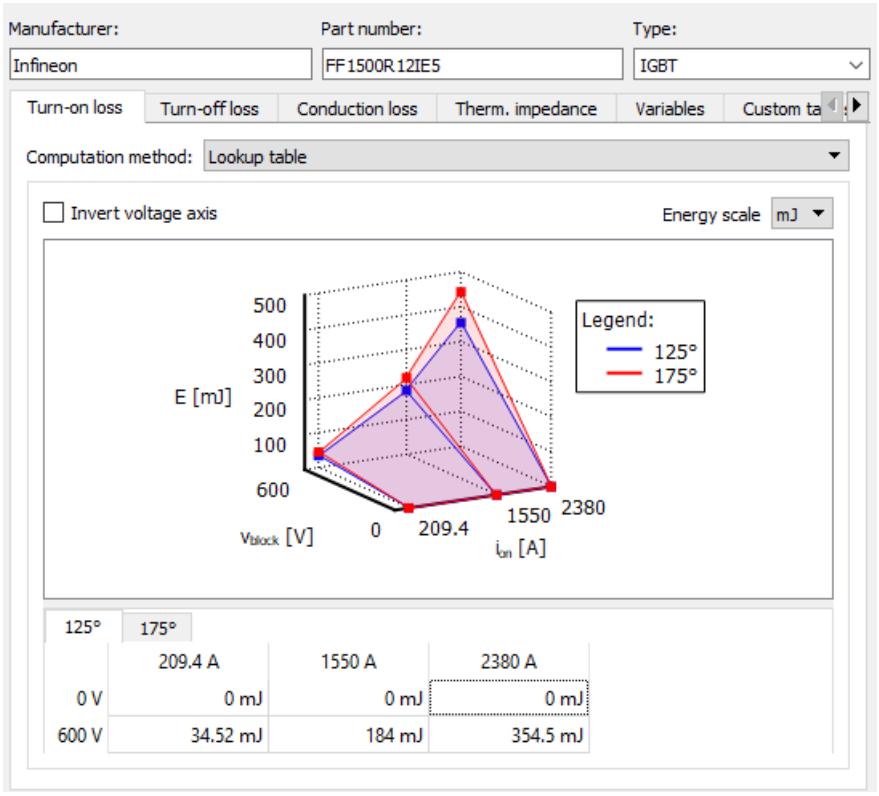

Figure 3.26 - Turn-on losses represented in PLECS thermal library.

The turn-on and turn-off losses of the IGBT depend on factors such as load current, electrical load type (ohmic, inductive, capacitive), DC-link voltage, junction

temperature, and switching frequency. Equation (3.84) demonstrates the calculation of switching losses, as per the method outlined by Wintrich et al. (2011).

$$P_{sw} = f_{sw} \cdot (E_{on}(V_{in}, I_{out}, T_j) + E_{off}(V_{in}, I_{out}, T_j) \tag{3.84}$$

where V_{in} is the voltage applied, I_{out} is the output current, and T_j is the junction temperature.

The process of modeling diode switching losses closely parallels that of modeling IGBT switching losses. The parameters associated with the switching loss curve for the diode are considered, as depicted in Figure 3.27. However, special attention must be given to diode turn-on, as no storage charge is initially present in the device. The injection of minority charges is typically very rapid, and in some cases, this charging can be treated as recovered energy to the system, resulting in seemingly negative losses during the turn-on sequence(Erickson and Maksimovic, 2007). Consequently, the turn-on losses are neglected and can be disregarded, with only turn-off losses being deemed relevant and modeled.

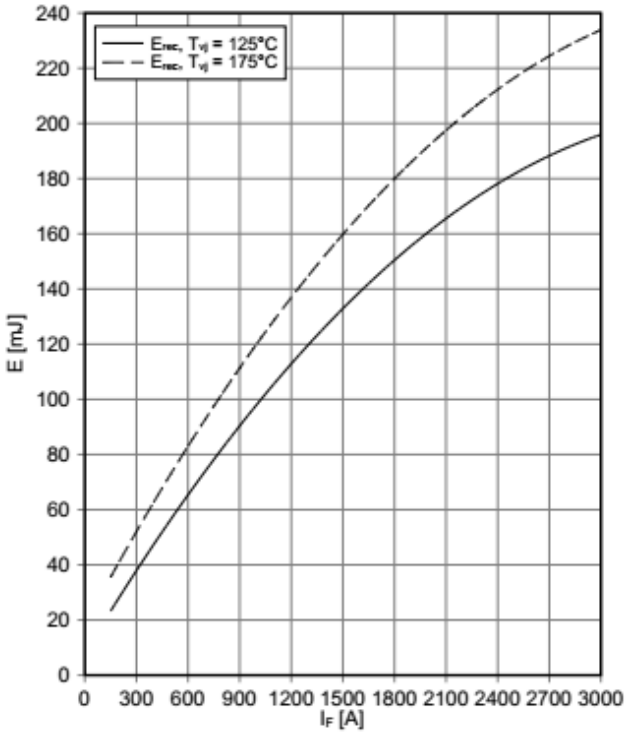

Figure 3.27 - Diode recovery energy characteristic curves of module FF1500R12IE5, considering a gate resistance of 0.82 Ω (Infineon, 2017).

The turn-off losses (P_{rr}) are dependent on the load current, the DC-link voltage, the junction temperature and the switching frequency. From equation (3.85), the switching losses can be calculated as follows:

$$P_{rr} = f_{sw} \cdot E_{rr}\left(V_{in}, I_{out}, T_j\right) \tag{3.85}$$

3.4.1.2.2. Conduction losses

The switching losses are not the sole losses of a semiconductor switch. Once the transient phase is completed, and the device attains a steady state, some power is dissipated in the form of heat due to the inherent resistance in the semiconductor junction. This type of power loss is referred to as conduction loss.

The conduction losses of the IGBT can be incorporated into the PLECS platform using its thermal library. This involves inserting data from the curves of collector current vs. collector-emitter voltage for different junction temperatures into the conduction loss tab. Figure 3.28 illustrates these curves for the module used in this work.

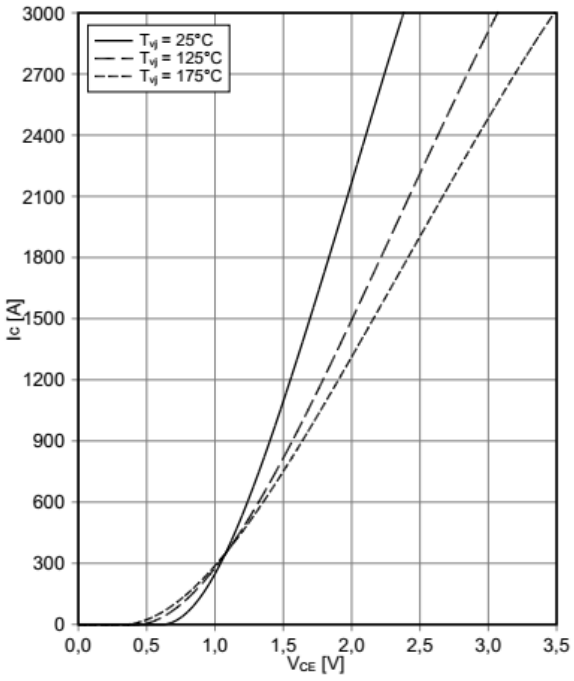

Figure 3.28 - IGBT characteristic curve module FF1500R12IE5 (Infineon, 2017).

The datasheet supplies conduction losses for the IGBT at three distinct temperatures: 25 ºC, 125 ºC, and 175 ºC. A partial result of modeling the conduction losses of the IGBT is illustrated in Figure 3.29.

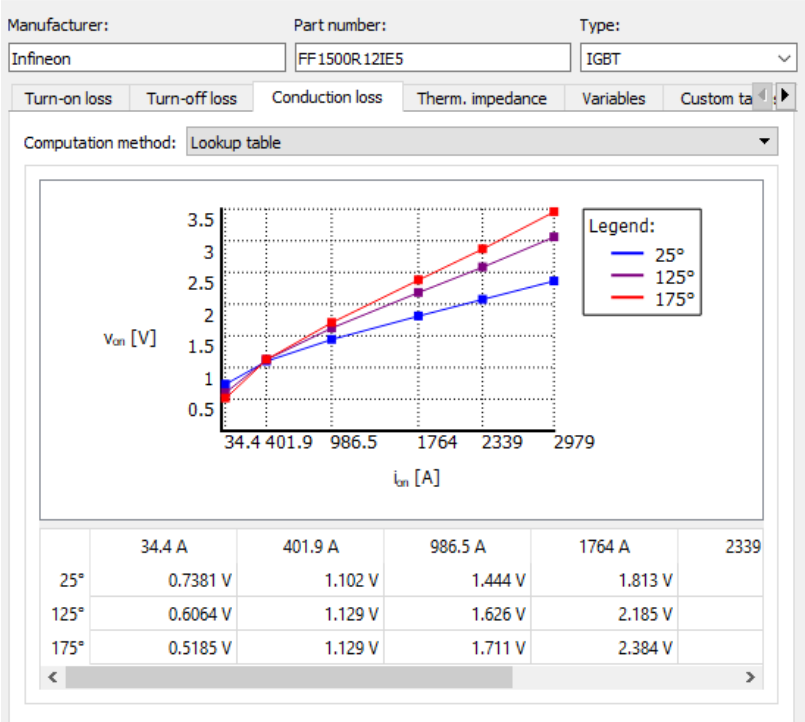

Figure 3.29 - Conduction losses represented in PLECS thermal library.

The on-state power dissipation ($P_{cond(T)}$) is dependent on the load current (over output characteristic ($V_{CE(sat)} = f(I_c, V_{GE})$), the junction temperature, and the duty cycle. From the IGBT conduction characteristic curve and equation (3.86), it is possible to obtain the conduction losses.

$$P_{cond(T)} = \frac{1}{T}\int_0^{t_t} i_c(t) \cdot v_{CE}(t)dt \tag{3.86}$$

where i_c is the collector current and V_{CE} is the collector-to-emitter.

The conduction losses of the diode can be modeled using the same principle as demonstrated in the IGBT. The tables associated with conduction losses are filled based on the curve depicted in Figure 3.30.

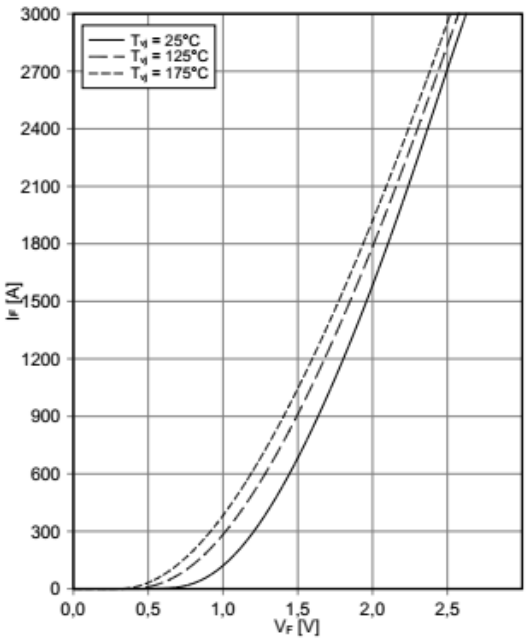

Figure 3.30 - Forward characteristic of diode of module FF1500R12IE5 (Infineon, 2017).

As with the IGBT, the losses in the freewheeling diode are detailed as follows. The on-state power dissipation ($P_{cond(D)}$) is dependent on the load current considering the output characteristic $V_F = f(I_F)$; the junction temperature; and the duty cycle.

Using equation (3.87), it is possible to calculate the conduction losses.

$$P_{cond(D)} = \frac{1}{T}\int_{t_1}^{T} v_F(t) \cdot i_F(t) dt \tag{3.87}$$

where v_F is the forward voltage and i_F is forward current.

3.4.1.2.3. Thermal impedances

The datasheet provides the junction-case transient thermal impedance curves for both the IGBT and diode, along with coefficients for a four-stage Foster network. Figure 3.31 illustrates the junction-case transient thermal impedance curve for the IGBT.

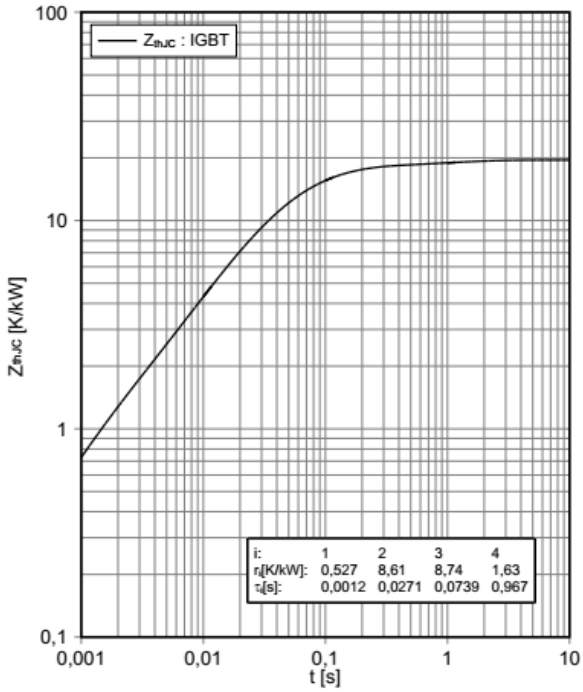

Figure 3.31 - IGBT's junction-case transient thermal impedance (Infineon, 2017).

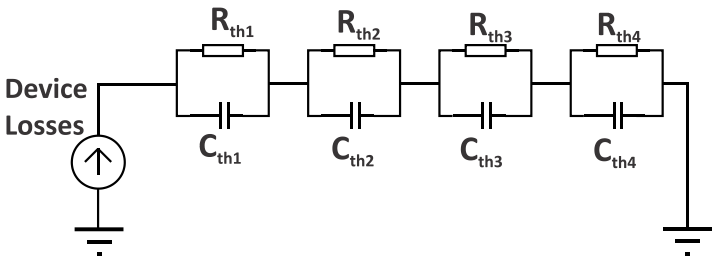

Figure 3.32- Foster network (Own authorship).

The Foster coefficients should not be utilized unless the case temperature of the device is maintained constant. The presence of series-connected capacitors in the Foster network (Figure 3.32) causes temperature variations at the case end of the chain to promptly propagate back to the junction end, thereby invalidating the transient response.

If the case temperature is not constant, a more suitable approach is to represent the junction-case thermal impedance using a Cauer network, as illustrated in Figure 3.33.

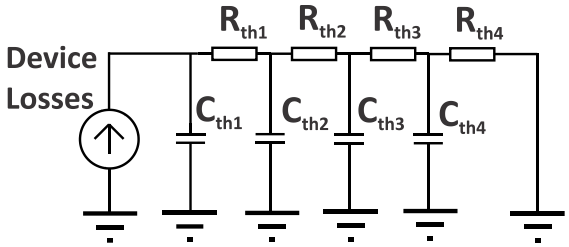

Figure 3.33 - Cauer network (Own authorship).

The resistance can be obtained from the thermal impedance curve. The transient thermal impedance curve corresponds to the step response and therefore contains the full thermal description of the system. The thermal impedance of a partial fraction model can be expressed as defined in (Infineon, 2015):

$$Z_{th}(t) = \sum_{i=1}^{n} r_i \left(1 - e^{-\frac{t}{\tau_i}} \right) \tag{3.88}$$

where:

$$\tau_i = r_i c_i \tag{3.89}$$

The capacitance c_i is calculated using equation (3.89), where τ_i is the time constant determined as the time taken for the resistance r_i to reach 63% of its final value.

Internally, PLECS consistently employs the Cauer network to calculate thermal transitions. Foster networks are converted to Cauer networks at the beginning of the simulation. Xu et al. (2021)Xu et al. (2021) conducted a study comparing Foster and Cauer networks, highlighting their respective advantages and disadvantages. This work reveals that the Foster model exhibits limitations during transient phases, but it demonstrates a robust response in steady-state conditions. On the other hand, the Cauer model exhibits a strong response during transients, but it may require a longer time to reach the steady-state condition.

The thermal impedance of the IGBT and diode can be incorporated into the PLECS platform through its thermal library. This involves inserting the Foster parameters provided by the datasheet of the power module into the impedance tab. Figure 3.34 displays the result of this insertion.

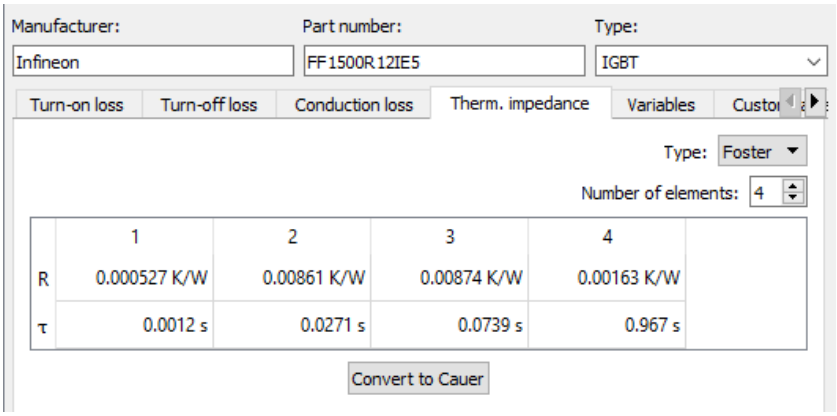

Figure 3.34 - Thermal impedance in PLECS thermal library.

3.4.2. Heatsink design

A diverse array of heatsinks is available on the market, spanning from large aluminum plates tailored to cool extensive sets of power modules to smaller plates designed for the cooling of individual components. Various cooling methods are also employed, including air cooling, forced air cooling, heat pipes, water cooling, among others. For additional details, Wintrich et al. (2011) provides comprehensive insights into these cooling methods. The arrangement of heatsinks used for the GSC and RSC modules are shown in Figure 3.35.

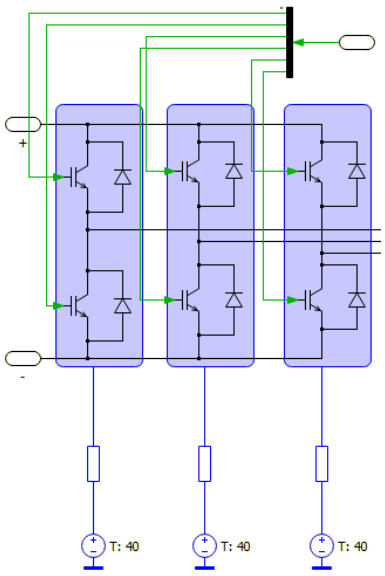

Figure 3.35 – Heatsinks used in the GSC and RSC.

Using the measured average power loss and assuming a worst case heat sink temperature of 80ºC, one can calculate the thermal resistance through equation (3.90).

$$R_{th} = \frac{T_{hs} - T_{amb}}{P_{loss}} \tag{3.90}$$

where R_{th} is a thermal resistance, T_{hs} is a heat sink temperature, T_{amb} is the ambient temperature and P_{loss} is the average power loss.

The ambient temperature is assumed as 40 ºC. To determine P_{loss}, the system was simulated at rated conditions and normal operation according to Table 3.1 and Table 3.2. Figure 3.36 shows that the average power loss is about 1550 W. So, the heat sink thermal resistance is 0.026 ºC/W.

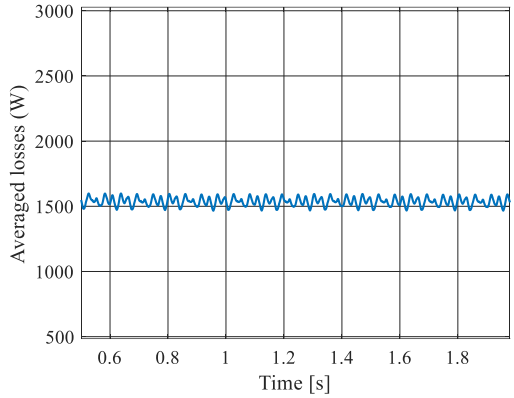

Figure 3.36 - Averaged power loss.

The thermal capacitance of a heatsink is typically not explicitly calculated, but it depends on factors such as the mass of the heatsink and the type of material used. The thermal capacitance is not as critical because the thermal resistance primarily determines the steady-state operating temperature. The thermal capacitance, which measures the heat storage ability of the heatsink, mainly influences the rate of temperature rise during transient overload conditions. In this work, the thermal capacitance is neglected since the primary focus is on the thermal loading of power semiconductors.

Figure 3.37 provides a comparison of semiconductor device temperatures with and without thermal capacitance. This test was conducted under normal operating conditions. In addition, the thermal capacitance has minimal influence on the temperature of the devices once the system reaches a steady state. Nevertheless, the temperature of the diode is influenced by the temperature of the IGBT, and vice versa, as these components are arranged in the same case.

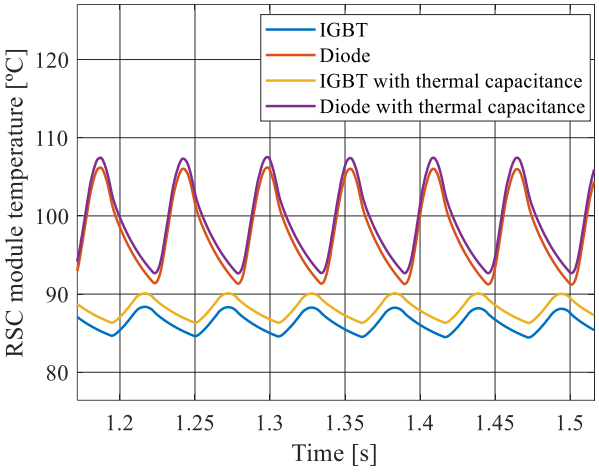

Figure 3.37 - Temperatures of semiconductor devices considering or not the heat sink thermal capacitance.

3.5. Chapter closure

This chapter has provided in-depth insights into the DFIG technology. The components of the system were introduced and mathematically modeled. Control strategies to be examined were presented and elaborated upon, followed by block diagrams that elucidate their fundamental principles of operation. By comprehending the entire mechanism underpinning the control strategy, simulations become more accessible, facilitating the validation of theoretical concepts

A state-of-the-art review of thermal analysis of power converters in WECS was conducted, presenting works that offer perspectives on thermal stresses on power semiconductors. This survey revealed a scarcity of recent literature providing thermal analyses of these devices, especially concerning RTFC strategies. Notably, a gap in the literature was identified, as there is a lack of studies analyzing the thermal behavior of semiconductor devices when subjected to unbalanced voltage sags.

In summary, the thermal modeling was elucidated, providing insight into the criteria adopted in the thermal design of semiconductor devices.

To design a power converter that is reliable and safe, attention must be paid to some issues:

- The design considerations for the power converter module include increasing the maximum voltage value it supports by 60% above the DC bus voltage value specified in the project
- The determination of the maximum current for the power converter involves estimation, with the understanding that its direct impact on module heating necessitates thorough consideration during the thermal design phase. The thermal design will ultimately dictate whether the specified conditions are met or not.

The PLECS software's thermal library is equipped with various capacities, tools, and functions that contribute to understanding and comprehending the thermal behavior of semiconductor devices within power converters.

The upcoming chapter, leveraging the thermal model and knowledge of the DFIG topology, will delve into studies exploring the electrical and thermal behavior of the system under both balanced and unbalanced voltage sags.

Chapter 4. **SIMULATION RESULTS**

4.1. Balanced voltage sags

4.1.1. Classical control

To understand the behavior of the WECS based on DFIG technology during balanced voltage sags, this chapter presents simulation results for the system described in the preceding chapter, as per the specifications summarized in Table 3.1 and Table 3.2. The analysis focuses on the onset of the sag, since this moment poses the greatest challenge to the system, and recovery typically occurs more smoothly. In the initial tests, no RTFC strategies are employed, and the generator operates at supersynchronous speed (2340 rpm) and rated power (2 MW).

In a steady-state condition, the stator flux is a vector rotating at synchronous speed in relation to the stator, with an amplitude proportional to the grid voltage. The reactive current energizes the magnetic field, amplifying the flux within the air gap. A sudden voltage drop in the stator terminals induces fluctuations in the stator flux, leading to a surge in the transient current through the rotor windings. According to Equation (2.13), the stator flux can be represented by two components: a fixed DC flux that decays with the stator time constant and an AC flux that rotates at synchronous speed in the complex plane. Figure 4.1 shows the stator flux behavior during a 20% balanced three-phase voltage sag.

Figure 4.2 represents the behavior of the spatial vector of the stator flux in the complex plane before and during the dip. The larger circle represents the steady state before the sag, indicating the forced flux generated by the initial voltage. As the dip commences, the forced flux due to the voltage sag traces a circular trajectory, albeit with a reduced amplitude. Simultaneously, the continuous component of the flux (natural) gradually diminishes, shifting the vector's circle towards the center of the plane. Following the transient period, a new steady state is attained, represented by the smaller circle.

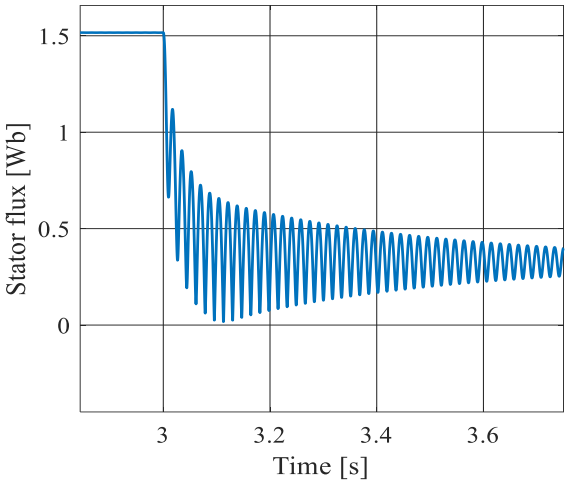

Figure 4.1 - Stator flux during balanced voltage sag.

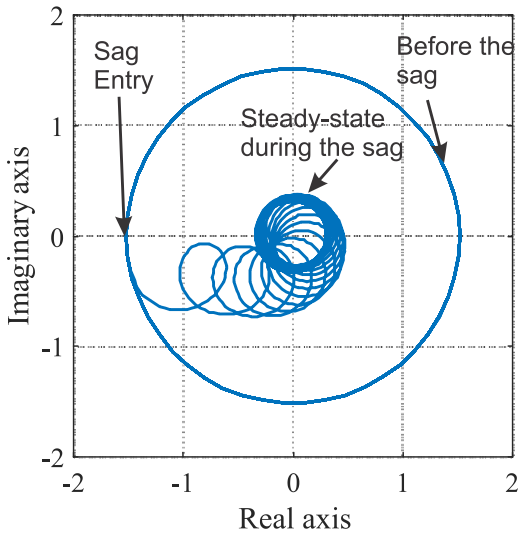

Figure 4.2 – Spatial vector of the stator flux in complex plane.

Figure 4.3 illustrates the stator currents, while Figure 4.4 represents the rotor current. Of particular interest in sag analysis is the rotor current because induced voltages in the rotor can result in overcurrent, potentially damaging the converter.

It is observed that, when the sag occurs, the rotor current peak reaches almost 4 times the current under normal conditions. This occurs due to the swift and high-amplitude fluctuations in the rotor voltage induced by the natural flux, which gradually decays in accordance with the stator time constant. This relationship is evident in equation (2.15), where the voltage amplitude increases with the severity of the sag and the rotational speed of the machine.

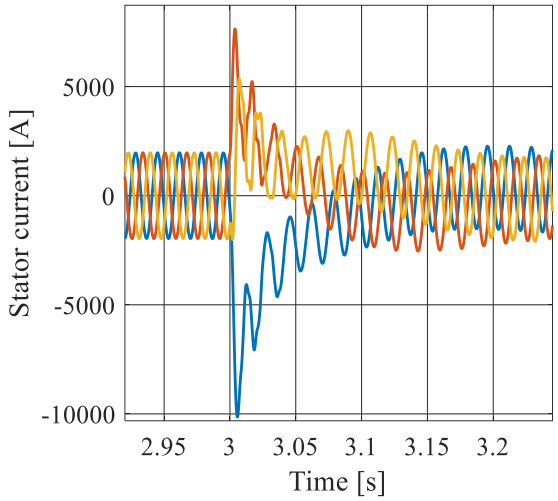

Figure 4.3 – Stator currents during a 20% balanced voltage sag without RTFC strategies.

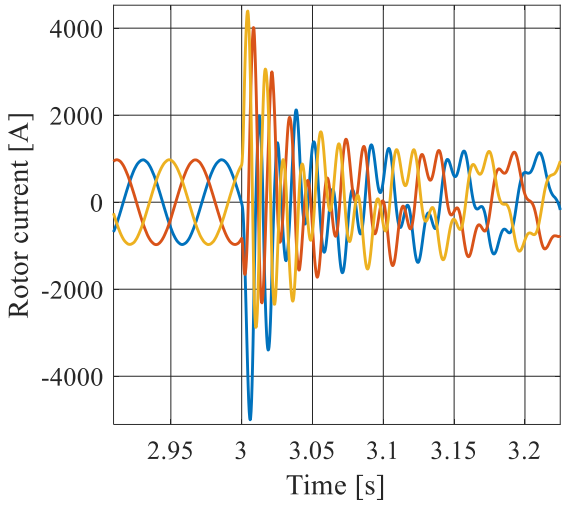

Figure 4.4 – Rotor currents during a 20% balanced voltage sag without RTFC strategies.

In Figure 4.5, the direct and quadrature currents of the RSC are depicted. These components experience a sudden surge at the dip's onset due to the induced natural component in the rotor voltage. Additionally, it is notable that the direct reference remains constant at the maximum value set by the RSC control (maximum 1500 A). In this case, the quadrature current reference, which is responsible by the reactive power, remained zero. The grid codes require the reactive current feedback, but it was omitted a priori for simplicity.

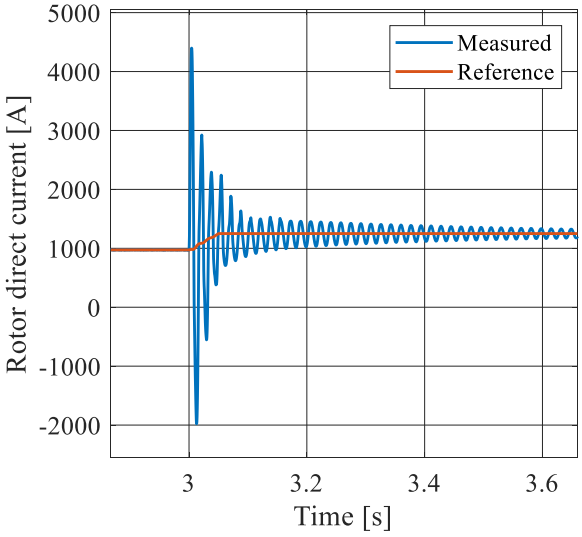

(a)

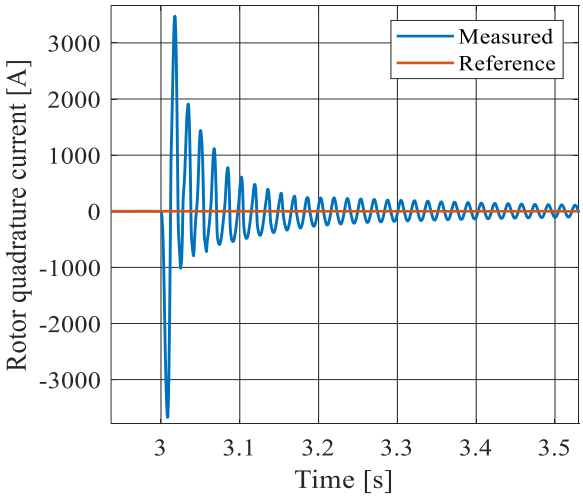

(b)

Figure 4.5 - RSC currents during a 20% balanced voltage sag without RTFC strategies: (a) direct axis and (b) quadrature axis.

The rotor current oscillations also reflect on the GSC currents and the DC-link voltage. Figure 4.6 shows that at the sag's onset, the DC-link voltage tends to rise due to the substantial flow of rotor currents into the capacitor. Consequently, according to Figure 4.7, the GSC currents increase to maintain a constant DC-link voltage and keep the power transfer constant. To prevent the converter damage, a brake chopper is employed to limit the DC-link voltage to a maximum of 733 V.

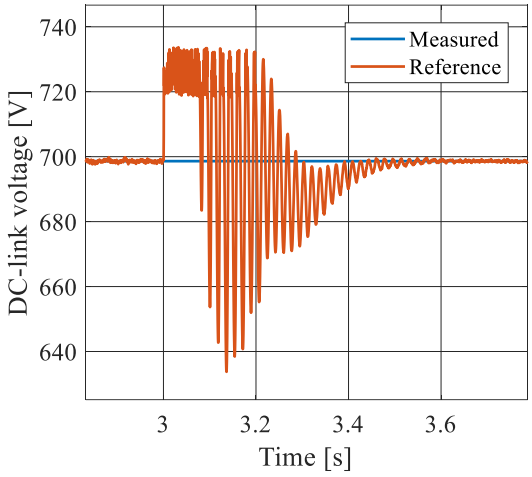

Figure 4.6 - DC-link voltage during a 20% balanced voltage sag without RTFC strategies.

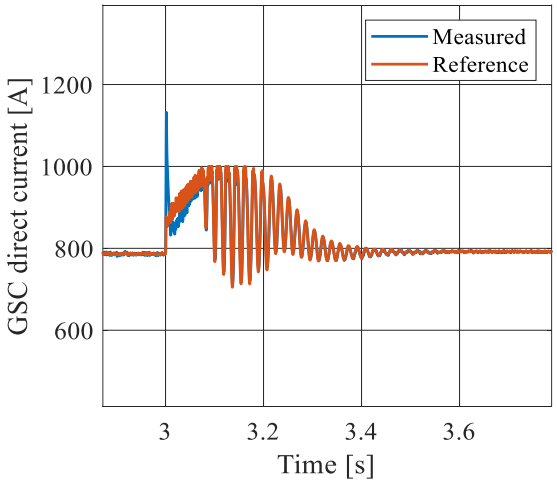

(a)

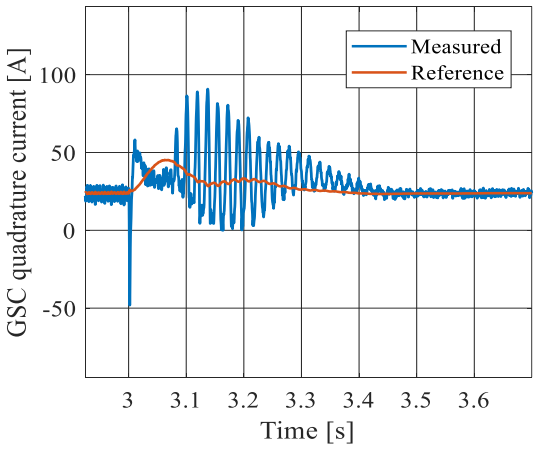

(b)

Figure 4.7 – GSC currents during a 20% balanced voltage sag without RTFC strategies: (a) direct axis and (b) quadrature axis.

The impact of the natural component on the power transmitted through the stator is evident as depicted in Figure 4.8. The fluctuations observed in the generated power, resulting from the natural component of the stator flux, are undesirable as they deteriorate the grid power quality, which is already compromised by the MVS. All power quantities are negative, thus denoting the energy injection into the grid.

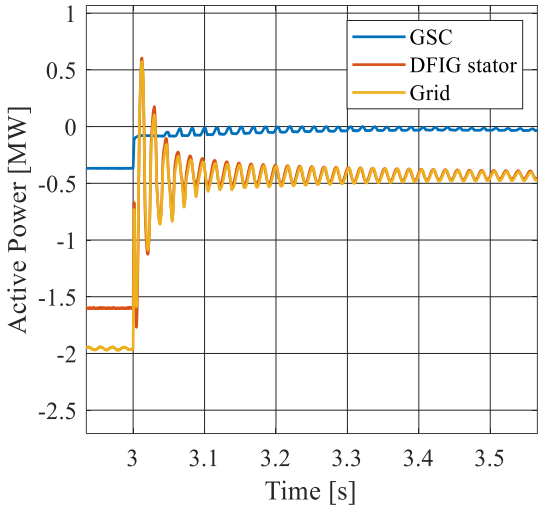

Figure 4.8 - Active powers during a 20% balanced voltage sag without RTFC strategies.

As semiconductors components are subjected to the harmful impacts generated by voltage sags, an analysis of the junction temperature behavior of these devices is shown. Figure 4.9 and Figure 4.10 evidence the junction temperatures for the GSC and RSC modules, respectively.

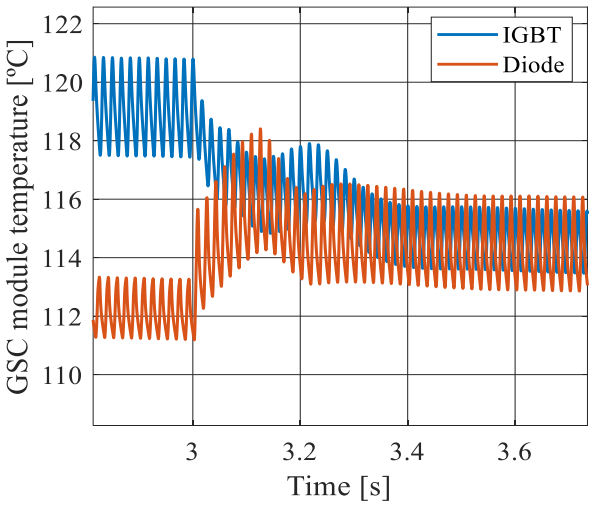

Figure 4.9 – Junction temperature of the GSC module during a 20% balanced voltage sag without RTFC strategies.

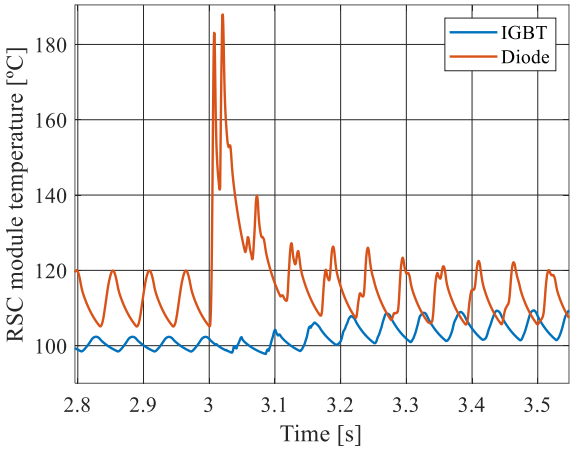

Figure 4.10 – Junction temperature of the RSC module during a 20% balanced voltage sag without RTFC strategies.

Figure 4.9 and Figure 4.10 demonstrate the adverse effects of oscillations stemming from voltage sags, which are evident in the temperature variations of power modules. The differences in semiconductor component behaviors are evident between the GSC and RSC configurations. Noticeably, under normal operating conditions, the IGBT undergoes the highest thermal stress in GSC, while in RSC, the diode is the most thermally stressed component. This discrepancy arises from the direction of power flow: AC to DC for RSC and vice versa for GSC. In particular, when analyzing Figure 4.9, an increase in diode junction temperature is observed at the start of the sag due to simultaneous peaks in the DC bus voltage and GSC currents. The behavior of these variables exhibits a more gradual change as the temperature dynamics are considerably slower compared to current dynamics.

An important observation is the heightened susceptibility of RSC to these effects, as oscillations induce overcurrents in the rotor, leading to peaks in the junction temperature of semiconductor devices that exceed the maximum temperature supported (175 ºC) as seen in Figure 4.10. Another factor contributing to the temperature peak is evident when examining Figure 4.5, where it can be observed that the current surpasses the maximum repetitive peak current specified in the module datasheet (3000 A).

Furthermore, it is evident that the thermal cycling endured by components within the power modules of RSC is lower compared to those in the GSC. This difference arises from the extended exposure of devices to high temperatures in the RSC due to the lower frequency of currents (approximately 18 Hz for 2340 rpm) in contrast to GSC's frequency of 60 Hz.

It is crucial to emphasize that the junction temperatures of the semiconductor devices, during normal operation, did not surpass the temperature limit supported by the power module, which stands at a maximum of 175ºC. Thus, the thermal design presented in the previous chapter and the current oversizing design used ensures the system's safe operation.

The capability to supply reactive power to the grid during a voltage sag is regulated by grid codes. This feature is crucial as it facilitates voltage support by injecting a positive-sequence reactive current, thereby aiding in stabilizing the grid voltage levels during such events.

Under the aforementioned operating conditions, the system underwent simulation to comply with the requirements outlined in the Brazilian grid code. As a result, the active power was systematically reduced while an equivalent reactive current was injected into the system at the same rate.

Figure 4.11 shows de ABC rotor currents, while Figure 4.12 depicts the rotor currents in synchronous reference frame. In comparison to the previous test, regarding the values reached by the currents during the start of the sag, there is no difference. This is because the natural component remains unchanged, as no RTFC strategy is employed in this test, similar to the previous one. The reduction in active power during the voltage sag contributes to lowering the average temperature of power semiconductors after the natural component main transient, as depicted in Figure 4.13. Notably, the temperature peak observed at the beginning of the sag also exhibits no difference from that shown in the previous test (Figure 4.10), given that the natural component remains uncontrolled.

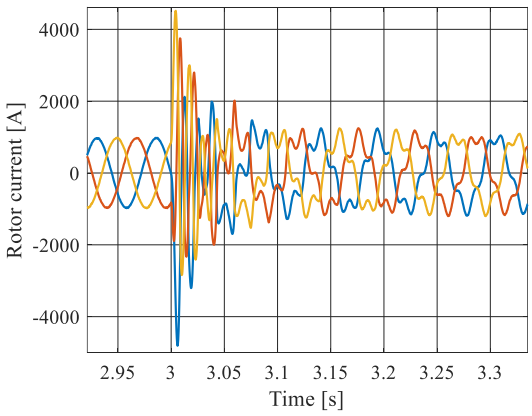

Figure 4.11 - ABC rotor currents during a 20% balanced voltage sag.

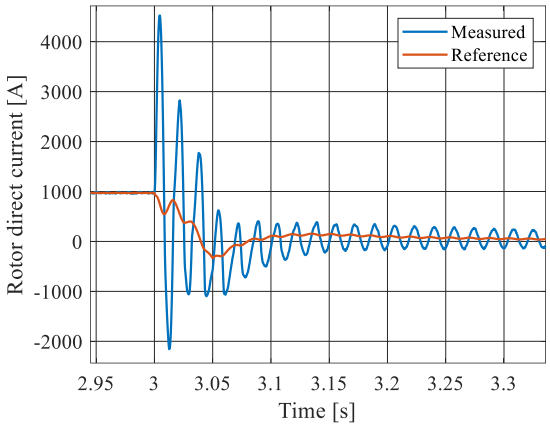

(a)

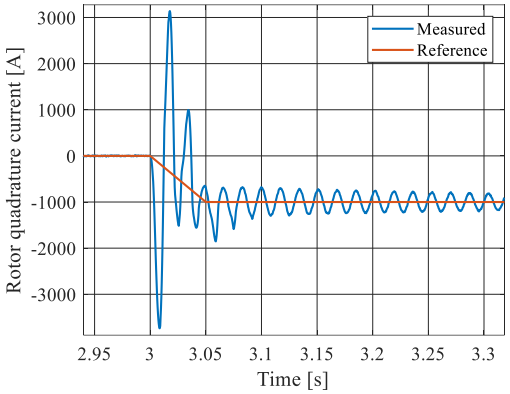

(b)

Figure 4.12 - RSC currents during a 20% balanced voltage sag: (a) direct axis and (b) quadrature axis.

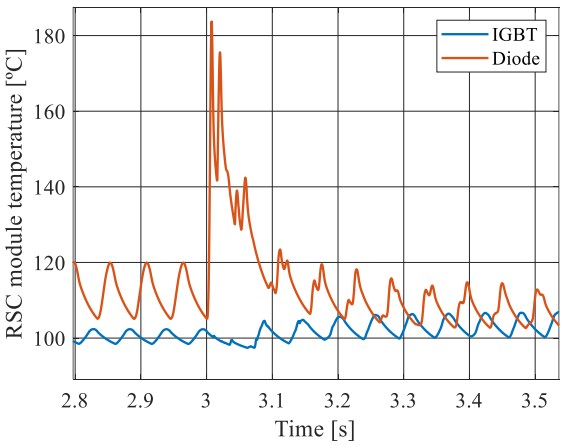

Figure 4.13 - Junction temperature of the RSC module during a 20% balanced voltage sag.

4.1.2. MCC strategy

Once we grasp the detrimental impact of voltage sags on DFIG converters, it becomes imperative to comprehend the system's behavior when employing RTFC strategies. To begin this exploration, we first delve into the analysis of the MCC strategy.

A simulation was conducted under nominal conditions, maintaining the machine speed at 2340 RPM. At 2.0s into the simulation, a voltage sag occurs, decreasing the stator voltage to 20% of its nominal value. Figure 4.14 shows two stator flux waveforms: one without the use of MCC strategy and the other with the MCC implemented for a proportional gain k_{pim}=-20.

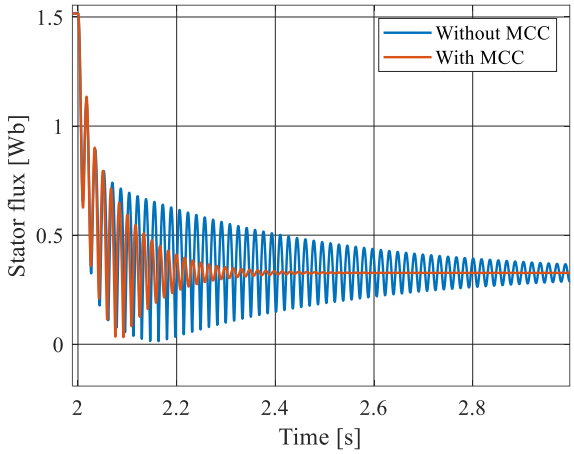

Figure 4.14 – Stator flux linkage.

The observation highlights the strategy capability to enhance the damping of the natural component within the stator flux linkage, thus validating the effectiveness of this control technique. Figure 4.15 provides insights into the behavior of the time of decay of the stator flux, demonstrating how the damping increases (smaller time) with variations in the proportional gain of the magnetizing current loop. It is important to note that to generate this curve, the time taken for the stator flux to decay from its maximum value to 10% of this value was considered for each value of k_{pim}. A dedicated simulation was conducted for each gain, and the collective outcomes were synthesized to form the representation depicted in Figure 4.15.

Figure 4.15 illustrates a noticeable trend: the damping of the stator flux experiences a substantial increase with lower k_{pim} values. However, as the gain increases, the damping tends to stabilize, showing minimal variations.

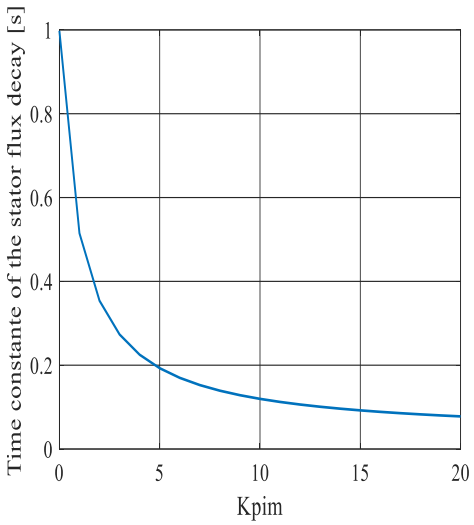

Figure 4.15 – Time constant of the stator flux decay for different kpim values.

A pertinent inquiry arises regarding the impact of MCC on the system, particularly on the power semiconductor devices. To explore this, simulations were conducted, varying the proportional gain k_{pim} and the dip, considering three pairs of the DFIG shaft speed and power: subsynchronous (1260 rpm/0.25 MW), synchronous (1800 rpm/0.85 MW), and supersynchronous (2340 rpm/2.0 MW) cases. Figure 4.16 depicts the curves showcasing the maximum amplitude of rotor current during the sag for these scenarios.

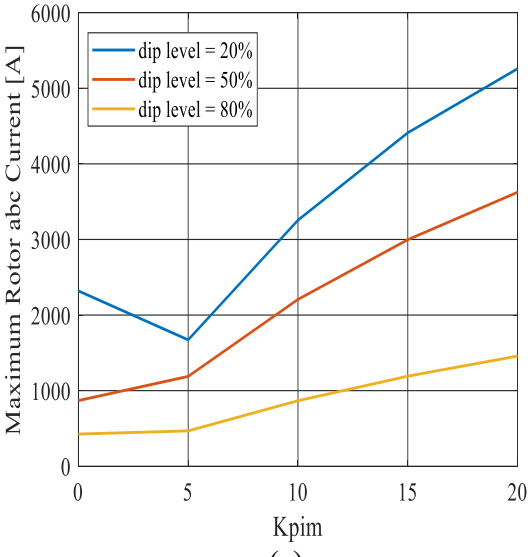

(a)

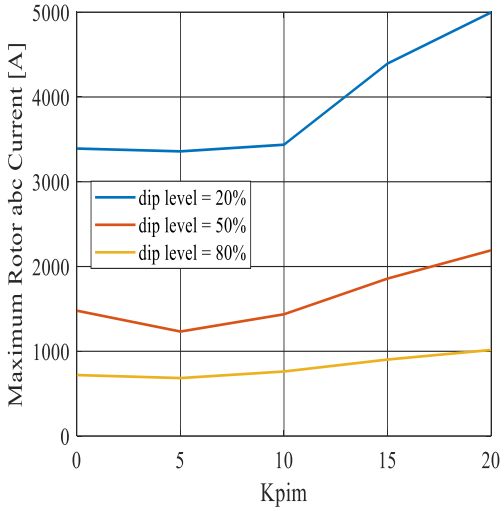

(b)

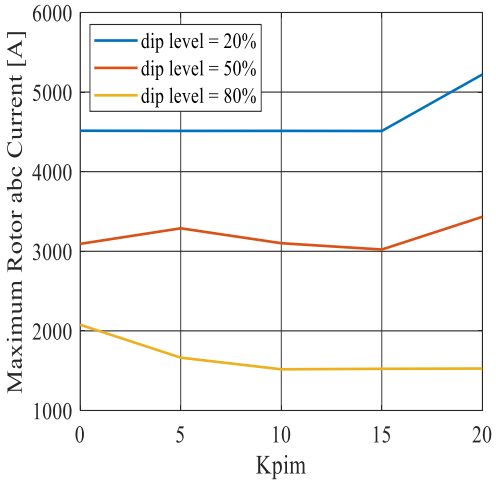

(c)

Figure 4.16 – Maximum rotor current for different k_{pim} values: (a) subsynchronous speed at 0.85 MW, (b) synchronous speed at 0.25 MW, and (c) supersynchronous speed at 2.0 MW.

Upon examining Figure 4.16, a notable observation emerges: the highest amplitude values of the rotor current manifest in the supersynchronous case, attributed to its higher power operation. Additionally, the rotor current increases within a specific range of magnetizing gain k_{pim}. Moreover, it is evident that as the percentage of voltage sag increases, the amplitude of the rotor current also does proportionally.

The dependency of the rotor current on both the magnetizing gain and the level of sag exhibits distinct behaviors across various operational regimes and dip levels. Notably, a peculiar pattern surfaces in the synchronous and supersynchronous cases. Specifically for the curve corresponding to the 20% dip, the rotor current remains constant for values of k_{pim} below approximately 10. This phenomenon can be elucidated by the predominance

of the direct axis rotor current over the quadrature axis rotor current under such conditions. However, when this dominance shifts, an upsurge in the rotor current amplitude is witnessed with an increase in the magnetizing gain. This impact of the quadrature rotor current is more evident in the subsynchronous case, where the rotor currents increase across the entire range of k_{pim} gain and almost proportional to this gain. Comparing the Figure 4.16 (a), (b), and (c) an important observation emerges: the maximum rotor current remains nearly constant for a severe voltage sag (20%) when high values of k_{pim} are applied, irrespective of the rotor speed imposed on the machine. This behavior occurs because the response is dominated by the quadrature current, and the operation power (related to the direct current) has smaller influence.

Figure 4.17 depicts the maximum junction temperature achieved by the semiconductors during the voltage sag.

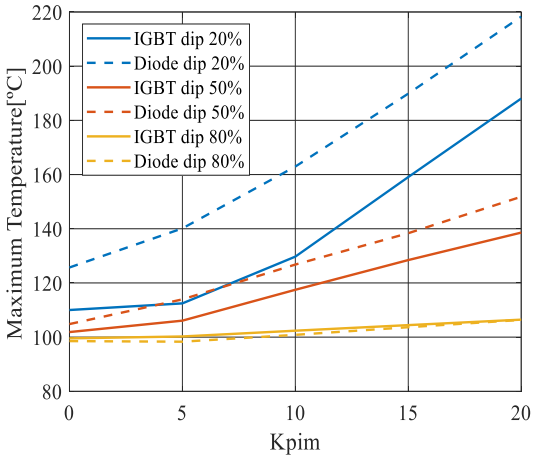

(a)

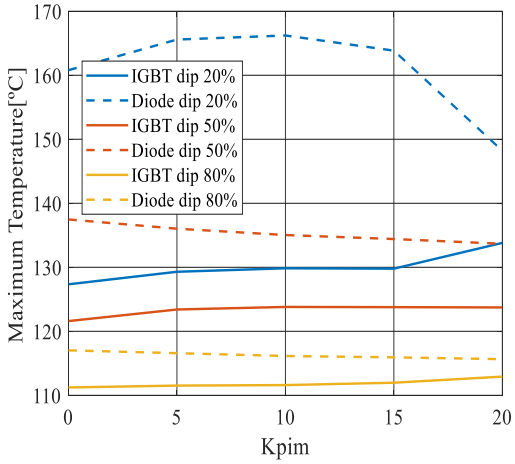

(b)

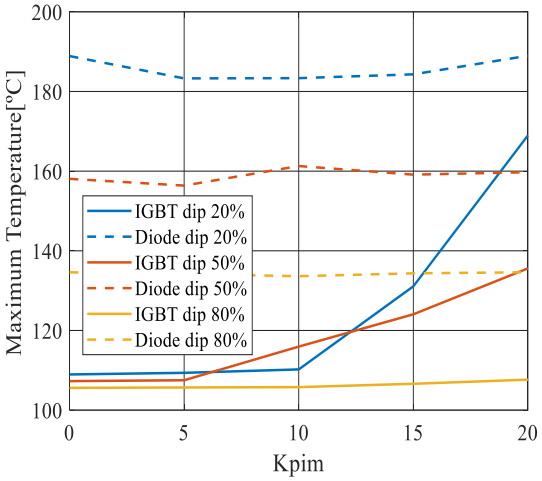

(c)

Figure 4.17 – Maximum junction temperature for different kpim values: (a) subsynchonous speed at 0.85 MW. (b) synchronous speed at 0.25 MW and (c) supersynchronous speed at 2.0 MW.

The introduction of the magnetizing current control loop indeed amplifies the thermal stress experienced by the power module. Nevertheless, this behavior diverges based on the operational regime of the system. In the subsynchronous operation, increasing k_{pim} results in heightened stress on both the IGBT and diode across all sag levels. Notably, the stress is higher for the curve associated with a 20% dip. This escalation occurs due to the direct correlation between the voltage drop and the induced voltages in the machine rotor by the natural component of the stator flux, since more intense voltage sags yield to increased rotor voltage, consequently higher rotor currents.

In the scenario of the system operating in synchronous mode, the MCC demonstrates a diminished impact on temperature in contrast to the other operational cases. In this mode, with zero slip, there is no induced voltage in the rotor during normal operation. Consequently, during the sag, only the natural component of the flux prevails, so the rotor currents has the same frequency as this one (60 Hz). Here, the MCC aims at dampening the oscillation, averting sharp peaks in the device junction temperatures and effectively reducing thermal cycling as well.

The reason behind this phenomenon lies in the initial phase of the voltage dip, where a shift occurs in the power flow dynamics. As the voltage drops, the machine rotor transitions from injecting active power to absorbing it. This causes a reversal in power flow direction—from the DC side to the AC side—implying additional stresses on the IGBTs. Moreover, this stress increases proportionally with the severity of the voltage dip.

Consequently, the more substantial the drop in stator voltage, the greater the peril posed by the voltage sag to the system.

Interestingly, these observations suggest that the MCC strategy might not prove beneficial for the subsynchronous case. This assertion stems from the observed trend: the maximum temperature experienced by the devices increases alongside the increment in k_{pim}, indicating a potential counterproductive effect of the MCC strategy in this specific operational scenario. In the synchronous speed operation, the MCC emerges as an intriguing strategy. Across variations in k_{pim}, it shows minimal influence on the temperature rise of the devices. Notably, for more severe sags and k_{pim} values exceeding 15, there's a discernible decline in the maximum peak temperature experienced by the diode. This particular analysis suggests that the strategy, besides dampening oscillations from the natural component, might contribute to reducing the maximum temperature experienced by the component at the onset of the dip.

In the supersynchronous case, especially when examining the more severe sag (20% dip curve), the selection of k_{pim} remarkably impacts the device temperatures. Notably, for values exceeding 0 but remaining below 10, there is minimal variation observed in the maximum device temperatures. This underscores the applicability of MCC in this range of k_{pim}, showcasing a notable reduction in the natural component, as depicted in Figure 4.15. Above the threshold of 10 for k_{pim}, the strategy's efficacy shifts, leading to an escalation in the thermal stress experienced by the devices. This increase is notable in the IGBT temperature, demonstrating a more pronounced trend. The saturation observed in the decay of the natural component (as shown in Figure 4.15) from this range of k_{pim} values indicates that the strategy ceases to provide any discernible benefits to the system.

Choosing the MCC gain involves striking a balance to minimize the impact on the rotor currents and the semiconductor junction temperatures while effectively reducing the decay of the stator flux. Upon analyzing Figure 4.15, Figure 4.16c and Figure 4.17c, it is apparent that k_{pim}=10 stands out as an "optimal gain" that satisfactorily addresses all these concerns.

4.1.2.1. Effect of modifying the DC-link voltage

Supplementary tests were conducted, expanding the converter limits and explore the behavior of crucial system variables. In this way, the DC-link voltage was increased to approximately 1000 V, aiming to offer a more substantial voltage margin for the converter control. It is worth noting that manufacturers typically recommend a module capable of standing a voltage approximately 60% of the DC-link voltage. Henceforth, it becomes imperative to replace the power module previously utilized with model FF1500R17IP5P (Infineon, 2020), which has a higher collector-emitter voltage of 1700 V. Details regarding the module can be found Table 4.1, while the circuit diagram remains identical to the one depicted in Figure 3.23.

Table 4.1 – FF1500R17IP5P module information.

Parameter	Value
Collector-emitter voltage	1700 V
Continuous DC collector current	1500 A
Peak repetitive collector current	3000 A
Maximum junction temperature	175 °C

For the tests in this section, only the supersynchronous case is analyzed, considering that it represents the most severe scenario.

The augmented voltage capacity of the converter contributes notably to curtailing overcurrents, as evident in Figure 4.18. This increase in voltage margin in converter control effectively prevents voltage saturation, thereby averting the flow of excessive currents through the rotor during a sag. The selection of k_{pim} is intrinsically associated with the reduction in maximum rotor current. Specifically, within the range of values from 0 to 15, the maximum current experienced by the rotor decreases in comparison to Figure 4.16(c). However, beyond these values, a convergence in the behavior of the cases emerges, wherein the influence exerted by the magnetizing loop amplifies, consequently leading to an upsurge in rotor current.

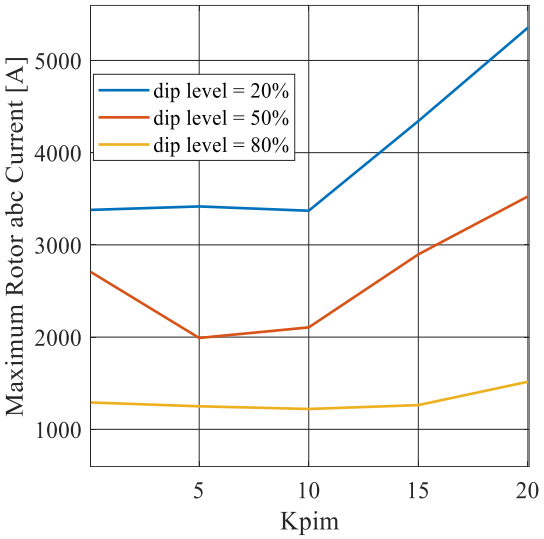

Figure 4.18 – Maximum rotor currents for case of increased DC-link voltage at supersynchronous speed - 2.0 MW.

Figure 4.19 shows the maximum junction temperature of the semiconductor devices, highlighting the correlation between the dip level and the magnetizing gain. Comparing it with Figure 4.17 (c), a similarity in the behavior of the maximum temperature curves for these two cases is evident. However, in this instance, the maximum temperature reached by the semiconductor devices is slightly lower. This decrease is due to the decrease in rotor overcurrents, directly influencing the maximum temperatures experienced by the devices.

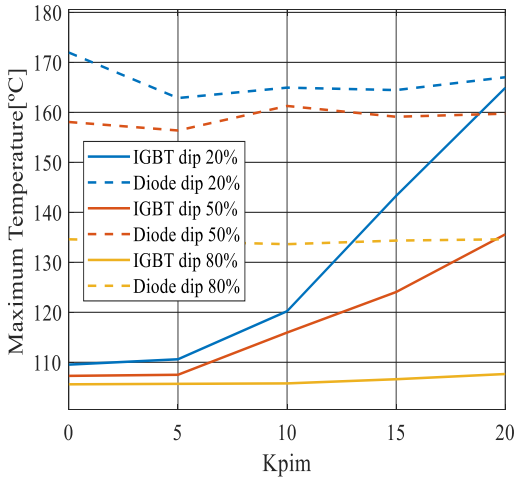

Figure 4.19 – Maximum junction temperature for case of increased DC-link voltage at the supersynchronous speed - 2.0 MW.

Figure 4.20(a) denotes that increasing the DC-link voltage results in a decrease in the damping effect on the natural component of the stator flux. This issue arises from the increased oscillation observed in the natural component of the stator flux. For instance, with k_{pim} = 5, the test conducted with a DC-link voltage of 689 V, depicted in Figure 4.20 (b), demonstrates a damping to around 20% of the time constant of the stator flux. Conversely, the test performed with a higher DC-link voltage (1000 V), shown in Figure 4.20 (a) showcases a damping of approximately 65%. It is important to note that the methodology employed to obtain Figure 4.20 (b) was replicated for Figure 4.20(a).

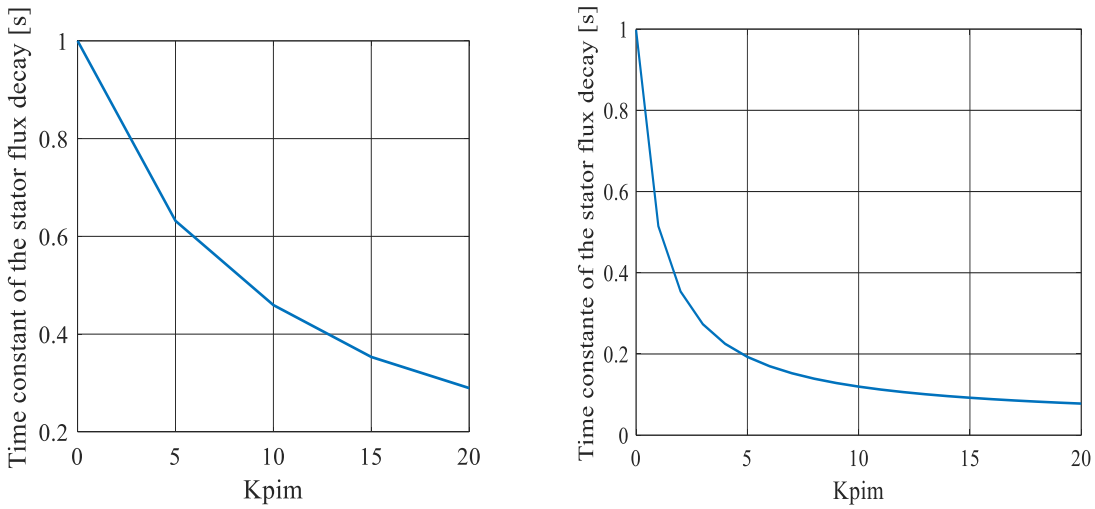

(a) (b)

Figure 4.20 – Stator time constant decay for case of increased DC-link voltage for: (a) 1000 V and (b) 698 V.

In this test, the impact of increasing the DC-link voltage on the rotor currents and semiconductor device junction temperatures under balanced voltage sags while employing the RTFC strategy (MCC) was analyzed. The benefit of this voltage increase lies in decreasing the maximum rotor current, consequently reducing the maximum junction temperature of the devices. However, this increase in the DC-link voltage amplifies the oscillation induced by the natural component of the stator flux, thereby compromising the effectiveness of MCC action. As previously discussed, this oscillation detrimentally affects the grid power quality. Hence, as the decrease in the junction temperature is not so expressive, in the subsequent subsections, the DC-link voltage will be set to its nominal value (698 V) as employed previously.

4.1.2.2. MCC results using the “optimal gain”

For the analysis of the system's primary variables, k_{pim} = -10 has been selected in this section. This particular gain strikes a favorable balance by effectively reducing the natural component of the stator flux while exerting minimal impact on rotor currents and power semiconductor junction temperatures, as previously demonstrated. This analysis will encompass the base case (DC-link voltage set at 698 V) and will specifically focus on the worst-case scenario: operation at the supersynchronous speed with a 20% voltage sag.

Figure 4.21 (a) illustrates the stator active power and the operation of the power control loop. At the onset of the dip, there is a prompt reduction in the stator active power at a predefined rate, prioritizing the injection of reactive current into the grid in alignment with the specifications outlined in the Brazilian grid codes. Notably, the control mechanism exhibits an adept response in maintaining controlled average active power levels.

Figure 4.21 (b) depicts the stator reactive power, highlighting the injection of reactive current into the grid. The negative signal observed in the reactive power during the sag denotes the reactive current supplied to the grid as stipulated by the Brazilian grid code. It is noteworthy that the reactive power reference is not displayed because, during the voltage sag, the focus remains primarily on controlling the reactive current (quadrature component) rather than the reactive power itself.

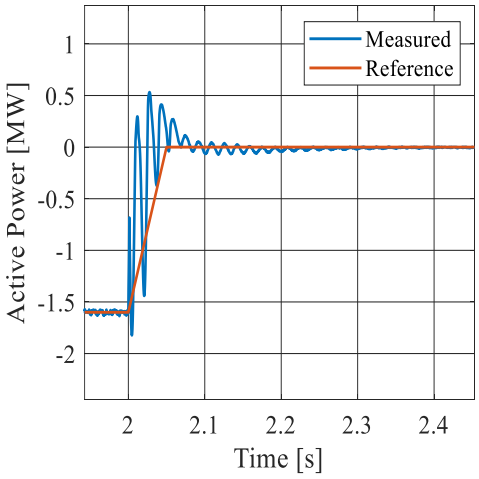

(a)

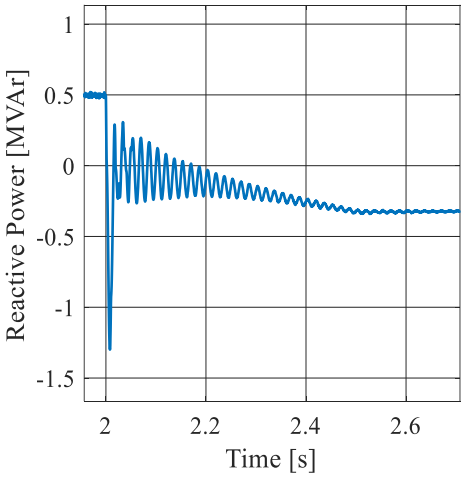

(b)

Figure 4.21 – Stator powers during a 20% balanced voltage sag with kpim = -10: (a) active power and (b) reactive power

Figure 4.22 presents the ABC rotor currents, while Figure 4.23 (a) shows the d-axis current and Figure 4.23 (b) illustrates the q-axis current. The action of the MCC on the quadrature current is noticeable, whereas the control system tracks the reference and effectively regulates the current.

Figure 4.24 provides insight into the junction temperatures of the modules associated with the RSC. This plot clearly shows how this behavior translates into the thermal stress experienced by semiconductor devices.

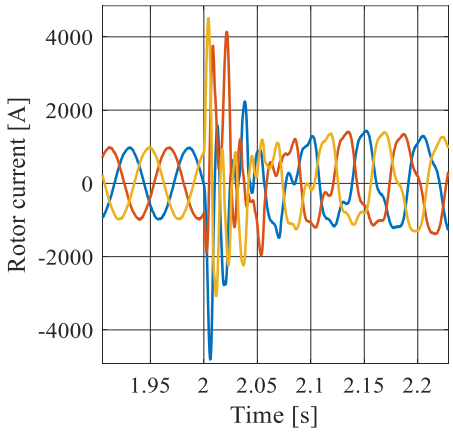

Figure 4.22 – Rotor currents in abc coordinates during a 20% balanced voltage sag with k_{pim} = -10.

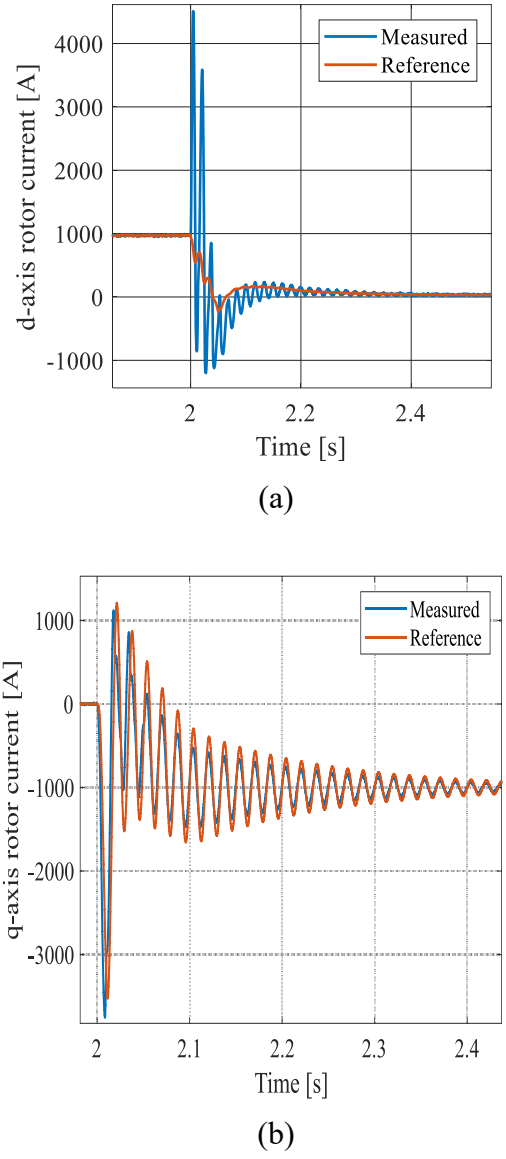

Figure 4.23 – Rotor currents in the dq reference frame during a 20% balanced voltage sag with k_{pim} = -10: (a) d-axis component and (b) q-axis componente.

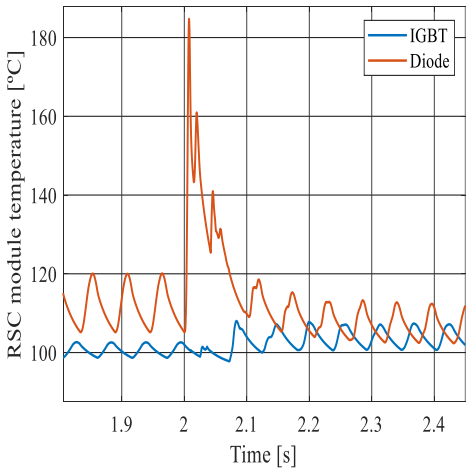

Figure 4.24 – Module junction temperature during a 20% balanced voltage sag with k_{pim} = -10.

As expected, the MCC strategy notably aided in mitigating oscillations induced by the natural component of the stator flux. This effect is evident when examining the rotor current graphs in Figure 4.5, notably in the quadrature current, which showcases a significant reduction of approximately 67% in the initial peak current experienced at the commencement of the sag. This reduction can be attributed to the operation of the magnetizing current that acts on the reactive current (quadrature component). However, it is important to note that while the control action effectively addresses these oscillations, it does impact the thermal stresses experienced by the semiconductors, as depicted in Figure 4.24.

The converter design ensures, under system's normal operation conditions, that the maximum temperature stays below the maximum of threshold 175 ºC, thus ensuring the safe operation in normal conditions. This means that the MCC is a reliable control approach.

4.1.3. FSCR strategy

The FSCR strategy was tested similarly to the MCC strategy to observe the system's most pertinent variables and the thermal behavior of power semiconductors. This strategy revolves around employing the measured stator currents as a reference for controlling the RSC when the system undergoes a voltage sag.

In this test, the base case was revisited: the system operating at supersynchronous speed with a balanced 20% voltage sag. As a result, Figure 4.26 depicts the stator flux. The rotor currents in ABC coordinates are represented in Figure 4.26, whereas Figure 4.27 illustrates the rotor currents in the synchronous reference frame.

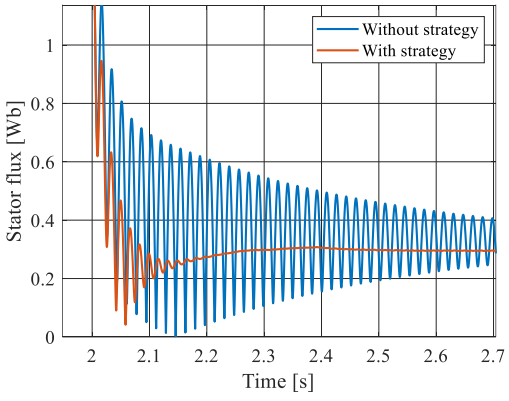

Figure 4.25 - Stator flux for a balanced voltage sag of 20%.

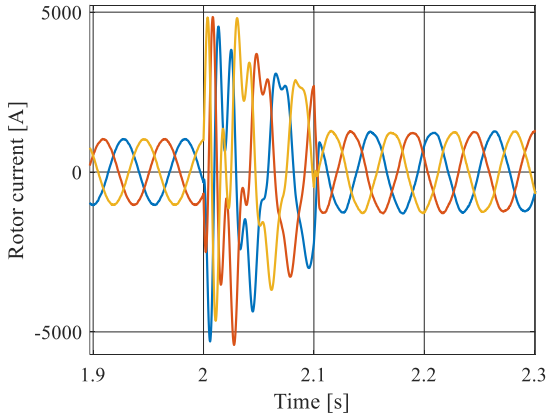

Figure 4.26 - Rotor currents for a balanced voltage sag of 20%.

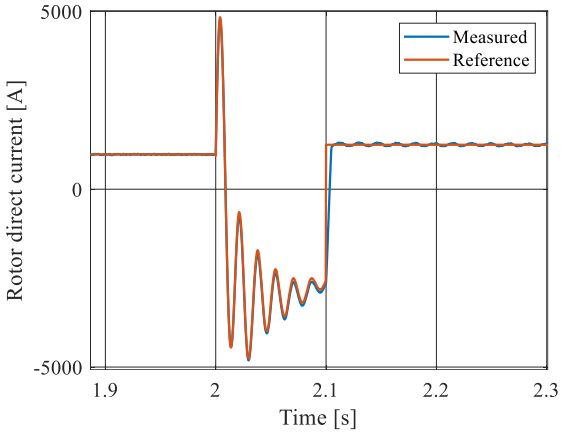

(a)

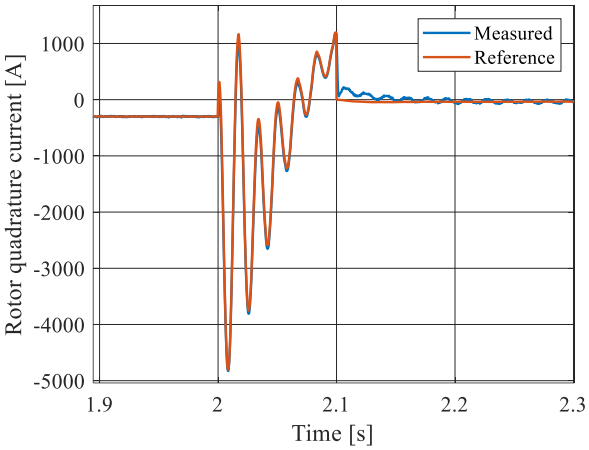

(b)

Figure 4.27 - Rotor currents in synchronous reference frame for a balanced voltage sag of 20%: (a) d-axis component and (b) q-axis component.

Observing Figure 4.25, the strategy's impact on reducing stator flux oscillations becomes apparent. The transient behavior of the natural component ceases approximately 100 ms after the sag onset. At this point, the strategy is deactivated and the classical control is activated. This flux oscillation reduction comes with a significant tradeoff: an evident increase in rotor currents, as depicted in Figure 4.26 and Figure 4.27. This issue directly influences the junction temperatures of power semiconductors according to Figure 4.28.

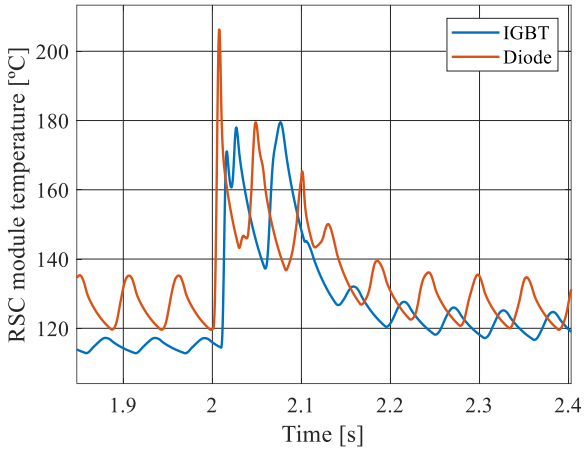

Figure 4.28 - Temperature of the semiconductors devices of the RSC module for a balanced voltage sag of 20%.

Therefore, one can conclude that such a strategy allows for the reduction of the stator flux oscillations. Conversely, this results in heightened thermal stress on the power semiconductors, wherein the maximum value reached at the onset of the sag surpasses the module's maximum temperature threshold (175 ºC). Therefore, it is necessary is to redesign of the converter for the accurate application of such strategy in this conditions, which is not within the scope of this work.

4.1.4. CRTC strategy

A simulation test was carried out to assess the impact of the CRTC strategy on the system, particularly in terms of thermal stress on the power semiconductors.

In this test, a 20% balanced voltage sag is considered, and the tracking coefficient k_r was systematically changed to analyze its impact on the temperature of the semiconductor components. The strategy relies on employing the measured stator

currents multiplied by the gain k_r as a reference for controlling the RSC, similar to the FSCR strategy described in Subsection 3.3.3.

Initially, the behaviors of key variables within the system, such as the rotor voltage, rotor current, and stator flux will be presented. Figure 4.29 illustrates the variation in the time constant of the stator flux decay with the adjustment of k_r, marking the onset of the sag.

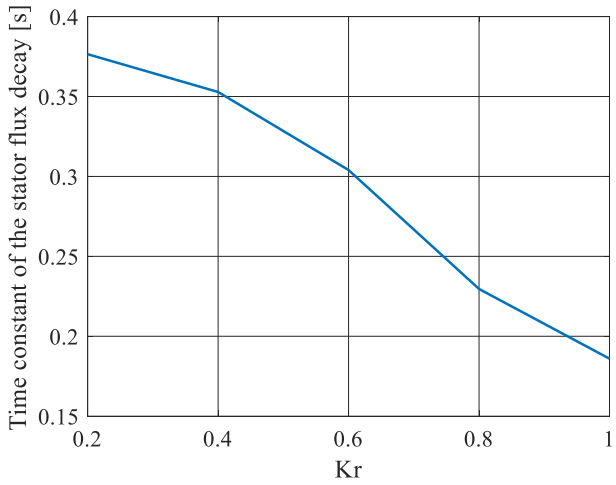

Figure 4.29 – The time of decay of the stator flux for a varying in the tracking coefficient kr.

Examining Figure 4.29 reveals a discernible trend: as the coefficient k_r increases, there is a decrease in the time of decay of the stator flux natural component. This observation was derived from the data captured at the moment when the stator flux reached 100 ms subsequent to the initiation of the dip. Consequently, it can be inferred that k_r significantly impacts the decay of the natural component of the stator flux.

The distinction in behavior becomes more apparent upon analyzing the stator flux for two distinct values of k_r. To ascertain the most appropriate values, we refer to equation (3.80) and equation (3.81), which delineate the limitations on k_r values, factoring in the maximum permissible current within the RSC and the maximum DC-link voltage. Upon calculation, we ascertain a current restraint of $k_r \leq 1.034$ and a voltage restraint of $0.957 \leq k_r \leq 0.974$. Therefore, we selected one value that lies outside the constraints: k_r = 0.6, and another value within the constraints: k_r = 0.96. Figure 4.30 depicts the stator flux corresponding to two values of k_r.

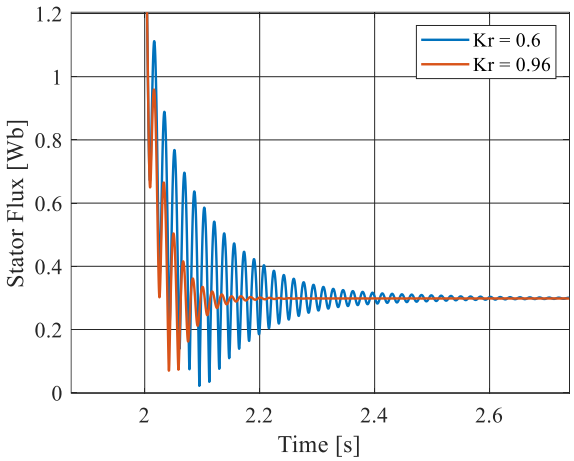

Figure 4.30 - Stator flux for two values of the tracking coefficient k_r.

The difference between the curves is notably apparent. When k_r adheres to a value within the constraints, there is a marked decrease in the natural component of the stator flux. Nevertheless, it is crucial to examine the behavior of both rotor and stator currents concerning these specific values of k_r. Figure 4.31 exhibits the stator and rotor currents for a k_r value of 0.6, while Figure 4.32 illustrates these currents for k_r = 0.96.

Selecting values of k_r below these constraint limits results in an inability to adequately control both stator and rotor currents concerning the natural component of the stator flux during the sag. However, as the value of k_r aligns within the constraints, the control mechanism demonstrates greater effectiveness in decreasing the natural component of the stator flux, as depicted in Figure 4.32, but with an increase in the rotor currents, as shown in Figure 4.32.

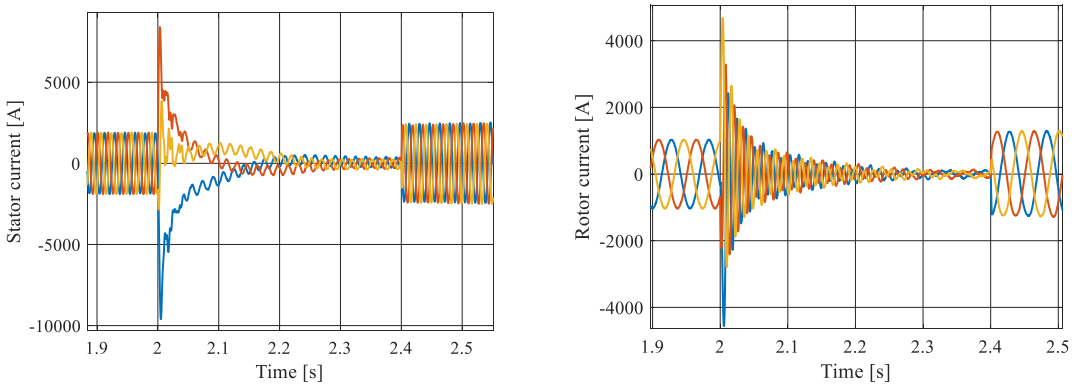

(a) (b)

Figure 4.31 - Currents in abc coordinates for a kr = 0.6: (a) stator and (b) rotor.

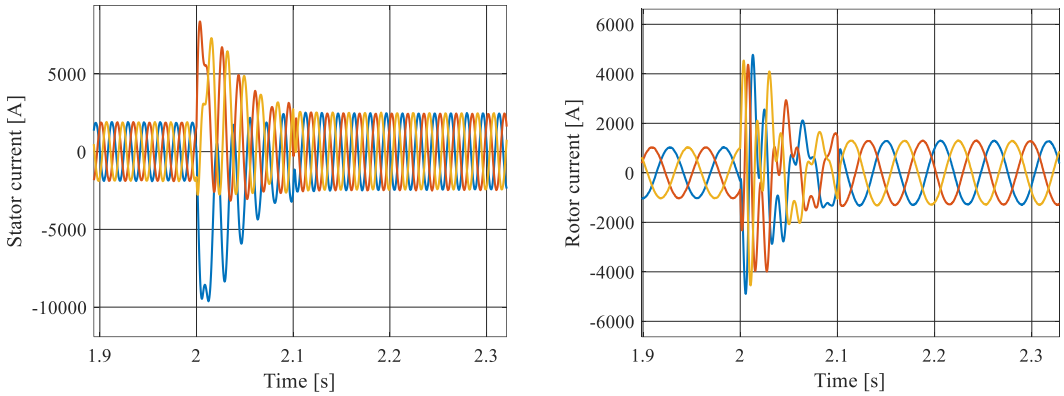

(a) (b)

Figure 4.32 - Currents in abc coordinates for a kr = 0.96: (a) stator and (b) rotor.

The difference becomes clearer when comparing Figure 4.33 and Figure 4.34, which show the currents in the synchronous reference frame for k_r = 0.6 and k_r = 0.96, respectively. Similar to the approach adopted with the FSCR strategy, once the transient of the natural component of the stator flux concludes, the strategy is deactivated, and classical control is activated. This transient period varies for different values of k_r, occurring approximately 400 ms after the onset of the sag for k_r = 0.6 and within 100 ms for k_r = 0.96, as depicted in Figure 4.30.

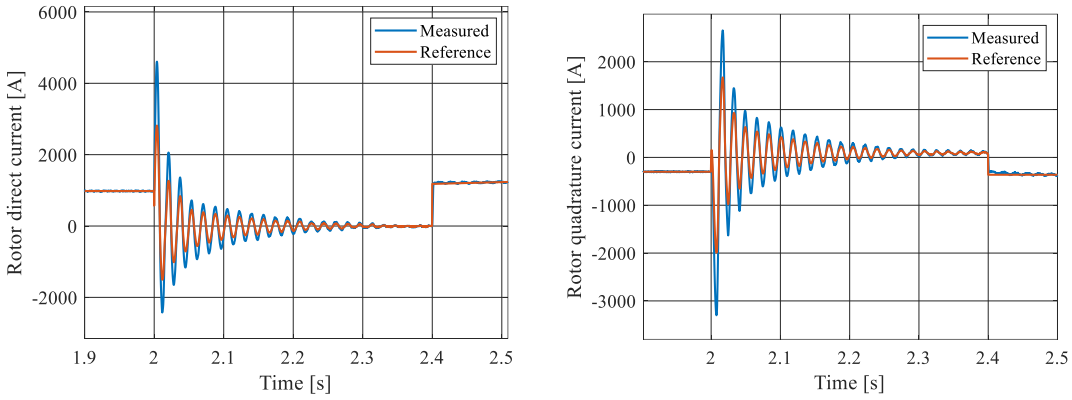

(a) (b)

Figure 4.33 - Rotor currents in synchronous reference frame for a k_r = 0.6: (a) d-axis and (b) q-axis.

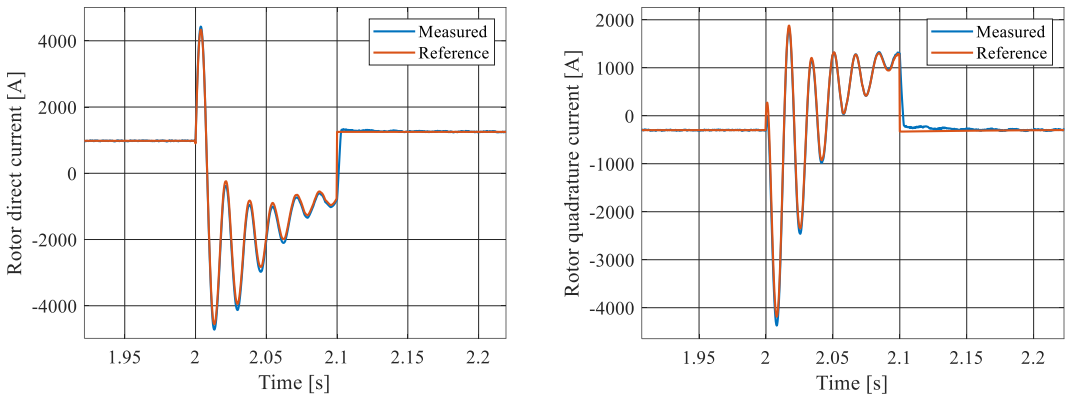

(a) (b)

Figure 4.34 - Rotor currents in synchronous reference frame for a kr = 0.96: (a) d-axis and (b) q-axis.

These outcomes find validation when examining the behavior showcased in Figure 4.35 for the maximum rotor voltage and in Figure 4.36 for the maximum rotor current. Upon analyzing the maximum rotor voltage, it is seen that values of k_r within the range of 0.2 to 0.8 result in the rotor voltage exceeding levels beyond the converter's synthesis capacity (approximately 400 V). This situation prompts the converter to operate in overmodulation, consequently saturating the controller. However, when k_r falls within the range of 0.8 to 1.0, there is a notable augmentation in the maximum rotor current. This augmentation directly contributes to elevating the temperature of the power semiconductors, as depicted in Figure 4.37.

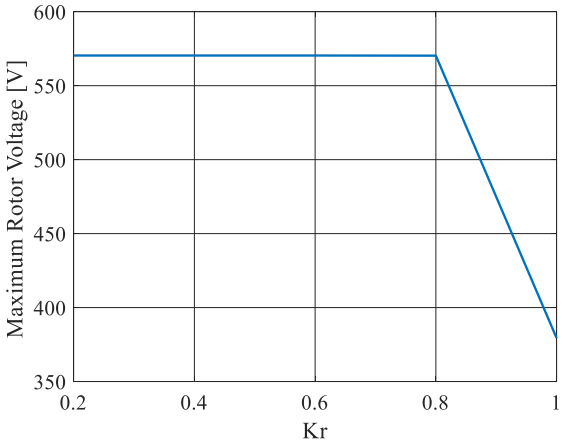

Figure 4.35 - Maximum rotor voltage for a varying in the tracking coefficient kr.

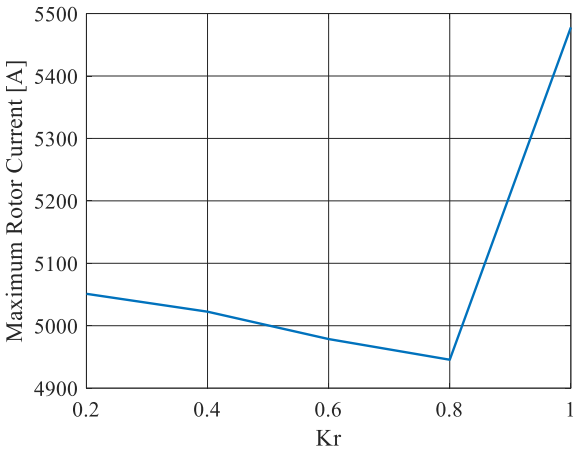

Figure 4.36 - Maximum rotor current for a varying in the tracking coefficient kr.

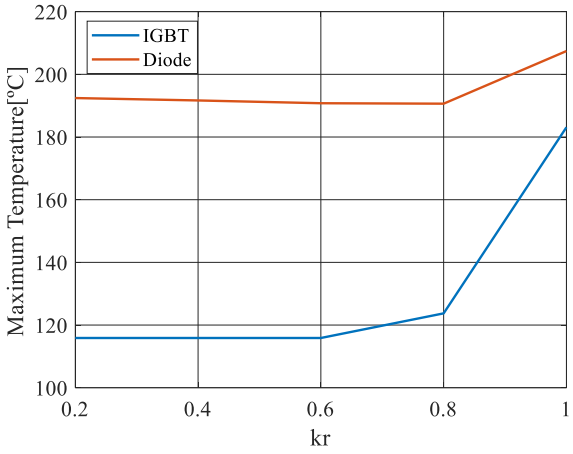

Figure 4.37 - Maximum temperature of the power semiconductors for a varying in the tracking coefficient kr.

It is important to highlight that for k_r = 1, this strategy resembles the FSCR strategy, with the values associated to this gain for maximum current and maximum temperature corresponding to those depicted in Figure 4.27 and Figure 4.28, respectively.

Figure 4.38 depicts a predominance of the natural component of the stator flux, resulting in an elevation of the diode's temperature, the most stressed component in this scenario. Following this, within a few milliseconds, there is a subsequent decline in this temperature. This reduction aligns with the decrease in the rotor current reference in Figure 4.33 and Figure 4.34.

Hence, it becomes evident that achieving a reduction in the natural component requires maintaining k_r within the prescribed current and voltage restriction limits. Consequently, there is a noticeable increase in the temperature of the semiconductor components, as depicted in Figure 4.38 (b). In contrast to the prior observation in Figure

4.38 (a), there is an abrupt increase not only in the diode temperature but also in the IGBT temperature. Furthermore, in this scenario, the temperature remains at high levels during subsequent cycles following the sag. This issue occurs due to the rotor quadrature axis current sustaining a higher value compared to the previous case. As the temperature dynamics operate at a slower pace than the current dynamics, the component takes longer to cool down, even after the current decreases.

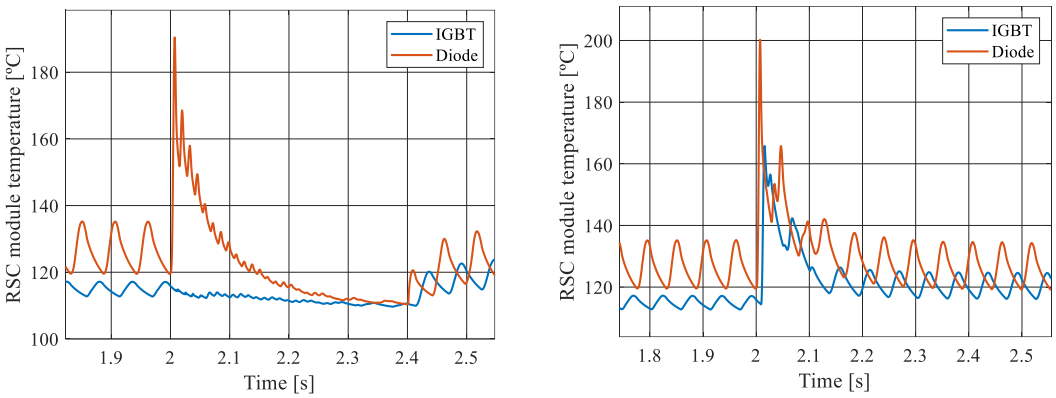

Figure 4.38 - Temperature of the semiconductors devices of the RSC module for: (a) k_r = 0.6 and (b) k_r = 0.96.

4.1.5. RTFC comparison for balanced voltage sags

This subsection presents a comparison among strategies targeting the improvement of the system behavior during balanced voltage sags. It is important to mention that the optimal gain was utilized for strategies employing a gain, determined based on analyses conducted in the preceding subsections for each strategy. Therefore, the MCC strategy used a magnetization loop gain k_{pim} = 10, and the CRTC strategy used a tracking coefficient k_r = 0.96. All tests were conducted under worst-case conditions, with a slip of -0.3 and 2.0 MW of power production.

Figure 4.39 depicts the maximum rotor voltage in the beginning of the sags for the strategies studied in this work. The studied system has a DC-link voltage of 698 V, according to the Table 3.1. As a result, the converter is able to impose a voltage of approximately 400 V.

However, in this test, the converter saturation limits were raised to highlight that, based on the sag's level, the converter might enter into overmodulation. Hence, upon

observing Figure 4.39, how the sag level impacts the maximum rotor voltage. The higher the severity of the sag, the higher the voltage attained by the rotor.

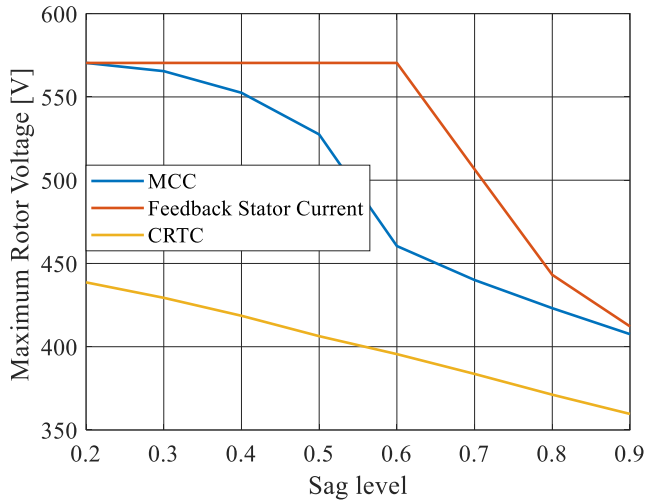

Figure 4.39 - Maximum rotor voltage for the RTFC strategies studied at different sag values.

The big question here is how each control strategy impacts the behavior of the power semiconductor when subjected to voltage sags. Figure 4.40 shows the maximum rotor current, and Figure 4.41 illustrates the maximum junction temperatures of the RSC semiconductors devices.

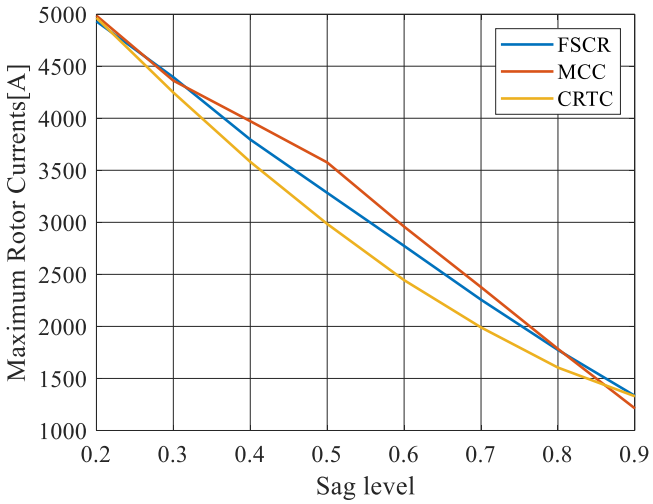

Figure 4.40 – Maximum rotor current for the RTFC strategies studied at different voltage sags values.

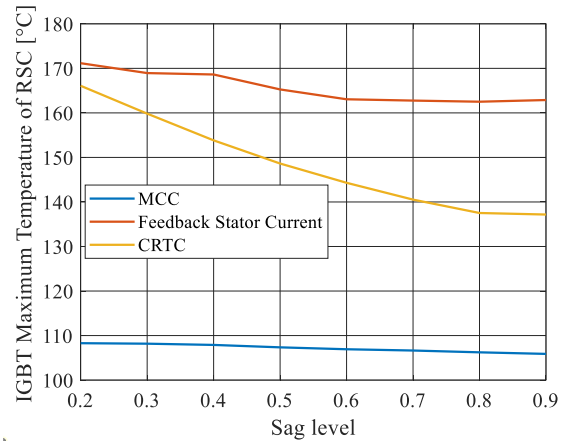

(a)

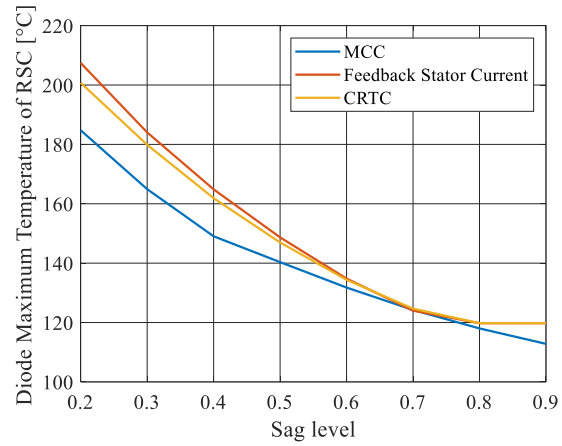

(b)

Figure 4.41 - Maximum junction temperatures of the RSC power semiconductors for the RTFC strategies studied at different voltage sags values: (a) IGBT and (b) diode.

It is noticeable that the CRTC strategy achieves the lowest maximum rotor voltage values. However, it is observed that along with the FSCR strategy, they impose the highest stress on power semiconductors, displaying the highest temperature values that exceed the maximum supported value for the module (175 ºC) when the system is subjected to more severe voltage sags.

The MCC strategy exhibits the most favorable response concerning the thermal behavior of the semiconductors since it does not deactivate active and reactive power controls, as observed in CRTC and FSCR. Consequently, during the sag, it allows for the supplying reactive current to support the system's operation. In dealing with more severe sags, it is necessary to provide an extended margin for the control system to reduce the

natural component of the stator flux and minimize the thermal stresses on the power semiconductors.

It is also important to check the power losses in semiconductor devices, as these are directly linked to the thermal stresses caused by these components. Thus, Figure 4.42 shows the average switching losses, average conduction losses, and average total losses of the power semiconductors devices for each RTFC strategy. These losses were obtained considering the beginning of a balanced voltage dip of 20%.

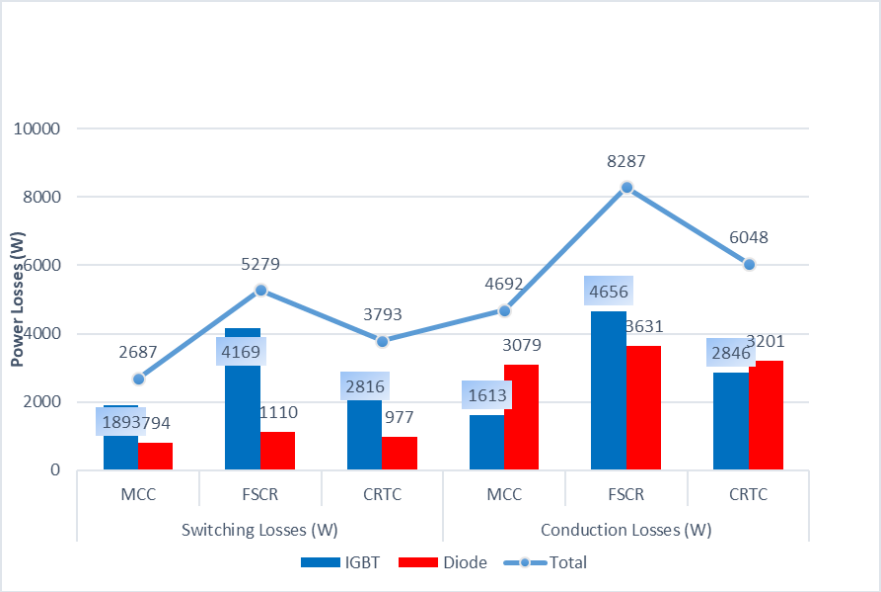

Figure 4.42 - Power losses on the power semiconductors for each RTFC strategies at a 0.2 balanced voltage sag.

It is evident that the FSCR strategy demonstrates the highest total power losses, showcasing the highest temperature in the power semiconductors, as illustrated in the Figure 4.41. The clarity of this results is further heightened upon observing Figure 4.43. This outcome emphasizes the percentage increase in power losses when the system shifts from a steady-state condition to the transient state induced by a voltage sag. The MCC strategy demonstrates the least percentage increase in power losses, succeeded by the CRTC strategy, and ultimately, the FSCR strategy. This substantiates the findings depicted in Figure 4.41.

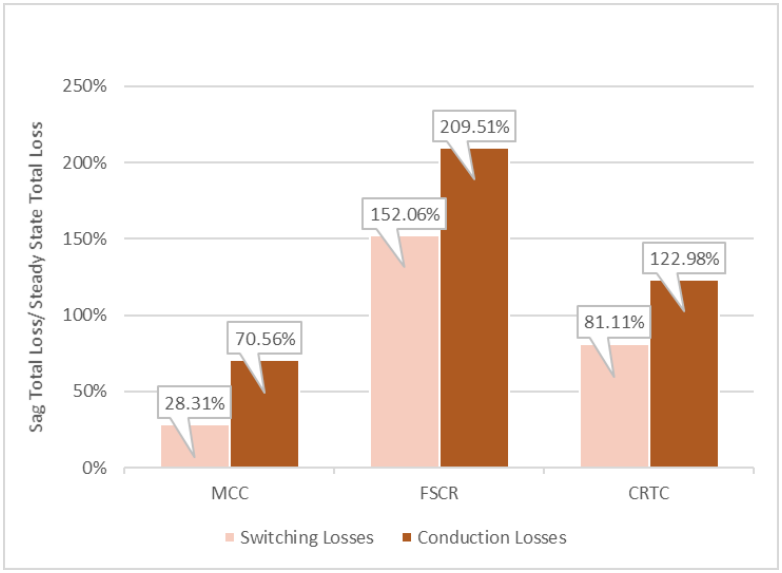

Figure 4.43 - Ratio of total power loss under normal conditions to losses during a 0.2 balanced sag for each RTFC strategy.

Throughout this study, it has been demonstrated and emphasized that examining the thermal behavior of the system is fundamentally crucial to guarantee its safe and reliable operation.

4.2. Unbalanced voltage sags

4.2.1. Classical control

A preliminary test was conducted to explore the behavior of key system variables when subjected to unbalanced voltage sags, using the classical control Specifically, a phase-ground sag was simulated, with phase A reduced to 60% of its nominal value, as illustrated in Figure 4.44. The instant of the voltage sag entry was timed to induce the highest natural component. This test was executed at a supersynchronous speed (2340 rpm), operating at the rated power (2 MW), and without employing any RTFC strategies.

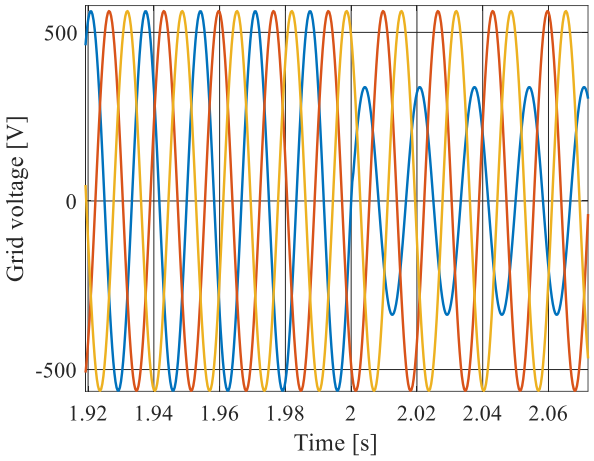

Figure 4.44 – Grid voltage for 60% phase to ground voltage sag.

The stator and rotor currents are depicted in Figure 4.45 and Figure 4.46, respectively. In unbalanced sags, apart from the natural component, there exists a negative sequence that induces oscillations at a frequency twice that of the stator frequency (120 Hz). Similar to balanced sags, conspicuous peaks are observable, resulting from the combination of the natural component and the negative sequence component in both stator and rotor current waveforms. These overcurrents present a potential risk of damaging the converter.

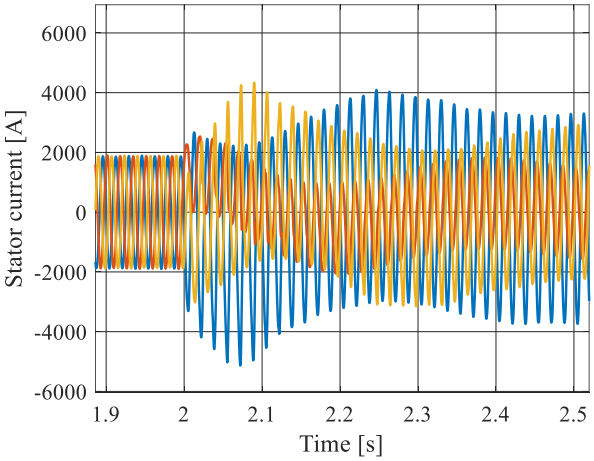

Figure 4.45 – Stator currents for unbalanced voltage sag.

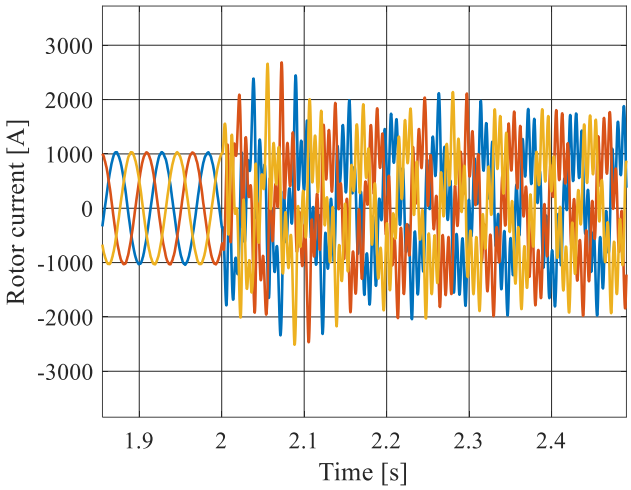

Figure 4.46 – Rotor currents for unbalanced voltage sag.

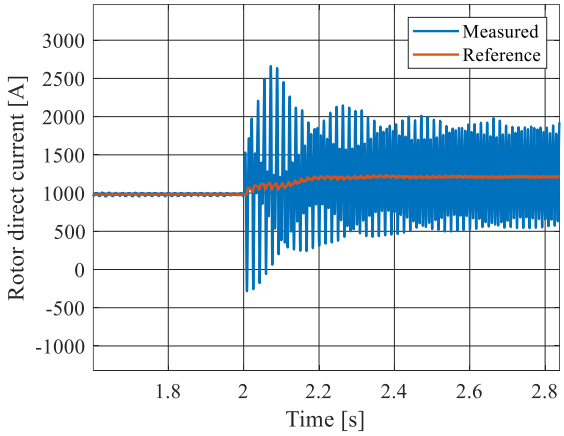

(a)

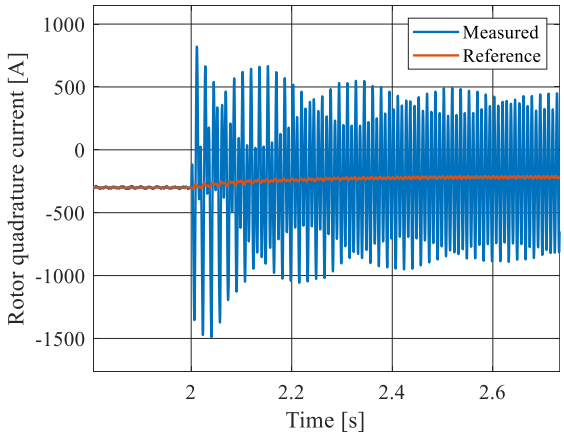

(b)

Figure 4.47 - Rotor currents in coordinate's dq for unbalanced voltage sag: (a) direct axis and (b) quadrature axis.

Examining the rotor currents in synchronous reference (Figure 4.47), one can provide a clearer perspective on the control's efficacy. The natural component gradually decays, leaving only the persistent negative-sequence component throughout the duration of the dip.

The negative sequence component induces oscillations in stator power, evident in Figure 4.48. These oscillations are undesirable, contributing to the degradation of power quality within the system. The GSC currents (Figure 4.49), and DC-link voltage (Figure 4.50) are similarly impacted by the negative sequence, apart from the impacts caused by the natural component, as in the balanced case. Notably, the control system operates solely on the positive sequence, proving ineffective in managing the negative sequence due to the narrow bandwidth set for the controls.

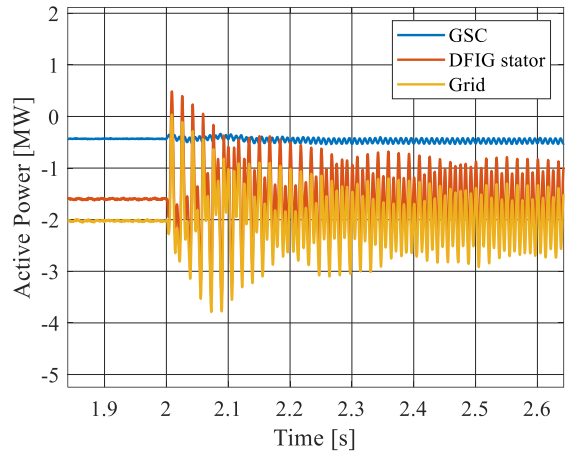

Figure 4.48 – Active powers for unbalanced voltage sag.

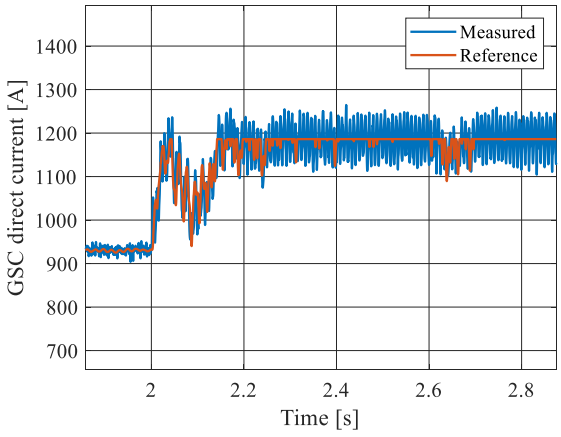

(a)

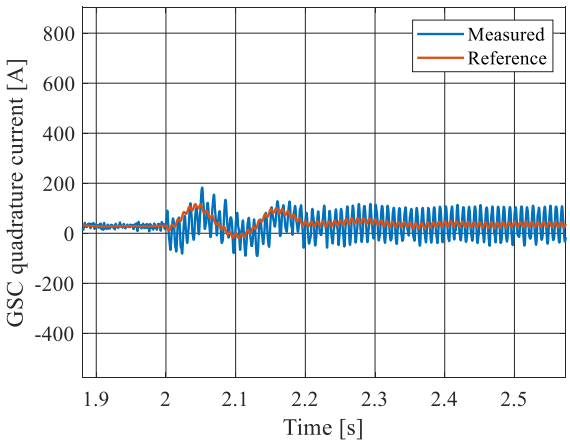

(b)

Figure 4.49 – GSC currents for unbalanced voltage sag: (a) direct axis and (b) quadrature axis.

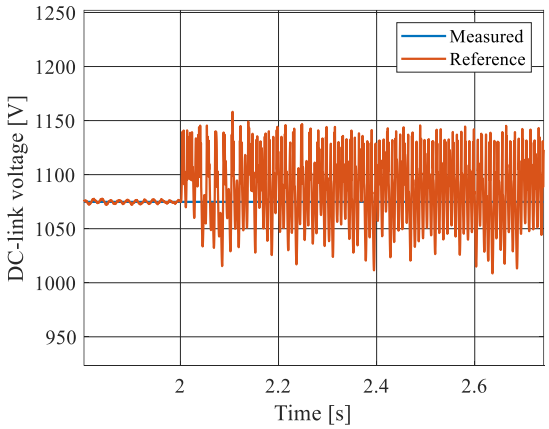

Figure 4.50 – DC-link voltage for unbalanced voltage sag.

The semiconductor devices are also subject to oscillations caused by the negative sequence. Figure 4.51 shows the temperature of these devices used in the GSC. It is notable, at the beginning of the sag, the rise in temperature of the diode. This is because, just like in balanced sags, the DC-link voltage tends to increase. Thus, the GSC currents also increase in order to keep both the voltage and power transfer constant. The IGBT's temperature experiences a decrease due reduction in the power that can be delivered to the grid, during the sag.

Figure 4.52 demonstrates the temperature variations in the semiconductor components housed within the RSC. A peak in the diode temperature is observable, attributable to the natural component, as observed in balanced sags. Additionally, the impact of the negative sequence is evident, sustaining elevated temperatures even after the decay of the natural component. Notably, the diode is more affected due to the power flow within the RSC, which is from the AC to the DC side.

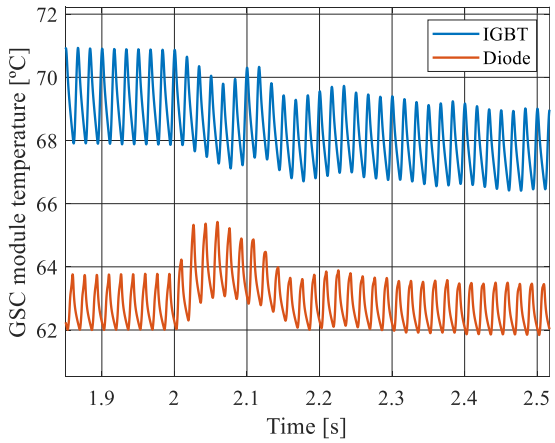

Figure 4.51 – GSC module temperature for unbalanced voltage sag.

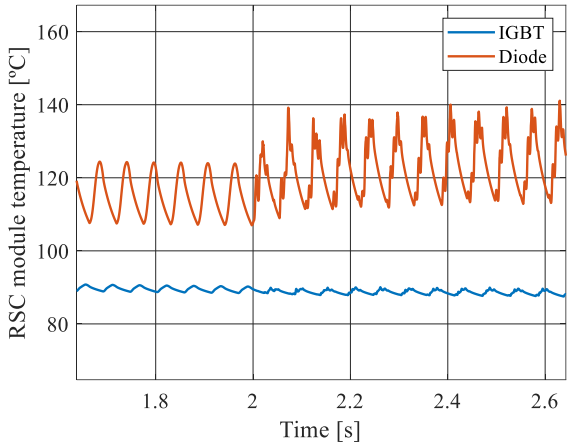

Figure 4.52 – RSC module temperature for unbalanced voltage sag.

It is important to reiterate that no RTFC strategy was employed in this test, and the device temperatures remained below the limit supported by the power module (maximum 175°C). Nevertheless, the tested voltage sag is not so severe and for greater unbalances the thermal stress is much higher due to the negative-sequence component. Initially, an effective RTFC strategy would involve controlling this negative-sequence component, addressing its impact on system variables to enhance overall performance and mitigate potential issues.

4.2.2. PIR strategy

In this test scenario, the control strategy utilized is a combination of classical PI control with resonant control. The assessment involves analyzing the behavior of the WECS under an unbalanced voltage sag of 60% concerning relevant variables. The timing

of this event was chosen to induce the highest natural component considering the very same conditions of the previously test.

Figure 4.53 illustrates the stator and rotor currents, respectively. Apart from the natural component, there's also the presence of the negative-sequence component inducing oscillations at twice the stator frequency (120 Hz). It is evident that the control encounters challenges in effectively managing the negative-sequence component.

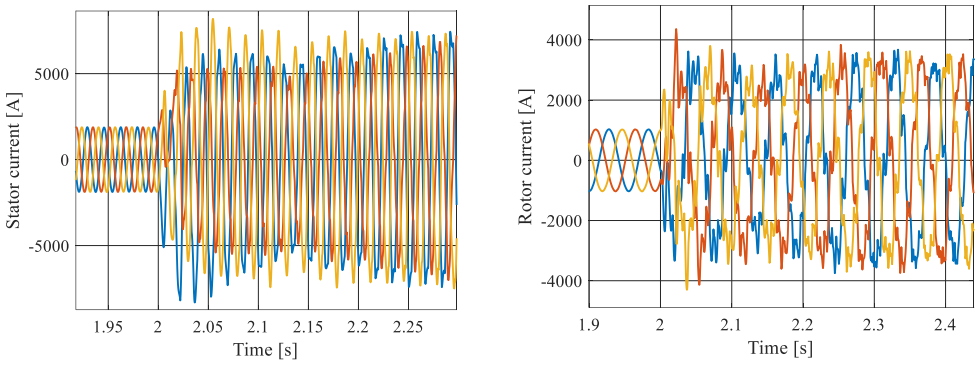

(a) (b)

Figure 4.53 - DFIG currents for an unbalanced voltage sag of 60%: (a) stator currents and (b) rotor currents.

Figure 4.54 showcases the direct-axis and quadrature-axis currents on the rotor, offering a clearer depiction of the control system's limitations in managing the negative-sequence component.

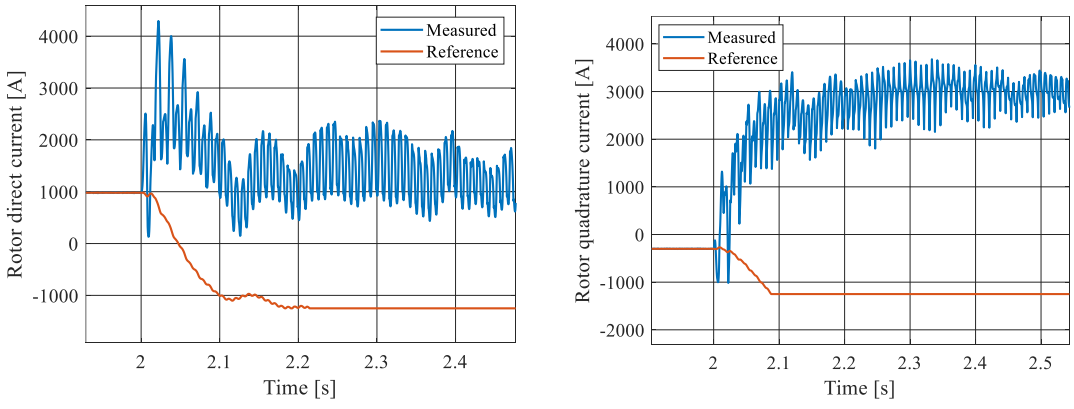

(a) (b)

Figure 4.54 - RSC currents for an unbalanced voltage sag of 60%: (a) d axis component and (b) q axis component.

Figure 4.55 illustrates the maximum voltage induced in the rotor corresponding to various levels of voltage sags. This graph was produced in accordance with Equation

(2.27), elucidating the impact of the sag level on the induced voltage in the rotor. Notably, the more severe the voltage sag, the higher the induced voltage in the rotor.

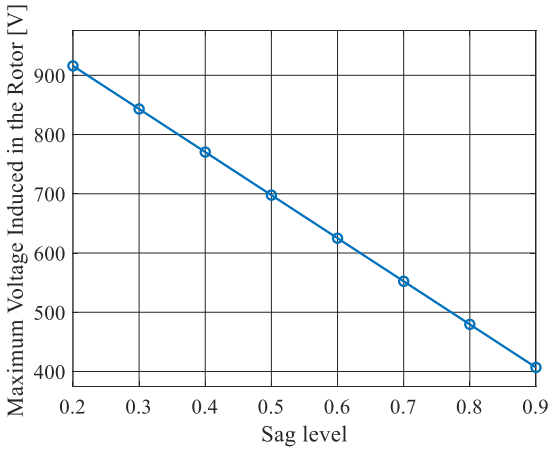

Figure 4.55 - Maximum voltage induced in the rotor with various sag levels.

Considering a phase-to-neutral sag of 60%, the voltage induced in the rotor would approximately amount to 625 V for the studied system, as depicted in Figure 4.55. . However, it is important to note that the nominal system's DC-link voltage is 698 V. Consequently, the converter has the capability to enforce a voltage of around 400 V. This circumstance pushes the converter into the overmodulation region, rendering the resonant control ineffective for this specific case. An analysis of the rotor voltage in Figure 4.56 indeed indicates that the peak values of the rotor voltages at the onset of the sag exceed the converter limit (400 V).

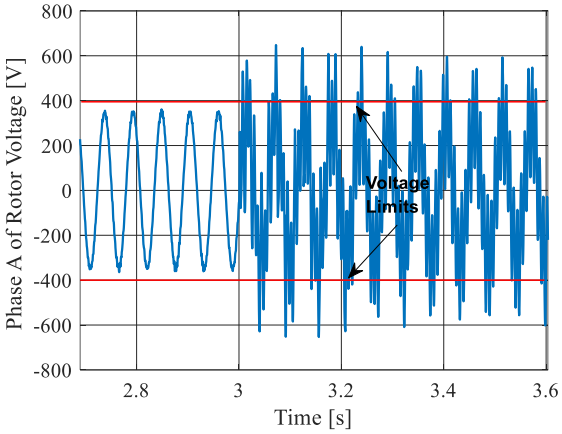

Figure 4.56 - Rotor voltage in phase A for unbalanced voltage sag of 60%.

Increasing the converter voltage limits by elevating the DC-link voltage could be a viable solution. For a 60% dip, the calculated induced rotor voltage is approximately 625 V, as previously noted. By augmenting the DC-link voltage to around 1000 V, there

would be ample room for the resonant control to intervene effectively in mitigating the negative-sequence component. As mentioned earlier, manufacturers typically recommend a module capable of withstanding a voltage around 60% of the DC-link voltage. Consequently, it became necessary to replace the previous power module with the FF1500R17IP5P model, rated at 1700 V, to accommodate this adjustment.

In this new test, conducted under the same conditions as the previous one, only the key variables highlighting the resonant controller's performance will be analyzed. Figure 4.57 exhibits the GSC currents, showcasing the resonant controller's action. Additionally, Figure 4.58 displays the rotor currents in the synchronous reference frame, enabling an evaluation of the control system's performance. Notably, the resonant controller demonstrates its capability to regulate the negative-sequence components, while also allowing for observing the transient behavior of the natural component.

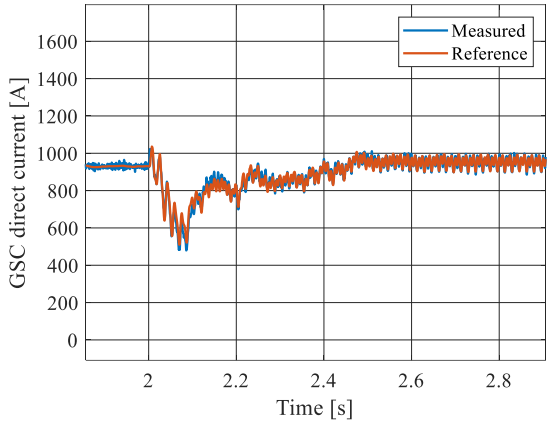

(a)

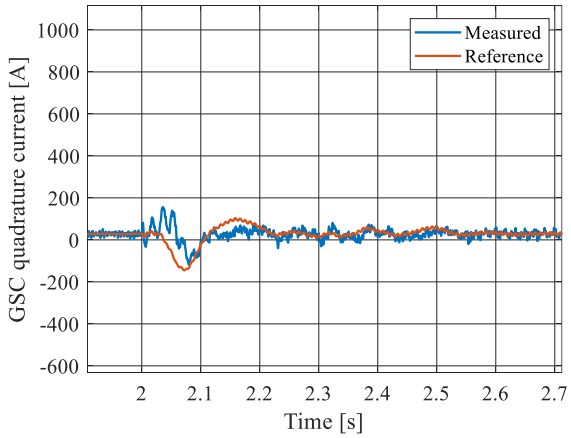

(b)

Figure 4.57 - GSC currents during an unbalanced voltage sag of 60%: (a) *d* axis component and (b) *q* axis component.

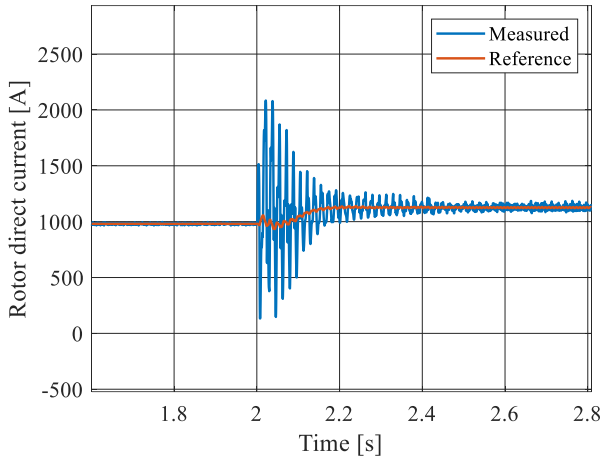

(a)

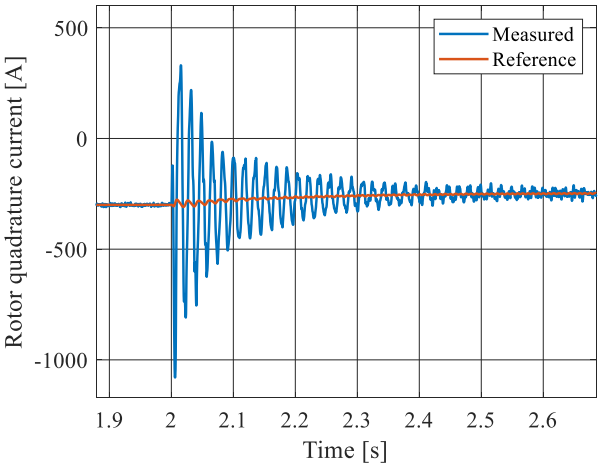

(b)

Figure 4.58 - Rotor currents an unbalanced voltage sag of 60%: (a) *d* axis component and (b) *q* axis component.

Figure 4.59(a) displays the temperature of the power semiconductor module utilized in the GSC. At the onset of the sag, there's a slight increase in the diode temperature. This is due to the tendency of the DC-link voltage to rise, subsequently causing an increase in GSC currents to maintain both voltage and power at a constant level. Meanwhile, Figure 4.59(b) illustrates temperatures in the semiconductors of the RSC. Despite the voltage sag, the average temperature of devices experiences a slight decrease, although an even greater reduction was expected. However, it does not occur because the negative-sequence component may remain during the whole dip. Since the thermal dynamics is slower that of the currents, the system may still remain under the harmful effects of the negative-sequence component.

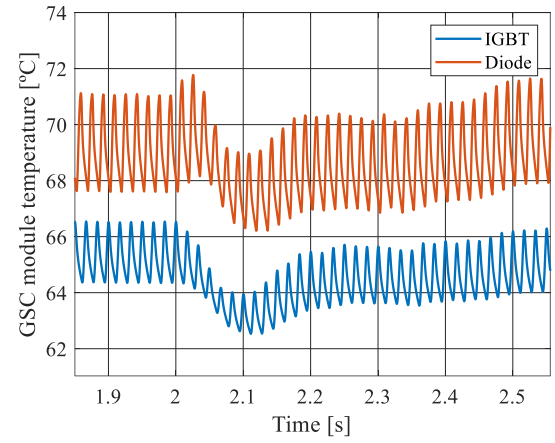

(a)

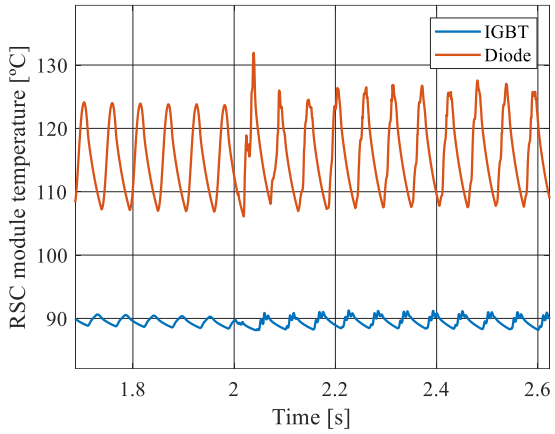

(b)

Figure 4.59 - Junction temperature of the power module during unbalanced voltage sag of 60%: (a) GSC and (b) RSC.

4.2.3. MCCR strategy

To verify the effectiveness of the MCC combined with the resonant control set, a test was conducted under identical conditions outlined in the preceding subsection, with a DC-link voltage of 1000 V. For the gain of the magnetizing loop, $k_{pim} = 10$ was selected, which was found to be the optimal choice in subsection 4.1.2. Consequently, only the variables that best demonstrate the control system's performance will be analyzed in this particular test.

Figure 4.60 exhibits the rotor currents in the synchronous reference frame, providing insight into the functionality of the MCC combined with the resonant control set.

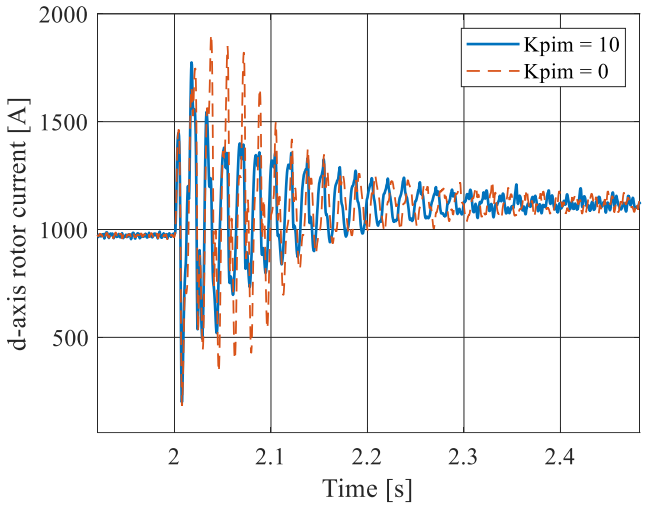

(a)

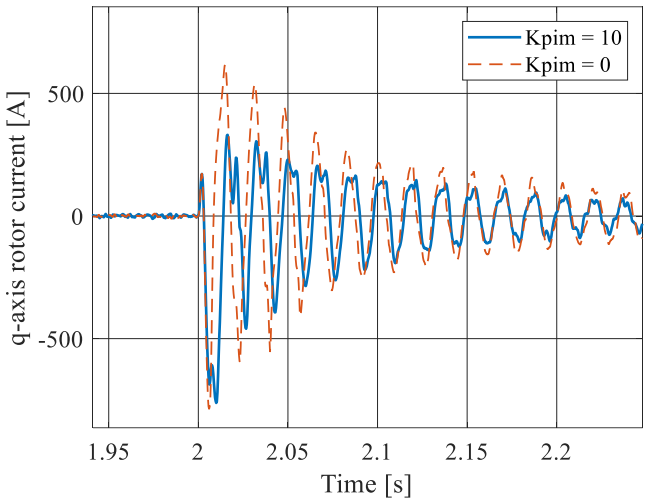

(b)

Figure 4.60 - Rotor currents using the MCCR strategy: (a) d-axis component and (b) q- axis component.

Looking at the Figure 4.60 it is notable that is possible to use the MCC in conjunction with the resonant control, where it is evident that the control of the magnetizing current contributes to the reduction of the natural component that appears at the beginning of the sag. This reduction becomes clearer when observing Figure 4.61, which the system recovers from the voltage dip.

In this case study, the reduction of the oscillations is not very impressive due to the voltage limit imposed by the DC-link that hinders the control action. Nevertheless, the objective is to show that the strategies can be combined.

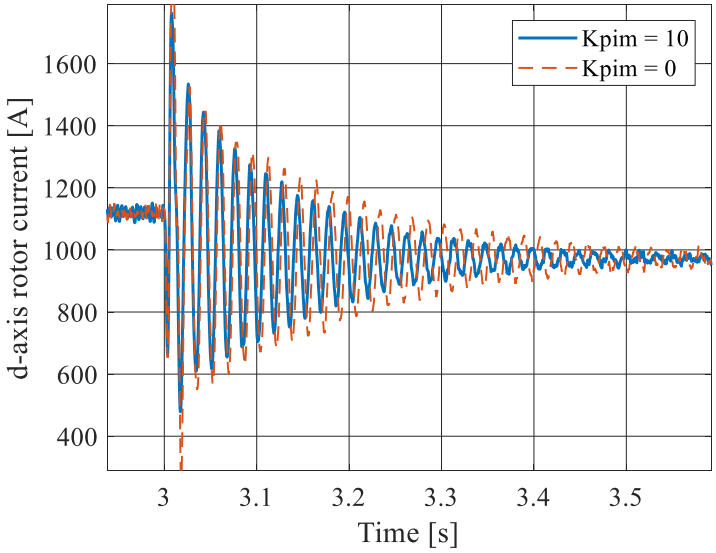

(a)

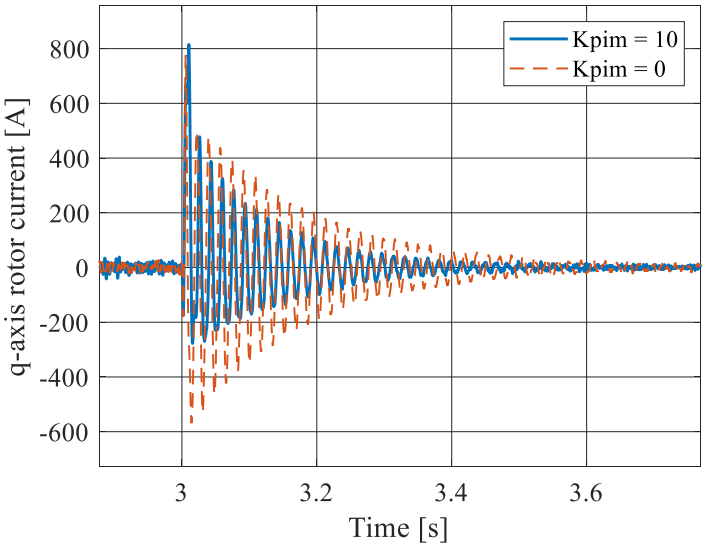

(b)

Figure 4.61 - Rotor currents at the system recovery: (a) d-axis component and (b) q- axis component.

It is also important to analyze how the MCCR affects the thermal behavior of the semiconductor devices. Figure 4.62 shows the junction temperatures of the IGBTs and diodes in the RSC. It is possible to notice that the gain of the MCC loop influences the peak of the junction temperature of the semiconductor devices and contributes in order to reduce this peak.

Therefore, it can be concluded that is possible to use the magnetizing current control combined with the resonant control and it offers improvements in the thermal

behavior of the semiconductors components present in the power converters of the system.

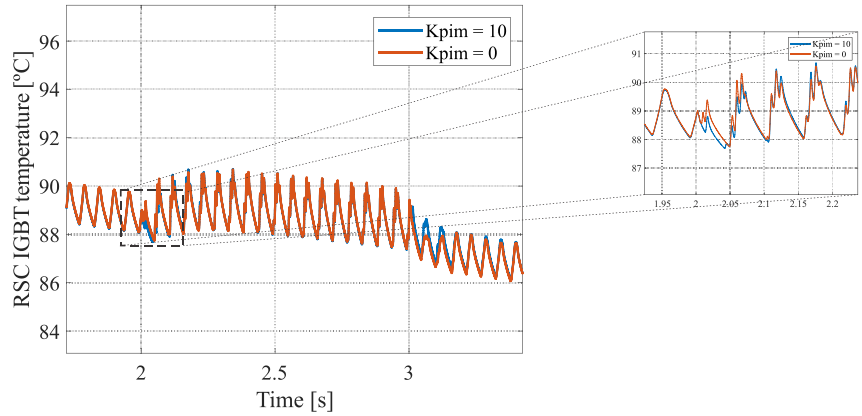

(a)

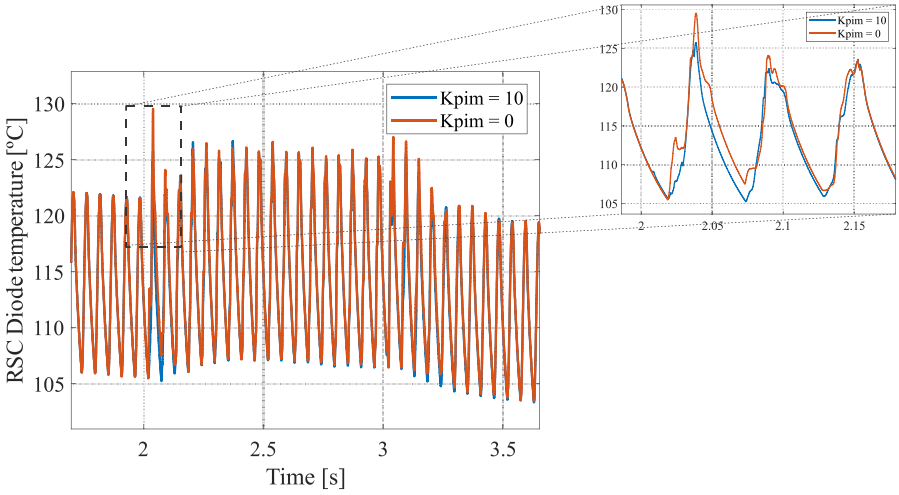

(b)

Figure 4.62 - Junction temperature of the power semiconductors for different mcc gains: (a) IGBT and (b) diode.

4.2.4. FSCR strategy

In the original work that proposed this strategy, the unbalanced voltage sags was not analyzed. So, the next results have the objective of expanding the analysis, adding a study of the strategy performance in face of the unbalanced voltage sags. For this, it is proposed here the implementation of a resonant controller with the current control loop. In this application, the stator currents in the synchronous *dq* reference frame underwent

filtration via a notch filter set to a frequency of 120 Hz, as described in Subsection 3.3.2. To investigate the behavior of the power semiconductors devices a phase-ground sag, where phase A its values reduced to 60% of their nominal value was simulated. This test was performed at DC-link voltage of 698V, supersynchronous speed (2340 rpm) and rated power (2 MW).

While effective in mitigating the natural component, this strategy exhibits a notable response during balanced voltage sags. However, its application in unbalanced voltage sags introduces challenges due to the presence of the negative-sequence component, as evidenced in Figure 4.63.

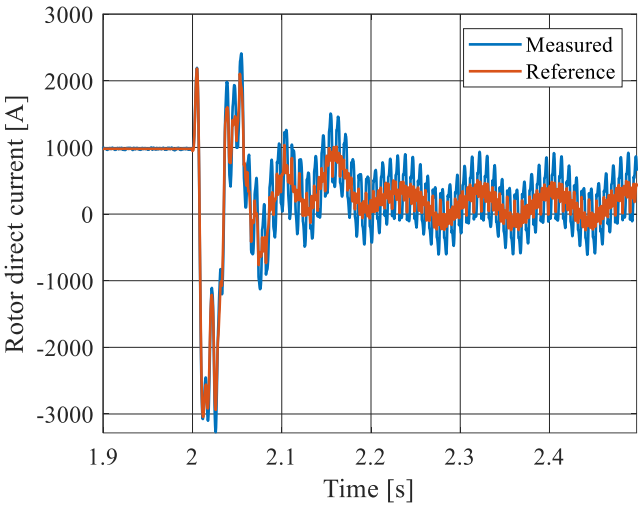

(a)

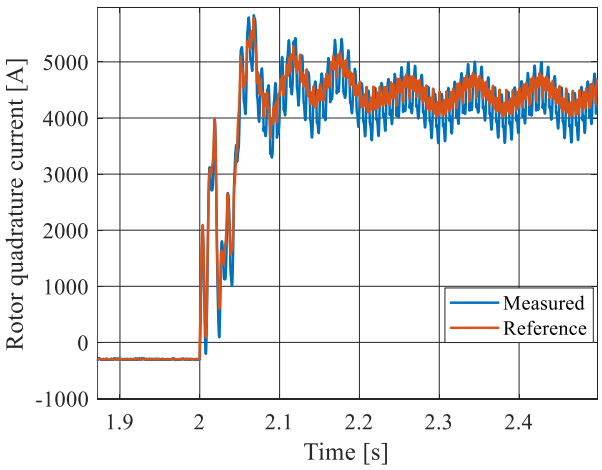

(b)

Figure 4.63 - Rotor currents for unbalanced voltage sag of 60%: (a) d-axis component and (b) q-axis component.

The results indicate an enhancement in rotor current management, notably in the control of the negative sequence. However, despite this improvement, there remains a substantial consumption of reactive current, resulting in exceedingly high temperatures within the semiconductor devices, as depict in Figure 4.64. These temperatures exceeds the maximum threshold (175 °C) that the modules can tolerate.

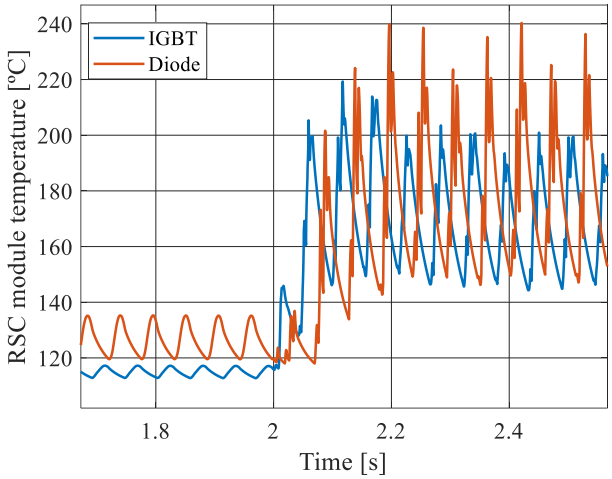

Figure 4.64 - Temperature of the semiconductor devices for unbalanced voltage sag of 60%.

Hence, it is evident that the strategy necessitates a voltage margin beyond the system's capacity for effective operation. Additionally, elevating the DC link voltage, essentially oversizing the system's thermal design, demands modules with higher voltage classes, thereby escalating costs and generating amplified power losses in power semiconductors. Consequently, the proposed modification in the strategy is deemed unfavorable for the system, particularly concerning the semiconductor devices.

Both the CRTC and FSCR strategies exhibit similar behaviors and are not suitable for managing unbalanced sags. Consequently, the CRTC strategy will not be assessed under such conditions.

4.2.5. RTFC comparison for unbalanced voltage sags

This subsection shows a comparison between strategies aimed at unbalanced voltage sags. The base case for the DC-link voltage (698 V) was considered in these tests, along with a supersynchronous speed (2340 RPM) and 2.0 MW of power production. The reason was to understand the limits of the strategies and how they affect the system variables. In line with the balanced sag scenario, these tests also employed a k_{pim} gain set

to 10 for the MCCR strategy. Figure 4.65 depicts the maximum rotor voltage for the strategies studied.

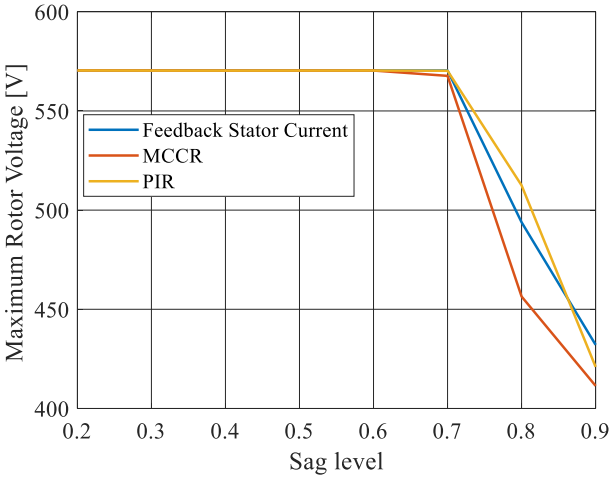

Figure 4.65 - Maximum rotor voltage for the RTFC strategies studied at different unbalanced sag values.

It is possible to observe a similar behavior between the strategies, up to a certain value the maximum rotor voltage remains constant, since the control is saturated. For smaller sags, the necessary voltage is smaller. It is worth mentioning that the strategies use the same device to control the negative-sequence component, a resonant control tuned to a frequency of 120 Hz. Therefore, this control requires a higher voltage margin from the converter for more severe sags.

However, it is necessary to analyze how the negative sequence control of each strategy impacts the power semiconductors. The negative-sequence component, if not well controlled, can cause great stress in the semiconductor components, as can be seen in Figure 4.66.

Notably, all the strategies cited here require a voltage level higher than that provided by the converter for controlling the negative-sequence component.

The FSCR strategy is the one that exhibits the most chaotic behavior, being the one that can stress the semiconductor components the most if the controllers are not properly adjusted, as depicted in Figure 4.64. For this reason, it will be not analyzed in this following tests.

Figure 4.66 exhibits the maximum rotor currents for various levels of sag. Noticeably, as the voltage sag becomes more severe, the rotor currents escalate, occasionally reaching values up to five times the nominal current (1000 A). Another

crucial point to highlight pertains to the discrepancy between the values observed for a sag of 0.6 and those presented in Figure 4.58 (PIR) and Figure 4.60 (MCC). This disparity arises from the use of the nominal system bus voltage (698 V) in this specific test, as depicted in Figure 4.66. As elucidated in this study, this voltage value is insufficient for the control to effectively manage the negative sequence component. Hence, it becomes imperative to prevent the converter from operating in overmodulation and to ensure an adequate voltage margin for the system's safe and reliable operation.

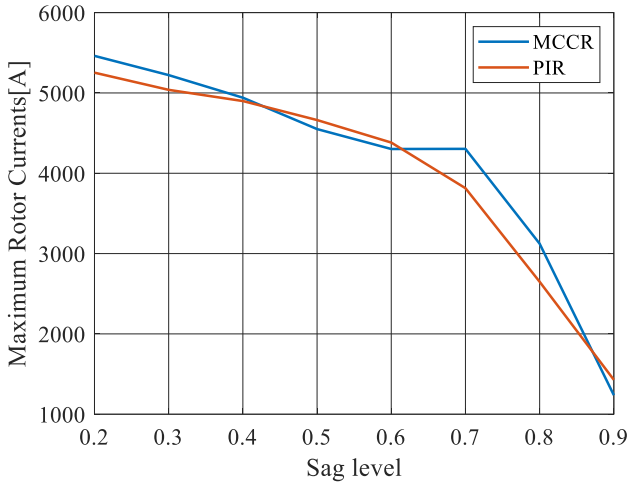

Figure 4.66 - Maximum rotor current for the RTFC strategies studied at different unbalanced voltage sags values.

This limitation in controlling the negative sequence component is reflected in the semiconductor junction temperatures, as can be seen in Figure 4.67.

It is evident that the high values that semiconductor temperatures can reach are due to the negative-sequence component. As this component will last throughout the entire sag, it contributes to the increase in voltage and current in the semiconductors, which is reflected in their junction temperatures, which remain high for more cycles. This is because the temperature dynamics is slower than the current dynamics. The temperature values displayed by semiconductor devices under the influence of these strategies indicate minimal differences, although there is a slight variance present. This discrepancy arises from the MCCR strategy's impact on the natural component of the stator flux, contributing to a reduction in its decay time.

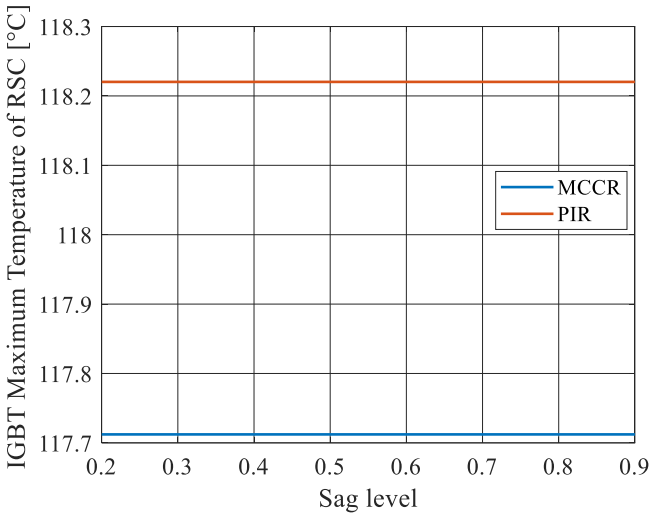

(a)

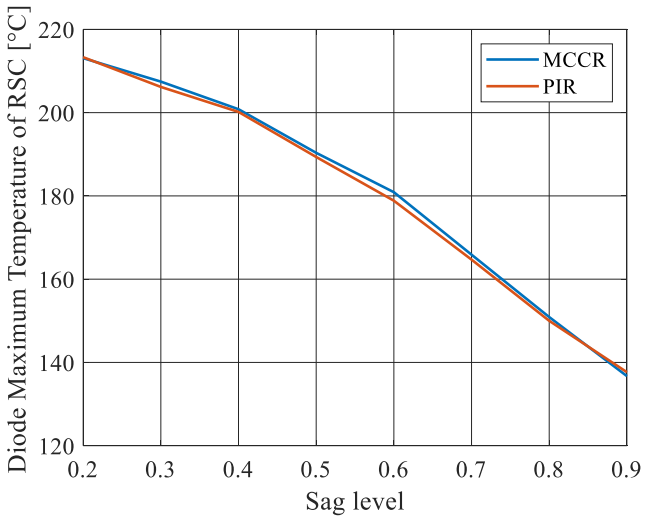

(b)

Figure 4.67 - Maximum junction temperatures of the RSC power semiconductors for the RTFC strategies studied at different unbalanced voltage sags values: (a) IGBT and (b) diode.

Figure 4.68 presents the average power losses for the aforementioned strategies when the system is subjected to an unbalanced voltage sag of 20%.

Analyzing Figure 4.68, it is even more evident the impact that the negative-sequence component has on thermal stresses in power semiconductors. The power losses are much higher than those listed in Figure 4.42, since in unbalanced sags, in addition to the negative-sequence component, the natural component is also present in these tests.

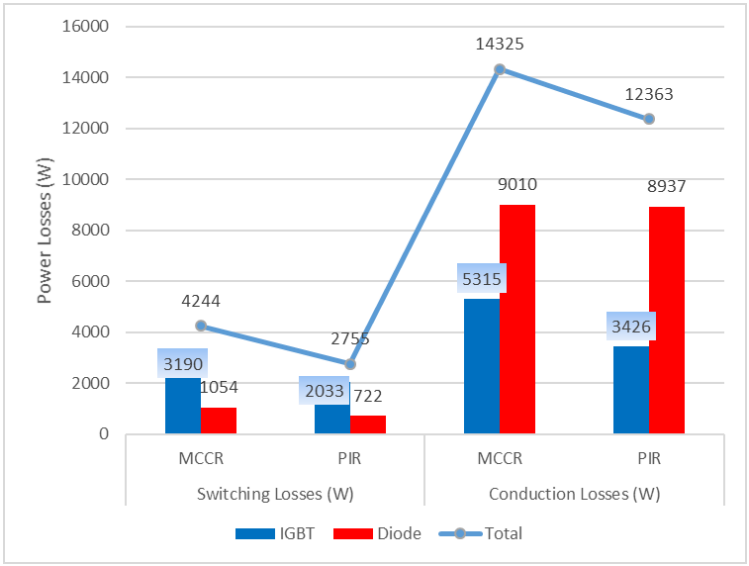

Figure 4.68 - Power losses on the power semiconductors for each RTFC strategies at a 0.2 unbalanced voltage sag.

Figure 4.69 depicts the relationship between the system's power losses under normal operating conditions and under the influence of unbalanced voltage sags. Significant increases in power losses are noticeable under unbalanced voltage sags, especially when the system operates in overmodulation. This highlights the influence of the negative sequence component on converter power losses. It underscores the importance of investigating the thermal behavior of semiconductor components to avoid subjecting them to conditions that would lead to high thermal stresses.

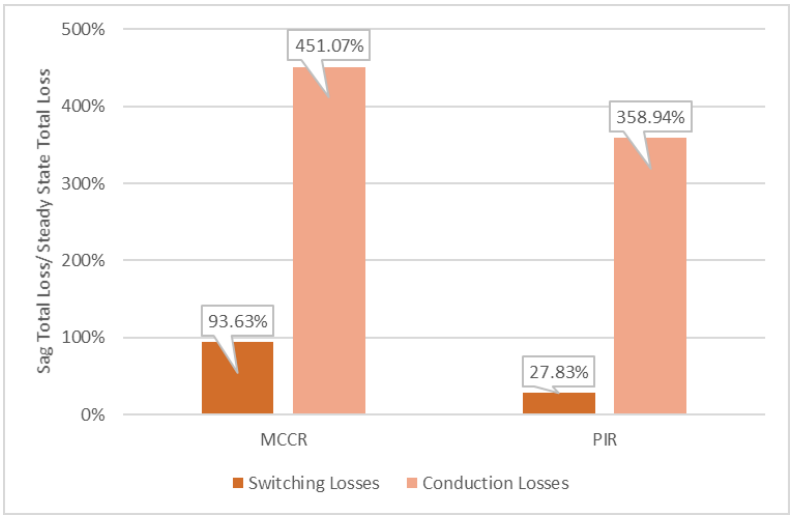

Figure 4.69 - Ratio of total power loss under normal conditions to losses during a 0.2 unbalanced sag for each RTFC strategy.

4.3. Effects of the change in the thermal design

As demonstrated in the preceding results, adjusting the DC bus voltage aids in diminishing rotor currents, consequently resulting in reduced junction temperatures of power semiconductors. However, such a modification necessitates a new selection of power modules with a higher voltage rating, consequently leading to an escalation in project costs. According to Infineon (2024), the cost of a module with a voltage rating of 1200 V and a current capacity of 1500 A is approximately $1135.07 each, whereas the same module with a voltage rating of 1700 V costs around $1299.78 each. This translates to an increase of nearly 15%.

The subsequent result demonstrate the feasibility of lowering the junction temperatures of the semiconductors to ensure that the project adheres to the maximum junction temperature requirements supported by the power module, even under more severe voltage sag conditions. To accomplish this, we altered the original configuration of the modules, employing two modules in parallel per phase, as depicted in Figure 4.70.

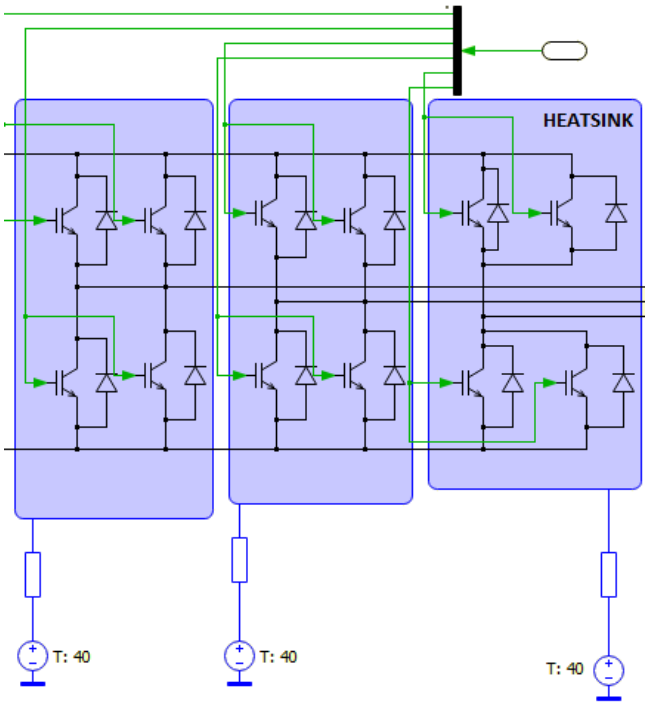

Figure 4.70 – New arrangement of the power modules on the rotor side of the converter.

Hence, a simulation was conducted to examine the impacts of this new thermal design. The LVRT MCC control strategy was implemented, and the analyzed system was subjected to a balanced voltage sag of 20%.

It is noteworthy to mention that only the MCC control strategy will be evaluated, as the others operate on the same premise of controlling the magnetization current. Consequently, it can be inferred that the effects will be analogous to the other strategies. Figure 4.71 depicts the junction temperatures of the semiconductor devices in the RSC.

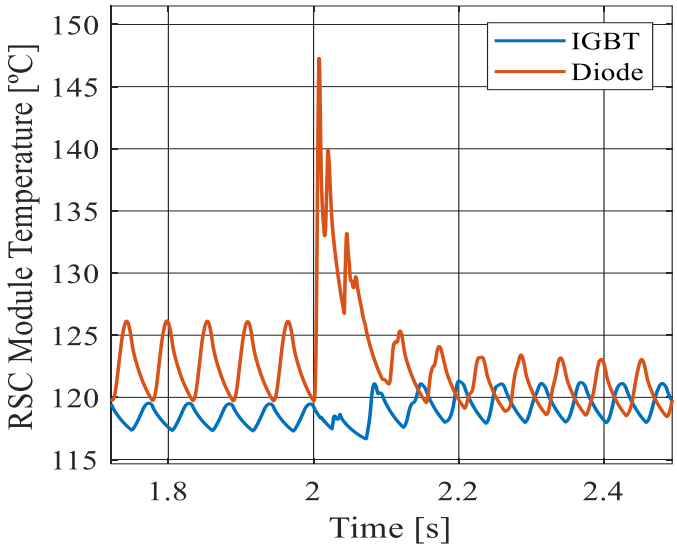

Figure 4.71 - Junction temperature of the power semiconductor devices on the rotor side of the converter when the system is subjected to a balanced voltage sag of 20%.

The reduction in junction temperature is apparent when compared to the result shown in Figure 4.24, with a decrease of nearly 17% in the temperatures of the semiconductor devices. Additionally, it is evident that in this outcome, the junction temperature of the semiconductors remains below the threshold supported by the power module (175°C).

Consequently, it can be concluded that there are more cost-effective methods for the thermal design to meet specifications and ensure the safe and reliable operation of the system. Another alternative would be to modify the thermal resistance of the heatsink or the type of cooling employed.

4.4. Chapter closure

This chapter has presented simulation results conducted using PLECS software, evaluating some RTFC strategies in WECS based on DFIG technology. The outcomes demonstrated the behavior of the system's most critical variables when exposed to both balanced and unbalanced voltage sags. These simulations underscored the potential harm voltage sags can inflict on DFIG systems and power semiconductor devices within converters. Notably, during balanced voltage sags, the emergence of the natural component of the stator flux induces high currents in the DFIG rotor. When combined with the negative sequence component prevalent in unbalanced sags, this situation poses a risk of converter damage due to increased heating in semiconductor devices. Additionally, this component leads to undesired power oscillations, contributing to the degradation of the system's power quality.

RTFC strategies tailored for balanced voltage sags exhibit promising outcomes, effectively managing the natural component and alleviating thermal stresses in semiconductor components. Meanwhile, strategies devised for unbalanced sags have also shown effectiveness in regulating the negative sequence component. Nevertheless, its effectiveness relies on ensuring an adequate voltage margin for the converter, a critical factor for achieving optimal control performance.

The comparison among the studied strategies highlighted their respective limitations, particularly when the converter lacks the capability to synthesize the required voltage for operation. This shortfall significantly impacts power semiconductors, underlining the critical influence of converter capacity on strategy effectiveness. A specific converter design is required to apply the RTFC strategies and ensure the proper control and safe operation of the converter.

Chapter 5. **CONCLUSIONS AND FUTURE WORK**

5.1. Conclusions

This work has presented a comprehensive thermal analysis of a DFIG-based WECS, focusing on evaluating the junction temperatures of power semiconductors to assess the thermal stress they endure. The results underscored the behavior of critical variables during voltage sags, emphasizing the DFIG's sensitivity to power quality fluctuations. Notably, fluctuations in the stator flux induce overcurrents in the rotor, driven by the presence of both natural and negative-sequence components. This issue intensifies with higher sag levels, as increased values of these components correspondingly elevate the junction temperature of semiconductors. Hence, it is reasonable to assert that understanding the thermal profile of power semiconductors is pivotal in system design to ensure safe operation during such phenomena.

The obtained results indicate that the MCC strategy is advantageous, effectively mitigating oscillations induced by the natural component of the stator flux. However, when assessing currents in the DFIG rotor, a clear correlation emerges between the maximum peak reached at the dip's onset and the gain of the MCC. The selection of k_{pim} holds immense significance—higher gains, while not significantly reducing stator flux decay, saturate the curve and lead to amplified rotor currents. Consequently, this escalation is reflected in the temperatures of the IGBTs and diodes within the converter's power module, resulting in overheating issues.

The increase of the DC-link voltage plays a role in diminishing rotor currents and alleviating thermal stress on semiconductors. However, this adjustment impacts the efficiency of the MCC by inducing an escalation in the oscillation of the natural component of the stator flux.

The FSCR strategy exhibited limitations, particularly when confronted with more severe balanced sags, necessitating an elevation in the DC-link voltage. However, this adjustment must be carefully executed to avoid oversizing the system, as it tends to raise the temperatures of power semiconductors, even under sags considered less severe.

The outcomes from the CRTC strategy unveil an interdependency among the stator flux, rotor voltage, and rotor current linked to the monitoring coefficient k_r. Elevated values of this gain result in a more pronounced reduction in the natural component but lead to a significant increase in rotor current. Consequently, this surge in current elevates thermal stresses on the power semiconductors. Hence, it's imperative to select a gain that strikes a balance, minimizing thermal stress while offering effective attenuation of the natural component. Besides inducing overcurrents in the rotor, this component also triggers oscillations in electromagnetic torque and mechanical vibrations, which pose harm to the DFIG.

The PI + R controller implemented in this study demonstrated effectiveness in mitigating the negative-sequence component, thereby preventing excessive temperature elevation in power semiconductors during the sag. However, further research suggests that this strategy could enhance its effectiveness by augmenting the converter's voltage capability, allowing for a broader margin in the control system. Consequently, selecting IGBTs rated at higher voltages becomes necessary, albeit leading to an overall increase in costs.

The integration of resonant control alongside magnetizing current control showcased improvements in system response. However, similar to other strategies, the efficacy of this approach is constrained by the converter's capabilities. The previous conclusions regarding the impact of converter limitations and the associated considerations remain applicable to this strategy as well.

This work aimed to further explore the resilience of DFIG systems. Through the detailed analyses conducted, a deeper understanding emerged regarding the response of power semiconductors when exposed to the adverse effects of both balanced and unbalanced voltage sags. The presented results emphasize the critical significance of these semiconductor devices in designing a system that ensures safe and dependable operation, even under the most challenging and unfavorable conditions.

5.2. Future works

Continuing this work relies on establishing functionality within the WECS workbench. This will enable the execution of a smaller-scale test, primarily focusing on experimentally validating the strategies from a control perspective. Additionally, to

validate the thermal aspects, a dedicated bench capable of directly measuring the temperature of semiconductor components becomes necessary.

It could be insightful to analyze the control strategy in conjunction with additional hardware-based strategies aimed at enhancing the system's protection level. This combined analysis might offer a comprehensive understanding of how these integrated approaches could fortify the system against various challenges and potentially improve its overall resilience.

Simulating alternative modulation strategies and analyzing their impact on the thermal behavior of power converters could provide valuable insights into their efficacy and thermal performance. By exploring various modulation techniques and assessing their effects on converter temperatures, one can gain a clearer understanding of their thermal implications and potential advantages or limitations compared to existing strategies.

The strategies examined in this study might find applications in other WECS systems employing different generator types, such as synchronous generators with full converters or utilizing alternative energy conversion technologies. Adapting and applying these strategies to diverse systems could potentially enhance their resilience and performance, contributing to a broader range of renewable energy systems beyond DFIG-based ones. Exploring their applicability in various setups could uncover their versatility and utility in different contexts of energy conversion.

REFERENCES

ABDELSALAM, I., ADAM, G. P., HOLLIDAY, D. & WILLIAMS, B. W. 2014. Modified back-to-back current source converter and its application to wind energy conversion systems. *IET Power electronics,* 8**,** 103-111.

ALAM, M. S., HOSSAIN, M. I., HOSSAIN, M. A., CHOUDHORY, M. S. H. & UDDIN, M. A. Protection of inverter-based distributed generation with series dynamic braking resistor: A variable duty control approach. 2018 10th International Conference on Electrical and Computer Engineering (ICECE), 2018. IEEE, 253-256.

AMORIM, A. E., OLIVEIRA, F. D. & SIMONETTI, D. S. 2021. A new hybrid multilevel back-to-back converter for doubly fed induction generator-based wind turbines' fault supportability. *International Transactions on Electrical Energy Systems,* 31**,** e12793.

ASADI, F. & EGUCHI, K. 2020. Chapter 5 - Thermal analysis of power electronics converters with PLECS. *In:* ASADI, F. & EGUCHI, K. (eds.) *Simulation of Power Electronics Converters Using PLECS®.* Academic Press.

BAIJU, P. & RAJEEV, T. Low Voltage Ride Through in DFIG based wind turbines: A review. Control Communication & Computing India (ICCC), 2015 International Conference on, 2015. IEEE, 337-342.

BAIMEL, D., CHOWDHURY, N., BELIKOV, J. & LEVRON, Y. 2021. New type of bridge fault current limiter with reduced power losses for transient stability improvement of DFIG wind farm. *Electric Power Systems Research,* 197**,** 107293.

BOLLEN, M. H. 2000. Understanding power quality problems. *Voltage Sags and Interruptions.* IEEE press.

BUSO, S. & MATTAVELLI, P. 2015. Digital control in power electronics. *Synthesis Lectures on Power Electronics,* 5**,** 1-229.

CHANG, Y., MAHSEREDJIAN, J., KOCAR, I. & KARAAGAC, U. 2022. Analytical characterization of DFIG response to asymmetrical voltage dips for efficient design. *Electric Power Systems Research,* 211**,** 108553.

CHEN, J., XUE, A., TIAN, C., BI, T. & GAO, C. A new method to improve the LVRT of DFIG based on the current compensation. Proceedings of the 30th Chinese Control Conference, 2011. IEEE, 5148-5152.

CHEN, L., DENG, C., ZHENG, F., LI, S., LIU, Y. & LIAO, Y. 2014. Fault ride-through capability enhancement of DFIG-based wind turbine with a flux-coupling-type SFCL employed at different locations. *IEEE Transactions on Applied Superconductivity,* 25**,** 1-5.

CHEN, L., DING, M., LI, Z., QIAO, X., TANG, J., ZHAO, Z., WANG, X., CHEN, H., DENG, X. & ISLAM, M. R. 2022. Coordination of adaptive virtual resistance controller and flux-coupling-type fault current limiter for LVRT fulfillment of virtual synchronous generator. *Electric Power Systems Research,* 210**,** 108112.

DAI, J., XU, D., WU, B. & ZARGARI, N. R. 2010. Unified DC-link current control for low-voltage ride-through in current-source-converter-based wind energy conversion systems. *IEEE Transactions on power electronics,* 26**,** 288-297.

DE ESPAÑA, R. E. 2006. Procedimiento de Operación 12.3. Requisitos de respuesta frente a huecos de tensión de las instalaciones eólicas. *Resolución de,* 4**,** 37017-37019.

DEMIN, S., SITBON, M., AHARON, I., BARBI, E., MACHLEV, R., BELIKOV, J., LEVRON, Y. & BAIMEL, D. 2023. A new resonant fault current limiter for improved wind turbine transient stability. *Electric Power Systems Research,* 223**,** 109600.

DJERIDANE, M. E., MECHGOUG, R., AJGOU, R. & CHEMSA, A. Fuzzy rotor side control of a DFIG-based wind turbine. 2018 International Conference on Communications and Electrical Engineering (ICCEE), 2018. IEEE, 1-7.

DÖŞOĞLU, M. K. 2020. Crowbar hardware design enhancement for fault ride through capability in doubly fed induction generator-based wind turbines. *ISA Transactions,* 104**,** 321-328.

ELSHIEKH, M., ELWAKEEL, A., VENUTURUMILLI, S., ALAFNAN, H., PEI, X., ZHANG, M. & YUAN, W. 2021. Utilising SMES-FCL to improve the transient behaviour of a doubly fed induction generator DC wind system. *International Journal of Electrical Power & Energy Systems,* 131**,** 107099.

ELTAMALY, A. M., AL-SAUD, M., SAYED, K. & ABO-KHALIL, A. G. 2020. Sensorless active and reactive control for DFIG wind turbines using opposition-based learning technique. *Sustainability,* 12**,** 3583.

ENERGINET, D. 2016. Technical regulation 3.2. 5 for wind power plants above 11 kW. *Tech. Rep.*

EPOWERBAY. 2022. *Fabricantes de Aerogeradores: Os Maiores em operação no Brasil-2022* [Online]. Available: https://www.epowerbay.com/single-post/fabricantes-de-aerogeradores-os-maiores-em-operacao-no-brasil-2022 [Accessed 12/09/2023 2022].

ERICKSON, R. W. & MAKSIMOVIC, D. 2007. *Fundamentals of power electronics*, Springer Science & Business Media.

FLANNERY, P. S. & VENKATARAMANAN, G. 2008. A fault tolerant doubly fed induction generator wind turbine using a parallel grid side rectifier and series grid side converter. *IEEE Transactions on power electronics,* 23**,** 1126-1135.

FORTESCUE, C. L. 1918. Method of symmetrical co-ordinates applied to the solution of polyphase networks. *Transactions of the American Institute of Electrical Engineers,* 37**,** 1027-1140.

GONÇALVES SOTELO, G., SANTOS, G. D., SASS, F., FRANÇA, B. W., NOGUEIRA DIAS, D. H., ZAMBOTI FORTES, M., POLASEK, A. & DE ANDRADE JR, R. 2022. A review of superconducting fault current limiters compared with other proven technologies. *Superconductivity,* 3**,** 100018.

GRAY, C., BUQUE, C. & CHOWDHURY, S. AC series dynamic resistor protection scheme with switching control for doubly fed induction generator based WECS. 2016 IEEE Power and Energy Society General Meeting (PESGM), 2016. IEEE, 1-5.

GWEC 2021. Global Wind Report 2021.

GWEC 2023. Global Wind Report 2023.

HAHN, F., ANDRESEN, M., BUTICCHI, G. & LISERRE, M. Mission Profile Based Reliability Evaluation of Building Blocks for Modular Power Converters. PCIM Europe 2017; International Exhibition and Conference for Power Electronics, Intelligent Motion, Renewable Energy and Energy Management, 16-18 May 2017 2017. 1-7.

HAIDAR, A. M., MUTTAQI, K. M. & HAGH, M. T. 2017. A coordinated control approach for DC link and rotor crowbars to improve fault ride-through of DFIG-based wind turbine. *IEEE Transactions on Industry Applications,* 53**,** 4073-4086.

HAVA, A. M., KERKMAN, R. J. & LIPO, T. A. 1999. Simple analytical and graphical methods for carrier-based PWM-VSI drives. *IEEE transactions on power electronics,* 14**,** 49-61.

HE, W., KING, M., LUO, X., DOONER, M., LI, D. & WANG, J. 2021. Technologies and economics of electric energy storages in power systems: Review and perspective. *Advances in Applied Energy,* 4**,** 100060.

HIREMATH, R. & MOGER, T. 2022. Modified Super Twisting algorithm based sliding mode control for LVRT enhancement of DFIG driven wind system. *Energy Reports,* 8**,** 3600-3613.

HOPFENSPERGER, B., ATKINSON, D. & LAKIN, R. 2000. Stator-flux-oriented control of a doubly-fed induction machine: with and without position encoder. *IEE Proceedings-Electric power applications,* 147**,** 241-250.

HOSSAIN, M., POTA, H. & RAMOS, R. 2012. Improved low-voltage-ride-through capability of fixedspeed wind turbines using decentralised control of STATCOM with energy storage system. *IET generation, transmission & distribution,* 6**,** 719-730.

HU, J. & HE, Y. 2009. Modeling and enhanced control of DFIG under unbalanced grid voltage conditions. *Electric Power Systems Research,* 79**,** 273-281.

HU, J. & HE, Y. 2011. DFIG wind generation systems operating with limited converter rating considered under unbalanced network conditions–analysis and control design. *Renewable Energy,* 36**,** 829-847.

HU, J., HE, Y., XU, L. & WILLIAMS, B. W. 2008. Improved control of DFIG systems during network unbalance using PI–R current regulators. *IEEE Transactions on Industrial Electronics,* 56**,** 439-451.

HU, J., XU, H. & HE, Y. 2012. Coordinated control of DFIG's RSC and GSC under generalized unbalanced and distorted grid voltage conditions. *IEEE Transactions on Industrial Electronics,* 60**,** 2808-2819.

HUANG, P.-H., EL MOURSI, M. S. & HASEN, S. A. 2014. Novel fault ride-through scheme and control strategy for doubly fed induction generator-based wind turbine. *IEEE transactions on energy conversion,* 30**,** 635-645.

HUANG, Q., ZOU, X., ZHU, D. & KANG, Y. 2016. Scaled current tracking control for doubly fed induction generator to ride-through serious grid faults. *IEEE Transactions on Power Electronics,* 31**,** 2150-2165.

INFINEON 2015. Application note AN2015-10: Transient Thermal Measurements and thermal equivalent circuit models. *Infineon Technologies AG, Munich, Germany*.

INFINEON 2017. Datasheet of module FF1500R12IE5. S.I.

INFINEON 2020. Datasheet of module FF1700R17IP5P. S.I.

INFINEON.2024.Available: https://www.infineon.com/cms/en/product/power/igbt/igbt-modules/ [Accessed 01/11 2024].

ISLAM, M. R., HASAN, J., HASAN, M. M., HUDA, M. N., HOSSAIN SADI, M. A. & ABUHUSSEIN, A. 2020. Performance improvement of DFIG-based wind farms using NARMA-L2 controlled bridge-type flux coupling non-superconducting fault current limiter. *IET Generation, Transmission & Distribution,* 14**,** 6580-6593.

ISLAM, M. R., HOSSAIN, M. A., HASAN, J., ROY, T. K. & SADI, M. A. H. 2022. Double integral sliding mode controller based bridge-type flux-coupling non-superconducting fault current limiter to protect DFIG-based multi-machine power system under transient-state. *International Journal of Electrical Power & Energy Systems,* 142**,** 108271.

KASHKOOLI, M. R. A., MADANI, S. M. & LIPO, T. A. 2020. Improved Direct Torque Control for a DFIG under Symmetrical Voltage Dip With Transient Flux Damping. *IEEE Transactions on Industrial Electronics,* 67**,** 28-37.

KESHAVARZI, M. D. & ALI, M. H. FRT Capability Enhancement of Autonomous AC/DC Hybrid Microgrid by Coordinated MSDBR and Interlinking Converter Control Strategy. 2019 IEEE Power & Energy Society Innovative Smart Grid Technologies Conference (ISGT), 2019. IEEE, 1-5.

KIM, J., MULJADI, E., GEVORGIAN, V. & HOKE, A. F. 2019. Dynamic capabilities of an energy storage-embedded DFIG system. *IEEE Transactions on Industry Applications,* 55**,** 4124-4134.

KONG, X., WANG, X., ABDELBAKY, M. A., LIU, X. & LEE, K. Y. 2022. Nonlinear MPC for DFIG-based wind power generation under unbalanced grid conditions. *International Journal of Electrical Power & Energy Systems,* 134**,** 107416.

KOVÁCS, P. K. 1983. Transient phenomena in electrical machines. *394 pp*.

LIANG, J., QIAO, W. & HARLEY, R. G. 2010. Feed-forward transient current control for low-voltage ride-through enhancement of DFIG wind turbines. *IEEE Transactions on Energy Conversion,* 25**,** 836-843.

LIM, S.-H., AHN, H.-J. & PARK, C. 2013. Study on fault current limiting characteristics of an SFCL using magnetic coupling of two coils with mechanical switch driven by electromagnetic repulsion Force. *IEEE transactions on applied superconductivity,* 24**,** 1-4.

LIMA, F. K., LUNA, A., RODRIGUEZ, P., WATANABE, E. H. & BLAABJERG, F. 2010. Rotor voltage dynamics in the doubly fed induction generator during grid faults. *IEEE Transactions on power electronics,* 25**,** 118-130.

LISERRE, M., BLAABJERG, F. & HANSEN, S. 2005. Design and control of an LCL-filter-based three-phase active rectifier. *IEEE Transactions on industry applications,* 41**,** 1281-1291.

LISERRE, M., TEODORESCU, R. & BLAABJERG, F. 2006. Multiple harmonics control for three-phase grid converter systems with the use of PI-RES current controller in a rotating frame. *IEEE Transactions on Power Electronics,* 21**,** 836-841.

LIU, B., MENG, K., DONG, Z. Y., WONG, P. K. C. & TING, T. 2020a. Unbalance Mitigation via Phase-Switching Device and Static Var Compensator in Low-Voltage Distribution Network. *IEEE Transactions on Power Systems,* 35**,** 4856-4869.

LIU, J., XU, Y., DONG, Z. Y. & WONG, K. P. 2018. Retirement-Driven Dynamic VAR Planning for Voltage Stability Enhancement of Power Systems With High-Level Wind Power. *IEEE Transactions on Power Systems,* 33**,** 2282-2291.

LIU, J., YANG, Z., YU, J., HUANG, J. & LI, W. 2020b. Coordinated control parameter setting of DFIG wind farms with virtual inertia control. *International Journal of Electrical Power & Energy Systems,* 122**,** 106167.

LIU, R., YAO, J., WANG, X., SUN, P., PEI, J. & HU, J. 2019. Dynamic stability analysis and improved LVRT schemes of DFIG-based wind turbines during a symmetrical fault in a weak grid. *IEEE Transactions on Power Electronics,* 35**,** 303-318.

LÓPEZ, J., SANCHIS, P., GUBÍA, E., URSÚA, A., MARROYO, L. & ROBOAM, X. Control of doubly fed induction generator under symmetrical voltage dips. 2008 IEEE International Symposium on Industrial Electronics, 2008. IEEE, 2456-2462.

LOPEZ, J., SANCHIS, P., ROBOAM, X. & MARROYO, L. 2007. Dynamic behavior of the doubly fed induction generator during three-phase voltage dips. *IEEE Transactions on Energy Conversion,* 22**,** 709-717.

LU, Y. 2018. Adaptive-fuzzy control compensation design for direct adaptive fuzzy control. *IEEE Transactions on Fuzzy Systems,* 26**,** 3222-3231.

MENDES, V. F. 2009. *Avaliação do comportamento de um sistema de conversão de energia eólica utilizando gerador de indução duplamente excitado durante*

afundamentos de tensão equilibrados e desequilibrados. Dissertaçao (Mestrado)—Universidade Federal de Minas Gerais.

MENDES, V. F. 2013. *Ride-through fault capability improvement through novel control strategies applied for doubly-fed induction wind generators.* Universidade Federal de Minas Gerais- UFMG.

MENDES, V. F., DE SOUSA, C. V., SILVA, S., RABELO, B. C. & HOFMANN, W. 2011. Modeling and ride-through control of doubly fed induction generators during symmetrical voltage sags. *IEEE Transactions on Energy Conversion,* 26**,** 1161-1171.

MENSOU, S., ESSADKI, A., NASSER, T. & BOUOULID IDRISSI, B. 2020. A direct power control of a DFIG based-WECS during symmetrical voltage dips. *Protection and Control of Modern Power Systems,* 5**,** 5.

MOHAMMADI, J., VAEZ-ZADEH, S., AFSHARNIA, S. & DARYABEIGI, E. 2014. A combined vector and direct power control for DFIG-based wind turbines. *IEEE Transactions on Sustainable Energy,* 5**,** 767-775.

NADEEM, F., HUSSAIN, S. S., TIWARI, P. K., GOSWAMI, A. K. & USTUN, T. S. 2018. Comparative review of energy storage systems, their roles, and impacts on future power systems. *IEEE access,* 7**,** 4555-4585.

NADERI, S. B., NEGNEVITSKY, M. & MUTTAQI, K. M. 2019. A Modified DC Chopper for Limiting the Fault Current and Controlling the DC-Link Voltage to Enhance Fault Ride-Through Capability of Doubly-Fed Induction-Generator-Based Wind Turbine. *IEEE Transactions on Industry Applications,* 55**,** 2021-2032.

NEŠIĆ, D. & TEEL, A. R. 2004. Input-to-state stability of networked control systems. *Automatica,* 40**,** 2121-2128.

NGAMROO, I. 2017. Review of DFIG wind turbine impact on power system dynamic performances. *IEEJ Transactions on electrical and electronic engineering,* 12**,** 301-311.

OKEDU, K. E. 2019. Enhancing the performance of DFIG variable speed wind turbine using a parallel integrated capacitor and modified modulated braking resistor. *IET Generation, Transmission & Distribution,* 13**,** 3378-3387.

OKEDU, K. E., MUYEEN, S., TAKAHASHI, R. & TAMURA, J. 2012. Wind farms fault ride through using DFIG with new protection scheme. *IEEE Transactions on Sustainable Energy,* 3**,** 242-254.

OLIVEIRA, F., AMORIM, A., ENCARNAÇÃO, L., FARDIN, J., ORLANDO, M., SILVA, S. & SIMONETTI, D. 2015. Enhancing LVRT of DFIG by using a superconducting current limiter on rotor circuit. *Energies,* 9**,** 16.

OLIVEIRA, F. D. C. 2016. Suportabilidade a Afundamentos de Tensão em Geradores DFIG Empregando Limitador Supercondutor.

ONISHI, K., LI, Y., KOIWA, K., LIU, F., ZANMA, T. & LIU, K.-Z. 2023. Analysis on the operation of crowbar in doubly fed induction generators. *Electric Power Systems Research,* 215**,** 108950.

ONS 2009. Procedimentos de Rede - Submódulo 3.6: Requisitos técnicos mínimos para a conexão à rede básica.

ONS. 2011. Submódulo 2.8: Gerenciamento dos indicadores de desempenho da rede básica e dos barramentos dos transformadores de fronteira, e de seus componentes; resolução normativa. [Online]. Available: http://extranet.ons.org.br/operacao/prdocme.nsf/principalPRedeweb?openframeset.

OPPENHEIM, A. & WILLSKY, A. 2010. Sinais e Sistemas-2a edição. Editora Pearson.

OZSOY, E., PADMANABAN, S., MIHET-POPA, L., FEDÁK, V., AHMAD, F., AKHTAR, R. & SABANOVIC, A. 2017. Control strategy for a grid-connected inverter under unbalanced network conditions—A disturbance observer-based decoupled current approach. *Energies,* 10**,** 1067.

PALIZBAN, O. & KAUHANIEMI, K. 2016. Energy storage systems in modern grids—Matrix of technologies and applications. *Journal of Energy Storage,* 6**,** 248-259.

PANNELL, G., ZAHAWI, B., ATKINSON, D. J. & MISSAILIDIS, P. 2013. Evaluation of the performance of a DC-link brake chopper as a DFIG low-voltage fault-ride-through device. *IEEE Transactions on energy conversion,* 28**,** 535-542.

PENA, R., CLARE, J. & ASHER, G. 1996. Doubly fed induction generator using back-to-back PWM converters and its application to variable-speed wind-energy generation. *IEE Proceedings-Electric Power Applications,* 143**,** 231-241.

PETERSSON, A., HARNEFORS, L. & THIRINGER, T. Comparison between stator-flux and grid-flux-oriented rotor current control of doubly-fed induction generators. 2004 IEEE 35th Annual Power Electronics Specialists Conference (IEEE Cat. No. 04CH37551), 2004. IEEE, 482-486.

PEYGHAMI, S., PALENSKY, P. & BLAABJERG, F. 2020. An Overview on the Reliability of Modern Power Electronic Based Power Systems. *IEEE Open Journal of Power Electronics,* 1**,** 34-50.

QIN, B., LI, H., ZHOU, X., LI, J. & LIU, W. 2020. Low-voltage ride-through techniques in DFIG-based wind Turbines: A review. *Applied Sciences,* 10**,** 2154.

QIN, B. & SUN, H. 2018. State dependent riccati equation based rotor-side converter control for doubly fed wind generator. *IEEE Access,* 6**,** 27853-27863.

QIN, B., SUN, H., MA, J., LI, W., DING, T., WANG, Z. & ZOMAYA, A. Y. 2018. Robust ${H_\infty} $ Control of Doubly Fed Wind Generator via State-Dependent Riccati Equation Technique. *IEEE Transactions on Power Systems,* 34**,** 2390-2400.

QIN, B., ZHANG, X., MA, J., DENG, S., MEI, S. & HILL, D. J. 2017. Input-to-state stability based control of doubly fed wind generator. *IEEE Transactions on Power Systems,* 33**,** 2949-2961.

RAFIEE, Z., HEYDARI, R., RAFIEE, M., AGHAMOHAMMADI, M. R. & BLAABJERG, F. 2022. Enhancement of the LVRT Capability for DFIG-Based Wind Farms Based on Short-Circuit Capacity. *IEEE Systems Journal,* 16**,** 3237-3248.

REN, J., XIAO, X., ZHENG, Z., WANG, Y., MA, Z. & LIU, K. 2021. Impact of Phase Angle Jump on DFIG Under LVRT Conditions: Challenges and Recommendations. *IEEE Transactions on Power Delivery,* 36**,** 3701-3713.

RODRIGUEZ, P., TEODORESCU, R., CANDELA, I., TIMBUS, A. V., LISERRE, M. & BLAABJERG, F. New positive-sequence voltage detector for grid synchronization of power converters under faulty grid conditions. 2006 37th IEEE Power Electronics Specialists Conference, 2006. IEEE, 1-7.

RUIZ-CRUZ, R., SANCHEZ, E. N., LOUKIANOV, A. G. & RUZ-HERNANDEZ, J. A. 2018. Real-time neural inverse optimal control for a wind generator. *IEEE Transactions on Sustainable Energy,* 10**,** 1172-1183.

RUIZ-CRUZ, R., SANCHEZ, E. N., ORNELAS-TELLEZ, F., LOUKIANOV, A. G. & HARLEY, R. G. 2012. Particle swarm optimization for discrete-time inverse optimal control of a doubly fed induction generator. *IEEE transactions on cybernetics,* 43**,** 1698-1709.

SHIHABUDHEEN, K. V., RAJU, S. K. & PILLAI, G. N. 2018. Control for grid-connected DFIG-based wind energy system using adaptive neuro-fuzzy technique. *International Transactions on Electrical Energy Systems,* 28**,** e2526.

SILVA, R. M., CUPERTINO, A. F., REZENDE, G. M., SOUSA, C. V. & MENDES, V. F. 2020. Power control strategies for grid connected converters applied to full-scale wind energy conversion systems during LVRT operation. *Electric Power Systems Research,* 184**,** 106279.

SWAIN, S. & RAY, P. K. 2017. Short circuit fault analysis in a grid connected DFIG based wind energy system with active crowbar protection circuit for ridethrough capability and power quality improvement. *International Journal of Electrical Power & Energy Systems,* 84**,** 64-75.

TANAKA, T., MA, K., WANG, H. & BLAABJERG, F. 2019. Asymmetrical Reactive Power Capability of Modular Multilevel Cascade Converter Based STATCOMs for Offshore Wind Farm. *IEEE Transactions on Power Electronics,* 34**,** 5147-5164.

TENNET, T. GmbH (2012) Grid code high and extra high voltage.

TOUROU, P., CHHOR, J., GÜNTHER, K. & SOURKOUNIS, C. Energy storage integration in DFIG-based wind energy conversion systems for improved fault ride-through capability. 2017 IEEE 6th International Conference on Renewable Energy Research and Applications (ICRERA), 2017. IEEE, 374-377.

WAGNER, C. F. & EVANS, R. D. 1933. *Symmetrical components as applied to the analysis of unbalanced electrical circuits*, McGraw-Hill.

WIAM, A. & ALI, H. 2019. Direct torque control-based power factor control of a DFIG. *Energy Procedia,* 162**,** 296-305.

WINTRICH, A., NICOLAI, U., TURSKY, W. & REIMANN, T. 2011. Application manual power semiconductors. Semikron international GmbH. ISLE Verlag, Illmenau.

WU, Y. K., CHANG, S. M. & MANDAL, P. 2019. Grid-Connected Wind Power Plants: A Survey on the Integration Requirements in Modern Grid Codes. *IEEE Transactions on Industry Applications,* 55**,** 5584-5593.

XIAO, F., XIA, Y., ZHANG, K., ZHANG, Z. & YIN, X. 2023. Fault characteristics analysis of DFIGWT in whole LVRT process considering control strategy switching between RSC and Crowbar. *International Journal of Electrical Power & Energy Systems,* 145**,** 108615.

XU, M., MA, K., LIU, B. & CAI, X. 2021. Modeling and Correlation of Two Thermal Paths in Frequency-Domain Thermal Impedance Model of Power Module. *IEEE Journal of Emerging and Selected Topics in Power Electronics,* 9**,** 3971-3981.

YANG, L., XU, Z., OSTERGAARD, J., DONG, Z. Y. & WONG, K. P. 2011. Advanced control strategy of DFIG wind turbines for power system fault ride through. *IEEE Transactions on Power Systems,* 27**,** 713-722.

YAO, Y., GAO, F. & ZHOU, Z. Reactive Power Voltage Stability Control of Power System with Wind Turbine Based on STATCOM. 2022 6th International Conference on Power and Energy Engineering (ICPEE), 25-27 Nov. 2022 2022. 31-36.

ZHANG, Y., YANG, Y., CHEN, X. & GONG, C. 2021. Intelligent Parameter Design-Based Impedance Optimization of STATCOM to Mitigate Resonance in Wind Farms. *IEEE Journal of Emerging and Selected Topics in Power Electronics,* 9**,** 3201-3215.

ZHOU, D. & BLAABJERG, F. 2020. Converter-level reliability of wind turbine with low sample rate mission profile. *IEEE Transactions on Industry Applications,* 56**,** 2938-2944.

ZHOU, D., BLAABJERG, F., LAU, M. & TONNES, M. Thermal behavior of doubly-fed induction generator wind turbine system during balanced grid fault. 2014 IEEE Applied Power Electronics Conference and Exposition-APEC 2014, 2014a. IEEE, 3076-3083.

ZHOU, D., ZHANG, G. & BLAABJERG, F. 2018. Optimal Selection of Power Converter in DFIG Wind Turbine With Enhanced System-Level Reliability. *IEEE Transactions on Industry Applications,* 54**,** 3637-3644.

ZHOU, L., LIU, J. & ZHOU, S. 2014b. Improved demagnetization control of a doubly-fed induction generator under balanced grid fault. *IEEE Transactions on Power Electronics,* 30**,** 6695-6705.

ZHOU, Z., WANG, X., ZHAO, F., SVENSSON, J. R., KOCEWIAK, Ł. H., GRYNING, M. P. S. & MOHANAVEERAMANI, A. 2023. Selective Harmonic Voltage Control for STATCOMs in Wind Power Plants. *IEEE Transactions on Power Delivery,* 38**,** 2183-2194.

ZHU, D., ZOU, X., DENG, L., HUANG, Q., ZHOU, S. & KANG, Y. 2016. Inductance-emulating control for DFIG-based wind turbine to ride-through grid faults. *IEEE Transactions on Power Electronics,* 32**,** 8514-8525.

ZHU, D., ZOU, X., ZHOU, S., DONG, W., KANG, Y. & HU, J. 2017. Feedforward current references control for DFIG-based wind turbine to improve transient control performance during grid faults. *IEEE Transactions on Energy Conversion,* 33**,** 670-681.